THE UNIVERSITY *of* EDINBURGH

Numerical simulation and characterization of site specific tidal flow turbulence

Thesis submitted for the degree of Doctor of Philosophy

2019

By

Manuel Guillermo Reta Palacios

The University of Edinburgh

School of Engineering

April 15, 2020

"Only a beast as deluded and stubborn as mankind could confront chaos and randomness, and dare to make sense of it, but we try spectacularly!"

ABSTRACT

The main area of study of this thesis was to research the effect of the bathymetry (the topography of the ocean floor) on the turbulent nature of a tidal energy site by way of high-resolution computational fluid dynamics simulations. Wall Modelled Large Eddy Simulations, for both flood and ebb tides, were carried out of a sampled area of the Fall of Warness, Scotland, which is the European Marine Energy Centre tidal energy site. Results from the simulations were validated with velocity and turbulence data from site measurements at the European Marine Energy Centre site. Both the simulation and the test data correspond to flows at 2.1 m/s turbine hub height reference velocity for ebb and flood tides.

Results show the influence of the sea bottom as a modifier of flow velocities and a driver of turbulence production at local areas important for the purposes of tidal converter performance and loading. High order turbulence parameters such as: Reynolds stresses, length scales, frequency spectra and turbulence intensities are analysed at different depths and locations in the domain, to better understand their local dependence on the changing bathymetry.

Turbulence data presents highly energetic coherent structures of a sufficiently large spatial and temporal size, connected to bathymetry variation. Both flood and ebb tidal simulations show that site bathymetry not only influences the mean flow, but also turbulent structure, energy efficiency of turbulent kinetic energy extracted

from wall shear stress and three-dimensional distribution of Reynolds Stresses. Turbulence was found to be more isotropic for larger portions of the water column than found in previous simulations of roughened surface flows, with an especially chaotic flow area covering the bottom fifth of the water column filled with energy rich turbulent events.

Quadrant analysis for multiple depth probe locations is used to give a three-dimensional statistical understanding of bursting events, as modified by the seabed. The results show highly energetic coherent structures of a sufficiently large spatial and temporal size, connected to bathymetry variation. Ebb and flood turbulent features were compared in an effort to further understand the role bathymetry plays on tidal asymmetry. The temporal, spatial and energetic character of coherent turbulent structures were analyzed, within a context of the direction of the flow and its link to the seabed as a driving force for turbulence generation. Ebb tide was found to have a stronger turbulent intensity and production than flood tide for the same reference mean flow velocities.

The thesis adds to the knowledge of tidal energy site flow characterization and the turbulence of offshore environments by showing the strong imprint of bathymetry on tidal flows. The numerical methodology employed shows a guideline for studying the local and unique seabed bathymetry interactions with the tides. The use of high-resolution large eddy simulations is shown to be a tool capable of reproducing energy rich resolved structures vital to continuous advancement of energy extraction devices.

DECLARATION

I declare that this work is fully my own work and has not been submitted for any other degrees or professional qualification except as specified.

ACKNOWLEDGMENTS

I would like to firstly acknowledge the help, mentorship and support that I received from my supervisors Dr Vengatesan Venugopal and Dr Angus Creech. Both have been an invaluable source of encouragement and help during my time at the University of Edinburgh. The doctorate was funded under the Mexican Government CONACYT scholarship of which I will be eternally grateful.

I would also like to thank the help I received during my PhD from Dr Brian Sellar and Dr Duncan Sutherland for all their efforts providing and explaining the ReDAPT data, which have been a fundamental portion of my thesis.

A huge thank you to all of my friends and colleagues at IES who have been of enormous support in all aspects these last years. Above all thank you to my beloved family without whom nothing would have been possible.

CONTENTS

NOMENCLATURE

Latin Symbols

$\dot{m}$	Cell face area (m^2)
$\hat{t}$	Aggregate Time (s)
$\mathbf{a}$	Surface vector (m)
$\mathbf{B_{ij}}$	Reynolds stress anisotropy tensor (-)
$\mathbf{J}^{\phi}$	Convective and diffusive face flux ($1/s$)
$\mathbf{J}$	Jacobian tensor of velocity ($1/s$)
$\mathbf{R_{ij}}$	Reynolds stress tensor (m^2/s^2)
$\mathbf{S_d}$	WALE model tensor ($1/s$)
$\mathbf{S_{ij}}$	Strain rate tensor ($1/s$)
$\mathbf{u}^*$	Root Mean Square of velocity signal (-)
$\overline{u}$	Averaged value (-)
a	Model Coefficient from k-ω model (-)
a_{ij}	Cholesky Decomposition of Reynolds stress tensor (-)

B_{ii}^{norm}	Normalized autocorrelation coefficient (-)
C^{+}	Roughness Coefficient (-)
C_s	Smagorinsky Coefficient (-)
C_t	Model Coefficient (-)
C_w	WALE model Coefficient (-)
f	Frequency (Hz)
f_1	Mesh Resolution studied variable (-)
f_k	Tent function (-)
f_r	Under relaxation factor (-)
f_v	Van Driest Damping function (-)
G	Filter function (-)
H	Hole Size (-)
H_{m0}	Wave Height (m)
h_{ref}	Hub-Height reference (m)
i	Iteration (-)
$I_{i,H}$	Filtering quadrant function (-)
II	Second Invariant of the anistropy tensor (-)
III	Third Invariant of the anistropy tensor (-)
k	Turbulent kinetic energy (m^2/s^2)
k_{res}	Resolved kinetic energy (m^2/s^2)
k_{sgs}	Subgrid scale kinetic energy (m^2/s^2)

k_{uw}	Kurtosis of uw cross component(-)
$N_{x,y,z}$	Number of cells per direction (-)
p	Pressure (Pa)
p''	Corrected pressure field (Pa)
$Q(1-4)$	Quadrant of $\overline{u'w'}$ Reynolds Stress (-)
r	Residual (-)
r_{12}	Refinement ratio (-)
Re	Reynolds Number (-)
Re_θ	Momentum Reynolds Number (-)
$S_{i,H}$	Averaged value per hole for the fractional contribution (-)
S_{uw}	Skewness of uw cross component (-)
T	Total time of simulation (s)
T	Turbulent time scale (s)
t	Time (s)
t^*	Non-dimensional time (-)
$T_{i,H}$	Averaged value of bursting event (s)
T_{int}	Integral Turbulent time scale (s)
u'	Fluctuation component (-)
u''	Root-mean-square of velocity (-)
u_τ	Friction velocity (m/s)
$u_{i,j,k}$	Instantaneous velocity in streamwise, spanwise and vertical directions (m/s)

u_{ref}	Hub-Height reference velocity (m/s)
u_{rms}	Root Mean Square of velocity signal (-)
V	Volume (m^3)
x_{inlet}	Streamwise position of inlet boundary condition (m)
x_{outlet}	Streamwise position of outlet boundary condition (m)
y^+	Non-dimensional distance to the wall (-)
H	Height (m)

Greek Symbols

α_e	Equivalent angle of attack (rad)
β	k-ω coefficient (-)
$\beta*$	k-ω coefficient (-)
Δ	LES filter size (m)
δ	Boundary Layer Thickness (m)
Δ_ϕ	Cumulative conjuctive error of mesh cells (-)
δ_{ij}	Kronecker delta function (-)
$\Delta_{t,x,y,z}$	Mesh discretization in time and space (s,m)
ϵ	Turbulence dissipation rate (m^2/s^3)
ϵ_k	Spin Unit Value (-)
η	Kolmogorov scale (Ns^2/m^2)
Γ	Gamma diffusion coefficient (-)
γ	Quality Coefficient (-)

κ	Von Karman constant $(-)$
λ_r'	Local instantaneous tip-speed ratio (-)
$\mathbf{\Omega}$	Vorticity tensor $(1/s)$
$\tau_{\mathbf{ij}}$	Subgrid stress tensor (m^2/s^2)
μ	Dynamic viscosity (Ns^2/m^2)
μ_T	Turbulent Dynamic viscosity (Ns^2/m^2)
ν	Kinematic viscosity (m^2/s)
ν_T	Turbulent Kinematic viscosity (m^2/s)
ω	Specific rate of dissipation $(1/s)$
ω	vorticity (rad)
ϕ	Scalar variable (-)
ϕ_{ii}	Power Spectrum Density $(m^4/s^4/Hz)$
ρ	Density of working fluid (kgm^{-3})
ρ_0	Initial Density (kgm^{-3})
σ	Standard Deviation (-)
σ_k, ϵ	Model Coefficients for k-ϵ model (-)
σ_k, ϵ	SEM eddy turbulent length scale (-)
τ_ω	Wall shear stress(Pa)

Acronyms

ADCP	Acoustic Doppler Current Profiler
AIM	Anisotropy Invariant Map

AMG	Algebraic Multigrid Method
BEMT	Blade element Momentum Theory
CFD	Computational Fluid Dynamics
CFL	Courant-Friedrichs-Lewy condition
CTKE	Coherent Turbulent Kinetic Energy
DES	Detached Eddy Simulation
DNS	Direct Numerical Simulation
EMEC	European Marine Energy Centre
GCI	Grid Convergence Index
LES	Large Eddy Simulation
LSM	Large Scale Motion
PISO	Pressure-Implicit with Splitting of Operators
PSD	Power Spectrum Density
RANS	Reynolds Averaged Navier Stokes
ReDAPT	Reliable Data Acquisition Platform for Tidal
ROMS	Regional Ocean Modelling System
SB-ADP	Single-beam Acoustic Doppler Profiler
SEM	Synthetic Eddy Method
SF	Safety Factor
SGS	Sub-Grid Scale
TI	Hairpin structure

TI	Turbulence Intensity
TKE	Turbulent Kinetic Energy
URANS	Unsteady Reynolds Averaged Navier Stokes
VLES	VeryLarge Eddy Simulation
VLSM	Very Large Scale Motion
WALE	Wall Adapting Local Eddy viscosity

LIST OF FIGURES

LIST OF TABLES

CHAPTER 1

INTRODUCTION

1.1 Tidal Energy

The growth and development of sustainable energy technology is one of the greatest challenges in our current society. Energy transition from carbon rich fossil fuels to renewable sources is an ongoing endeavour. The European Union has set energy targets to cut 40% of greenhouse emissions, improve energy efficiency by 32.5% and source at least 32% of its energy from renewable sources by 2030 (Union, 2014). The achievement of this endeavour hangs on using a variety of methods, tools and technologies to use local resources for a diversified energy portfolio.

Several hurdles remain in the development of renewable energy, and it would be remiss to not mention that immense societal, technological and economic challenges that are yet to be fully solved. However, advancements in the fields of solar and wind energy have shown how quickly technological development, not only in a technical sense, but also as economically attractive alternatives to fossil fuels can be achieved. The unpredictability and intermittency of many renewable energy sources, such as the previously mentioned solar and wind, limit their applicability for immediate energy use and transmission over large distances.

Marine renewable energy seeks to bring an additional source to the energy port-

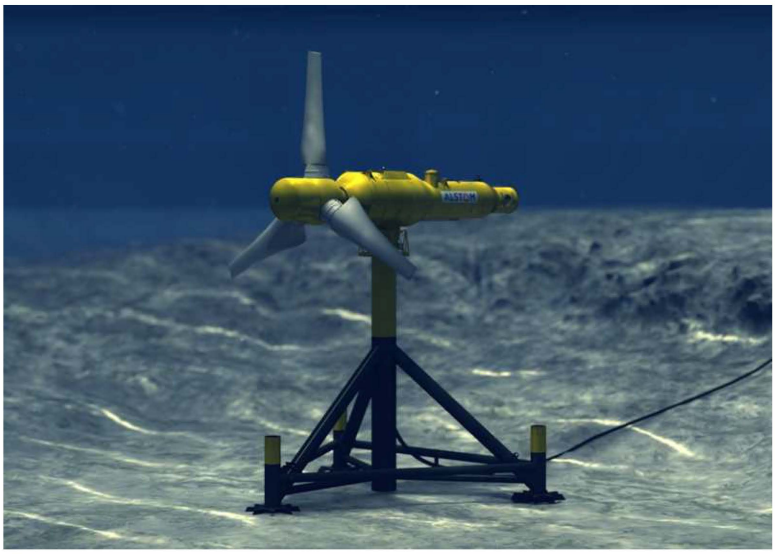

Figure 1.1: Alstom Tidal Turbine, installed at the European Marine Energy Centre.

folio to aid the energy transition. The ocean and other large bodies of water hold a large unused potential for energy extraction that development has rapidly increased to harness this untapped source. Many different technologies and methods are covered by the marine renewable umbrella (wave, river kinetic energy, tidal etc.). All of them carry an advantage of relative predictability that make them attractive alternatives for mass use and commercialization.

Tidal energy is a growing field that seeks to harness the energy resource of the ocean, specifically that of tidal flows. Tidal flows are driven by gravitational force interactions between celestial bodies (Sun, moon and earth). The orbital movements result in many tidal constituents, however the largest contributors are the principal lunar semi-diurnal (M2) and principal solar semi-diurnal (S2). Both have approximately the same time period $T_{M2} = 12.42\ hrs, T_{S2} = 12\ hrs$, yet sufficiently different to have a synchronised period (spring tide) and an anti phase period (neap tide). Although tidal energy is currently in an earlier stage of development, it offers a level of predictability that make it a perfect support for intermittent energy sources. Resource estimates by Davies (2017) put global energy resource at 2950 $TWh/year$, while Neill et al. (2018) calculated a larger theoretical resource values of 5792 $TWh/year$. The United Kingdom as well as many coastal areas around Europe are fortunate enough to have several rich energy sites ripe for development. The

extractable resource for the UK alone is estimated by Neill et al. (2018) to be 366 $TWh/year$, although this number is still subject to other practical considerations that would limit the resource further.

Several measurement campaigns have been carried out to understand and describe the tidal resource at potential energy sites. Tidal Energy sites measurements by McCaffrey et al. (2015), Milne et al. (2017), McMillan et al. (2016), Thomson et al. (2012), Sellar et al. (2018), Gunawan et al. (2014), and others have helped in understanding realistic turbulent flows within ocean energy engineering objectives and sites. All of these careful measurement campaigns have helped developers record turbulence statistics and velocity fields that help with the design of tidal energy converters.

Thomson et al. (2012) measured turbulence at two tidal energy sites in Puget sound, using Acoustic Doppler Current Profilers (ADCP) for the precise purpose of tidal energy resource assessment and performance. Turbulence levels were seen to fluctuate throughout the water column for both sites. Averaged turbulence intensity levels at hub height were measured at 10%, while higher values (up to 20%) of turbulence intensity appeared near the seabed.

Thomson's research stressed the importance of turbulence being taken into account as a fatigue factor for impacting stresses on tidal turbines. Larger scale anisotropic eddies occur and interact at the same frequency as turbine rotor diameter frequencies,while isotropic small scale dissipative turbulence would interact with blade chord length frequencies. McCaffrey et al. (2015), using data taken at the Puget Sound site in the US, found a large amount of anisotropical turbulent events and mentions the role of topography shedding in changing turbulence to a two-dimensional state as shallow depth does not allow for isotropy to develop.

Milne et al. (2013) showed similar results for the Sound of Islay by connecting spectral anisotropy results with bursting event processes close to the seabed. From past site measurements, and the fundamental research of roughness effects, it was surmised that turbulence characteristics and structures were related to the inherent variability of the seabed depth, as seen in Lu et al. (2002), and its localized peaks and

troughs interaction with both flood and ebb flows. McMillan et al. (2016) studied turbulence data at the mouth of the Bay of Fundy. Although a shallower site ($10-30m$) in comparison to the $40m$ depth of the Fall of Warness, it was characterized by several strong bathymetric features of interest (i.e prominent sudden ridges) for turbulent production. These bathymetrical features generated significant large scale turbulence near the seabed and up to a third of the water column. Interaction of the flow with the aforementioned prominent ridges within the channel lead to a tidal asymmetry for turbulent parameters. The study reported a strong asymmetry regarding the thickness of the bottom boundary layer between tides as reported equally by Hay et al. (2013) at the Bay of Funday site. Ebb tide velocity depth profiles did not fit the log-layer, as seen similarly to results at the Fall of Warness in Scotland. Strong turbulent anisotropy was seen for all of the previously mentioned sites. Dominance of the streamwise component at larger length scales was found by Milne at the Sound of Islay. Similar results from other site surveys show the critical need to take into account the anisotropical nature for each length scale when creating realistic inflows in modelling efforts. Several measurement campaigns and numerical modelling work (e.g, ReDapt, FlowTurb etc seen in Venugopal and Nemalidinne (2014); Sellar et al. (2018); Osalusi et al. (2009a) have been undertaken in the past to measure and understand tidal flow environment characterization of the Fall of Warness. Most of the measurements are point location based and do not provide a complete spatial and temporal structure of turbulence characteristics under tidal currents. A well designed numerical model would be preferred in such circumstances. Such a model would provide both spatial and temporal scale information, so long as it is designed to capture sufficiently representative lengths as well as small enough resolution for each turbulent movement.

1.2 European Marine Energy Centre Test Site

The Fall of Warness in Orkney is currently one of the most important tidal energy sites, not only in the UK but also worldwide. The high energy resource of the site,

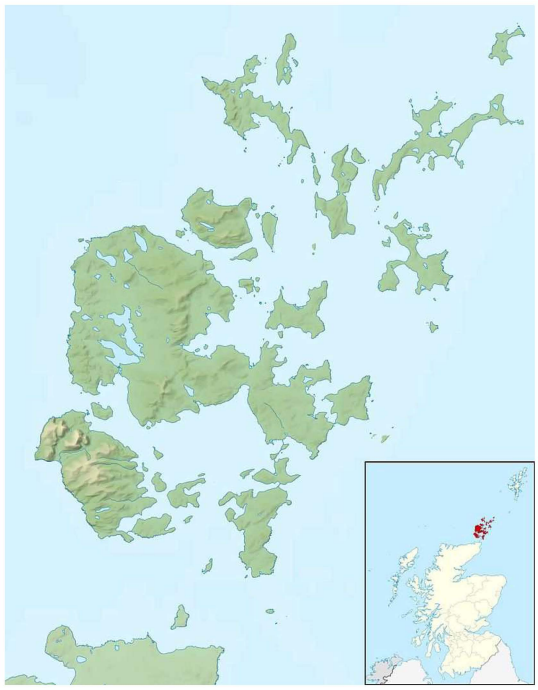

Figure 1.2: Location of the European Marine Energy Centre in Orkney, Scotland.

Figure 1.3: Aerial view of the Fall of Warness. Island of Eday and Muckle Green Holm are visible to the sides of the strait.

extensive device testing experience and site characterization make it a rich source of information for tidal energy site analysis. This work has been done in cooperation with many research institutes and the European Marine Energy Centre.

The Fall of Warness is located in the Orkney islands in northern Scotland (59 08.14N, 2'48.39E). It is bound by the island of Eday on the northeast and the isle of Muckle Green Holm. The rapid flows of the channel reach up to 4.0 m/s during spring flows. The speed of the flows create a strong turbulent flow in the order of a Reynolds number ($Re = 10^7 - 10^8$) based on a half channel depth length scale.

The ReDAPT project provides us with an incredible wealth of information about the Fall of Warness that proves to be an invaluable resource to validate, compare and learn for future tidal projects. Its success can be attributed to the collaboration of many stakeholders, amongst them, the University of Edinburgh, Alstom Ocean Energy, EMEC as well as many others. The long three year project took measurements of the Fall of Warness flow environment with a series of deployments. A number of

deployments included measurement of flows that featured an experimental installed turbine to learn the impact of turbines on the ambient flow. The main objective of the project was to better understand the hydrodynamic loads that come from the physical resource phenomena and a characterization of the spatial and temporal scales that interact with the actual turbine.

ReDAPT took metrics of the site that will be discussed as part of the understanding of tidal energy and an introduction to the main parameters needed to comprehend the context of the tidal energy site flow at the Fall of Warness. The immensity of the data acquired during the project is so vast as to overlap the scope of the thesis. Only the most pertinent of characteristics of the flow will be discussed. The main characteristics relate to the current mean velocities during ebb and flood, turbulence parameters along the water column and the strength and influence of waves. Data was reported in the technical report packages available at the ReDAPT website (redapt.eng.ed.ac.uk) and presented in Sellar et al. (2018) and Sellar and Sutherland (2016) amongst others.

Velocity depth profiles were found to follow a power law when isolated from wind and wave driven surfaces. This follows similar behaviour to theoretical channel flow and zero pressure gradient boundary layer flows, expanded on in the following chapters especially in relation to validation of the present work. Significant wave heights ranged from 0-4 m and composed mainly by Northwesterly swells, with wave periods of 10-20 s, and Southerly wind waves of periods within 5-10s (Osalusi, 2010)

Tidal energy resource extraction requires an improved understanding of the hydrodynamic forces that affect the design, performance and lifetime of tidal energy devices. The currents and waves that drive the sea flow carry an inherent uncertainty due to sea turbulence. The particular characteristics that define turbulence are unique for each tidal energy site. However, we can compare measurements at the Fall of Warness with previously mentioned tidal energy sites for a better contextualization of flow conditions and their driving forces.

The magnitudes and scales of turbulent motion at tidal energy sites have been shown to be of further interest to the understanding of device performance in the

sea. Turbulence at the Fall of Warness was recorded and analysed by Osalusi et al. (2009a,b); Sellar et al. (2018) amongst others. Osalusi et al. (2009a) studied turbulence for the entire water column while paying close attention close to the seabed. Data was obtained from an ADCP at 1.63 m from the seabed for a day long period and for peak speeds of 1 m/s. Turbulent energy production $\mathcal{P}$ was found to outstrip dissipation ϵ particularly during flood tides. All studies were found to have local maxima near the seabed for all turbulent parameters.

The Fall of Warness is characterized by a noticeable tidal asymmetry between the ebb and flood tides. Site measurements taken and processed by Sellar et al. (2018) shows no wave flood tide velocities depth profiles following a power-law equation behaviour. Ebb tide, in contrast to Flood tide, deviates strongly from the power law in the upper mid water column. Current velocities slow down after the mid column with an even stronger retardation as the flow velocity increases. The asymmetry is also apparent in higher current velocities for ebb flow (3.7 m/s) versus (3.3 m/s) during flood tide. Turbulence intensity levels showed similar discrepancies between their respective tides. While flood tides followed an almost linear decrease as the water column neared the sea surface, ebb tide held an increasingly large bump at the 10 m from the seabed mark as the current sped increased as well.

Regional coastal modelling by Neill et al. (2017) of the Fall of Warness, utilizing the ROMS (Regional Ocean Modeling System) hydrostatic code, studies the nature of this tidal asymmetry for tidal currents, turbulent dissipation and power output. Neill et al. (2014) mentions how tidal asymmetry can be a product of diverse factors interacting for each site, creating advective inertial and turbulent diffusive forces. Meteorological effects, topographic features and tidal component combinations can change the intensity of the asymmetry impacting resource magnitude and extraction. While the model ascribes the asymmetry to tidal phase relationships the authors do find turbulent value asymmetry strongest near the seabed. The contribution of the seabed and other topographical features is open to further study as a source of high turbulence during the different tidal currents.

1.3 Thesis Objectives & Structure

The aim of this thesis is to produce a faithful and representative model of EMEC tidal energy site at The Fall of Warness, Orkney with the special emphasis placed on understanding the role bathymetry plays on the turbulent hydrodynamics of the flow using high resolution computational fluid dynamics (CFD) numerical modelling codes.

CFD codes are selected as the desired method of research due to the high cost of site measurement data and the wealth of existing information that could support the creation of a high-fidelity numerical tool. Existing and past projects at the University of Edinburgh in collaboration with other research institutes, concerning the Fall of Warness EMEC site, allow for models to be tuned and developed with realistic inflows and validation data.

Work focused on this aim was structured in such a manner that the resulting model was capable of reproducing the turbulent phenomena close to the seabed as a way of capturing, as accurately as possible, the flow field in all three dimensions. The research shown in this thesis presents the decomposition of the research plan as each subsequent chapter builds on the past to improve the design and analysis of the work with improved tools and techniques. A summary of the research objectives can be presented in the following questions:

1. Is it possible and how does one develop affordable and available numerical models capable of capturing the unique turbulent character of a tidal energy site?

2. What is the effect of seabed irregularities on turbulence statistics and can it explain the discrepancies between site measurements and ideal flows?

3. What are the turbulent structures present in tidal channel flow and how do they contribute to the kinetic energy budget of the flow?

4. What role do the ebb and flood tides, and thus direction of the flow, play on the turbulent nature of the flow?

Each chapter of this thesis follows its own purpose in service of answering these research questions while bringing them together as a coherent body of research.

The present first chapter aims at understanding the thought process that went into designing the scope and novelty of the presented research by means of introducing the topic at hand. It is fundamental for the reader to be acquainted with tidal energy, some of the important development sites and specifically the EMEC site which will be the focus of the thesis.

Chapter 2 offers a short guide on the theory behind turbulent concepts. Theory ranges from introductory remarks to a presentation of the most well-known and used CFD models This includes commentary on their advantages and disadvantages regarding the aim of the research.

Chapter 3 presents a literature review of previous tidal energy modelling attempts and the current state of knowledge of turbulent flows and the coherent structures produced in them. Building upon the concepts in the previous chapter the reader will be shown a summary of the most relevant modelling attempts and fundamental research in turbulence.

Chapter 4 shows a detailed overview of the CFD numerical simulations used to model the EMEC tidal energy site. Descriptions will be offered of the meshing strategy, boundary conditions, numerical methods, domain selection and quality checks ensuring a level of trust as part of the verification process.

Chapter 5 shows results from a high-resolution large eddy simulation of a 2.1 m/s flood and ebb tide. Simulation was created using the real scale bathymetry of the EMEC site. Results describes the different turbulent statistics along the three-dimensional domain. Validation is shown with site measurements.

Chapter 6 provides an analysis on the turbulent structure and coherent structures seen during the 2.1 m/s flood tide described in Chapter 4. Analysis focuses the bathymetry effect on turbulent discrete events and their relationship to Reynolds stresses structure as they originate from the changing seabed bottom for a device scale domain.

Chapter 7 continues the analysis of chapter five for the corresponding ebb tide.

Results will show the comparative difference between ebb and flood tides, characterize the turbulent ebb flow and the coherent structures seen as a result of the resolved modelling of the EMEC site.

Chapter 8 presents the conclusion of the previous chapters description of methodology, results and finally a summary of the key findings of the work as a whole. Synthesis of the conclusions will be shown as a recommendation for future work.

Appendix A provides supplementary information supporting the validation of the numerical simulations that is referred to in the respective chapters.

CHAPTER 2

TURBULENCE MODELLING THEORY

2.1 Introduction

This chapter will introduce some of the fundamental turbulent concepts and terminology that will be essential to the understanding of the analysis brought upon in latter chapters. Among the topics touched on, are the numerical modelling tools used in CFD for turbulence. Comprehension of the limits and assumptions of turbulent models is key when analysing the turbulence of tidal energy sites. Research on turbulence has been a long ongoing endeavour, the discussion and presentation of the existing body of work for turbulent flows would cover multiple books and endless research papers. The aim of this chapter is not to present a complete review of the subject but to present the reader with sufficient understanding of the topic to comprehend the analysis of turbulent flow at the Fall of Warness and the context of its modelling.

Discussion on turbulent flows will begin from the very building blocks of fluid dynamics in the Navier-Stokes equations and the inherent uncertainty that comes from turbulent flows. Although turbulence is one of the most challenging physical problems, still among one of the unsolved Millennium Prize problems, some sense has already been made of these seemingly random chaotic behaviours. Material pre-

sented here is the result of reading and summarizing great fundamental turbulence books and notes by Pope (2004); Davidson (2012); McDonough (2017); Celik (1999); George (2010) and others which helped organize and elucidate such a gargantuan highly complex topic.

2.2 Fundamental fluid dynamics concepts

All fluid motions discussion must begin with the fundamental Navier-Stokes equations of mass and momentum conservation. Equations 2.1 and 2.2 show the mass and momentum conservation equations respectively for incompressible, constant property flows. Here the velocity flow field is represented by u_i with the subindex indicating the dimension while the position is indicated by x_i.

$$\frac{\partial u_i}{\partial x_i} = 0 \tag{2.1}$$

The incompressible Navier-Stokes equations are also composed of a momentum balance shown in a deglossed manner in equation 2.1 (McDonough, 2017) for an unsteady three dimensional flow. Each component of the equation will be introduced due to its importance in later sections for modeling clarification and importance to turbulent phenomena. All equations will use the convention i, j, k for each direction (streamwise, spanwise and vertical respectively) and t for time.

$$\underbrace{\frac{1}{\rho}\frac{\partial u_i}{\partial t}}_{Time\ Variation} + \underbrace{\frac{1}{\rho}\frac{u_i \partial u_j}{\partial x_j}}_{Convection} = \underbrace{-\frac{\partial p}{\partial x_i}}_{Pressure\ gradient} \underbrace{+\mu\frac{\partial^2 u_i}{\partial x_j \partial x_j}}_{Diffusion} \tag{2.2}$$

The time variation and convection term establish the material derivative of the flow field showing how fluid moves due to temporal and velocity differentials. A pressure gradient ∂p drives the fluid in each direction according to the net force on the control volume. Diffusion acts in direct opposition of the flow by viscous friction effects brought upon by the material property of viscosity μ that opposes the flow. Additional forcing terms may be added to the momentum conservation equation.

2.3 Fundamental Turbulence concepts

Turbulent flows should first be described in terms of their Reynolds number (Re) (shown in equation 2.3). The Reynolds number is a non-dimensional measure of inertial forces over viscous forces. A flow will become turbulent when the inertia overtakes the viscosity by such a large degree that the flow becomes chaotic and disorganized.

$$Re = \frac{uL}{\nu} \tag{2.3}$$

The velocity u and length scale L are characteristic lengths and speeds of the flow while the inertial laminar component is represented by the kinematic viscosity $\nu = \mu/\rho$. Characteristic length scales depend on the particular case analyzed, turbulent channels may use a full or half channel depth. As the flow enters a turbulent state, it becomes imperative to separate and measure the fluctuations within the unstable flow independent from the mean flow. The Reynolds decomposition divides the instantaneous velocity u_i into a time or ensemble-averaged component $\overline{u_i}$ and a fluctuating component u_i' as seen in equation 2.4.

$$u_i = \overline{u_i} + u_i' \tag{2.4}$$

Turbulence flow fields, although irregular and seemingly random, can actually be deconstructed from their fluctuating values into a series of spatial and temporal scales called eddies. Each eddy is of a subsequent smaller size feeding off of a larger scale until it reaches heat dissipation due to viscosity. The fluctuation velocity component from equation 2.4 contains the entire range of eddie scales. The decomposition of the fluctuation can be achieved by switching over to a Fourier space in equation 2.5. The Fourier series (shown in equation 2.5 describes any signal $g(x)$ as an infinite sum of periodic sinusoidal signals of wavenumber (κ).

$$g(x) = \frac{1}{2}a_0 + \sum_{n=1}^{\infty}(a_n cos(\kappa_n x) + b_n sin(\kappa_n x)) \tag{2.5}$$

where the a_0, a_n and b_n are Fourier series coefficients, following Parseval's Theorem for a periodic function of lengths $2L$, which in this case is the size of the complete turbulent signal. The wavenumber (κ_n) corresponds to each singular eddy that makes up the entire turbulent motion.

$$a_n = \frac{1}{L}\int_{-L}^{L} g(x)cos(\kappa_n x)dx \tag{2.6}$$

$$b_n = \frac{1}{L}\int_{-L}^{L} g(x)sin(\kappa_n x)dx \tag{2.7}$$

Eddies can be mapped onto a spatial wave number space (κ) versus their respective energy content $E(\kappa)$, for a full view of the behaviour of the turbulence spectrum. The spectrum is divided by Kolmogorov (2006) to describe the scales of turbulent eddies and their main characteristics within the overall flow field.

I. Energy containing range: The energy containing region holds the largest eddies as well as the largest amount of TKE of the entire spectra. The size of the eddies in this region is, at a minimum, in the order of a characteristic length for the flow L. The integral length scale L can be the mid-height of the channel flow or the boundary layer thickness for boundary layer flow, however the precise calculation of the length scale may be calculated by several methods (autocorrelation, spatial two point correlation, spectral etc). The turbulent cascade process begins in the largest eddies passing energy onto the smaller scales on and on until dissipation scales.

II. Inertial range : The wavenumber bandwidth is closely related to the Reynolds number, thus its existence is only seen at high enough Re. Length scales are also called Taylor microscales. The range is easily identified enough as in figure 2.1 by a -5/3 slope when plotted for a energy spectra. It is at the beginning

of this region where turbulence loses any anisotropic character for its eddies. That is to say unequal turbulent behavior between velocity components is balanced out.

III. Dissipation range: Here we find the smallest of all scales within the spectrum, also called Kolmogorov scales η. The cascading of energy from the energy containing region ends as energy is finally dissipated into heat. At this scale all turbulence is completely isotropic.

The entire energy content of the turbulence spectra can be integrated in all three dimensions to obtain the turbulent kinetic energy k for all wave numbers, this can also be described as an infinite sum of the Fourier series squared seen in equation 2.5. The TKE can alternatively be calculated as the energy within the fluctuation component of its velocity signal as seen in equation 2.8.

$$k = \frac{1}{2}\overline{u_i' u_i'} = \int_0^\infty E(\kappa) d\kappa = L \sum_{n=1}^{\infty} g^2(\kappa_n) \tag{2.8}$$

Here two alternative definitions of the turbulent kinetic energy content of the flow k are presented. Turbulent energy content of the signal is measured as the average of the self-multiplied fluctuations in each direction. It is important to note that due to the three-dimensionality of the flow fluctuations will have cross-component interactions. The Reynolds stress tensor $\mathbf{R_{ij}}$ establishes a clear picture of both the self multiplied fluctuations and the cross-component interactions due to its nature as a symmetrical tensor.

$$\boldsymbol{R_{ij}} = \overline{u_i' u_j'} \tag{2.9}$$

Equation 2.9 describes the strict definition of the Reynolds stress. The equation allows for a complete mapping of the structure of the turbulent flow, showing not only the diagonal stresses but also the shear non-diagonal anisotropic values.

Turbulence intensity I is an alternative parameter to the Reynolds stresses, highly used within wind and tidal energy. It is used to describe the fluctuations as a percentage % deviating from the mean flow. It is worth mentioning, due to the high use within site measurements and in the literature, its high sensitivity to the mean in comparison to Reynolds stresses.

$$I = \frac{\sqrt{\overline{u'^2}}}{\overline{u}} \tag{2.10}$$

The Navier-Stokes equations may be rearranged in a way that places the turbulent kinetic energy as the main variable and shows its main mechanisms within fluid flows term by term. Equation 2.11 (adapted from George (2010)) shows the rearrangement and decomposition into four different terms.

$$\underbrace{\frac{\partial k}{\partial t} + \overline{u_j}\frac{\partial k}{\partial x_j}}_{(1)} = \underbrace{-\frac{1}{\rho_o}\frac{\partial \overline{u_i' p'}}{\partial x_i} - \frac{1}{2}\frac{\partial \overline{u_j' u_j' u_i'}}{\partial x_i} - \nu\frac{\partial^2 k}{\partial^2 x_j}}_{(2)} \underbrace{- \overline{u_i' u_j'}\frac{\partial \overline{u_i}}{\partial x_j}}_{(3)} \underbrace{- \nu\overline{\frac{\partial u_i'}{\partial x_j}\frac{\partial u_i'}{\partial x_j}}}_{(4)} \tag{2.11}$$

1.- Material Derivative: Left hand side of the turbulent kinetic energy budget shows the complete change in time and space of the TKE through its different processes, The two terms show the time dependency and convection respectively.

2.- Transport: Transport is composed of a combination of events within the flow: pressure, turbulence and viscosity respectively in (2). The pressure term of the transport portion of the TKE equation can also be called the pressure diffusive term.

3.- Production $\mathcal{P}$: The negative sign of the production term shows how kinetic energy moves across the mean flow and the fluctuating flow, it is the only term in the TKE budget that allows this exchange between mean and fluctuating flows. The shear $\frac{\partial \overline{u_i}}{\partial x_j}$ component of the term is paramount for wall flows, as the component will reach its maxmimum near the wall.

4.- Dissipation ϵ: The dissipative term is the responsible for subtracting turbulent kinetic energy and transferring it into internal energy (e.g. heat) through viscous effects at the smallest scales η. Dissipation is directly proportional to the strain rate $\overline{\mathbf{S_{ij}}} = \overline{\frac{\partial u_i'}{\partial x_j}\frac{\partial u_i'}{\partial x_j}}$ multiplied by the viscosity. Reynolds stresses, which work against the mean flow. will be the ones producing the exchange of energy. Dissipation scales scale with the dissipation rate by a relationship of $\eta = (\frac{\nu^3}{\epsilon})^{1/4}$.

2.4 Turbulence Modelling

Numerical modelling of fluid flows has long had to deal with the great conundrum of having to discretize seemingly disorganized turbulent flows. Several mathematical models have come forward to attempt solve the Navier-Stokes equations, within the computational and time cost constraints of their time and specific objective.

They are, in decreasing order of accuracy and resolution, DNS (Direct Numerical Simulation), LES (Large-eddy simulation), DES (Detached Eddy Simulation), VLES (Very large eddy simulation), URANS (Unsteady Reynolds averaged Navier-Stokes simulations) and RANS (Reynolds Averaged Navier-Stokes simulations). RANS models do not attempt to solve the NS equation unsteady fluctuations, but instead attempt a closure of the equations to obtain a mean level of TKE and length scale.

Figure 2.2 shows the extent of the turbulence spectrum that is resolved by each further model until reaching the highest of models in DNS. DNS does not model any scale of the turbulence spectra, volume cells are of such a fine size that they are capable of resolving down to even the smallest Kolmogorov eddies. Simply put, DNS solves the NS equations with no need for a closure model. The computational cost of DNS is of such a high magnitude (measured in number of volume cells $\approx Re^{9/4}$ (Pope, 2004)), that it may not be used currently for complex geometries or high Reynolds numbers. For engineering purposes, however, not all turbulent scales need be resolved, allowing for a certain level of simplification and economy that is taken advantage of in other turbulence models. LES models are built on this principle

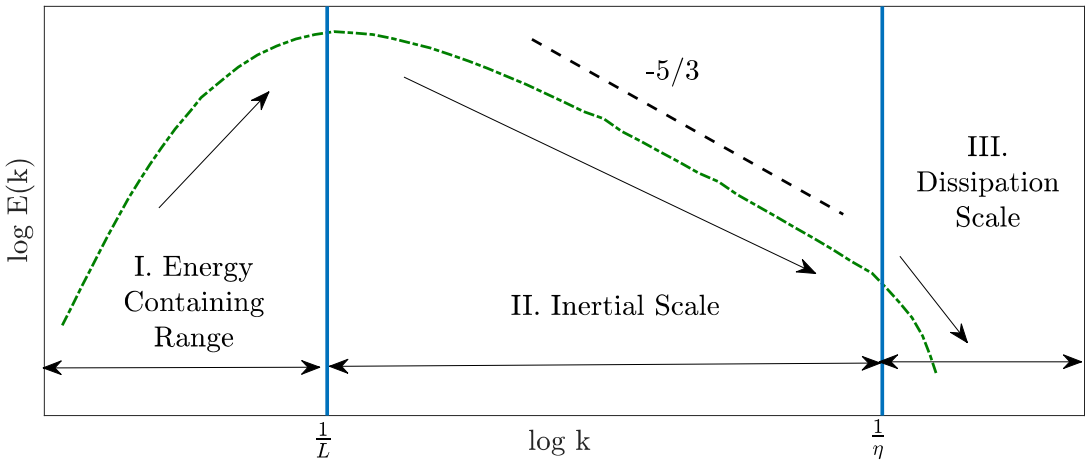

Figure 2.1: Turbulence Spectra

of selectively filtering eddies. The model chooses the scales that are resolved, and the scales that are modeled according to the needs of the particular case studied. Figure 2.3 is considered a good visual comparison of the capabilities each model has in terms of eddy size resolution for a turbulent jet. DNS captures even the smallest of the eddies from the turbulent jet, LES loses some of the finer details while preserving the highest energy content and shape of the larger eddies, while RANS can only average out the eddies losing almost all temporal fluctuations in a smoothed out jet. It is necessary to understand the inner workings of each model to surmise their capabilities and finally choose one for one of the main aims of study.

2.4.1 Reynolds Averaged Turbulence Models

RANS models are based on the initial Navier-Stokes equations, however modified by the Reynolds decomposition from equation 2.4. The Reynolds averaged form takes all instantaneous velocities u_i and expands out for the fluctuation component u_i' and the $\overline{u_i}$ mean component. After some rearranging the Reynolds averaged Navier-Stokes equations transform into:

$$\frac{\partial \overline{u_i}}{\partial x_i} = 0 \tag{2.12}$$

$$\rho\frac{\partial\overline{u}_i\overline{u}_j}{\partial x_j} = -\frac{\partial\overline{p}}{\partial x_i} + \frac{\partial}{\partial x_j}\big(\mu\frac{\partial\overline{u_i}}{\partial x_j} - \rho\overline{u_i'u_j'}\big) \tag{2.13}$$

Equation 2.13 has eliminated the time derivative assuming it is a steady flow but has come up with the aforementioned Reynolds stress term. This presents a large problem for the solution of the RANS equations since we are left with a larger number of unknown variables (ten) than we have equations (four). This famous closure problem concerning the Reynolds stresses is tackled by the Boussinesq hypothesis (Schmitt, 2007) in equation 2.14, which introduces a new concept to model the Reynolds stress tensor.

$$-\rho\overline{u_i'u_j'} + \frac{2}{3}\rho k\delta_{ij} = \rho\nu_T\overline{\mathbf{S_{ij}}} \tag{2.14}$$

The introduction of the eddy or turbulent viscosity ν_T models the Reynolds stress by multiplying it with a term proportional to the mean strain $\overline{\mathbf{S_{ij}}}$. The right hand side of equation 2.14 is the result of the difference of the Reynolds stresses from the overall kinetic energy. However the modelling of Reynolds stresses by an averaged stress tensor does eliminate all fluctuations from the chaotic flow, even if keeping the kinetic energy term.

The main "workhorses", long used as standards within RANS modelling are the so called two-equation models. The $k-\epsilon$ and $k-\omega$ models operate on equations that model the transport of the turbulent kinetic energy k and an additional term for either turbulent dissipation ϵ or the closely related specific-dissipation rate $\omega = \epsilon/k$.

2.4.1.1 k-ϵ two-equation model

Equations 2.16 and 2.17 are the transport equations for the turbulent kinetic energy k and the turbulent kinetic dissipation ϵ respectively. Whereas Equation 2.15 creates a relationship between the TKE and ϵ to calculate the turbulent viscosity as per the Boussinesq hypothesis.

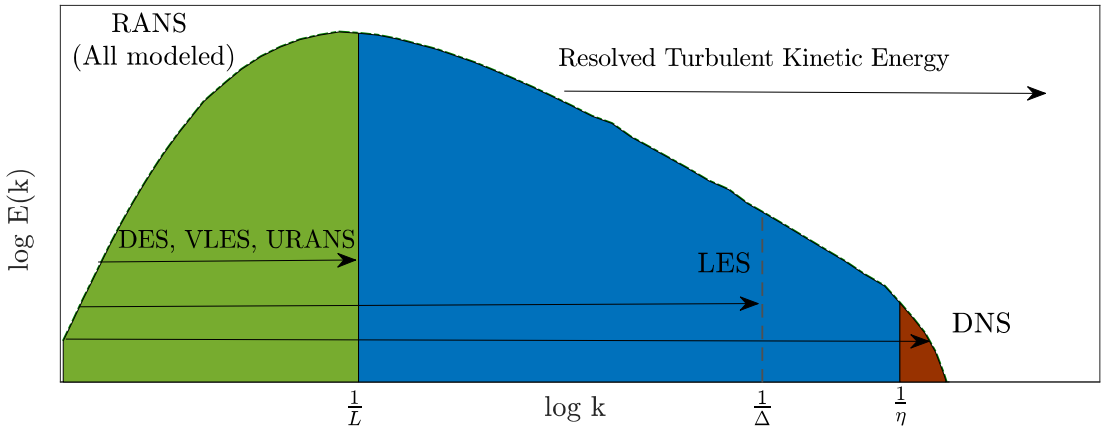

Figure 2.2: Resolved component of turbulence spectra for turbulence models

$$\mu_t = \rho C_\mu \frac{k^2}{\epsilon} \tag{2.15}$$

$$\frac{\partial}{\partial t}(\rho k) + \nabla(\rho k \overline{\mathbf{u_i}}) = \nabla\big[(\mu + \frac{\mu_t}{\sigma_k})\nabla k\big] + P_k - \rho(\epsilon - \epsilon_0) + S_k \tag{2.16}$$

$$\frac{\partial}{\partial t}(\rho \epsilon) + \nabla(\rho \epsilon \overline{\mathbf{u_i}}) = \nabla\big[(\mu + \frac{\mu_t}{\sigma_e})\nabla \epsilon\big] + \frac{1}{T_e} C_{\epsilon 1} P_\epsilon - C_{\epsilon 2} f_2 \rho (\frac{\epsilon}{T_e} - \frac{\epsilon_0}{T_0}) + S_\epsilon \tag{2.17}$$

Production terms P_k, & P_ϵ are model specific terms composed of buoyancy, shear and turbulent non-linear production terms. Time scales T_e and T_0 represent the time the kinetic energy takes to dissipate through a relationship k/ϵ.Initial ambient dissipation ϵ_0 and kinetic energy $k_0 = \epsilon_0 T_0$ conditions play a strong role in countering turbulent decay. While $\sigma_{k,e}$ and $C_{e1,e2}$ are model coefficients equal to: 1, 1.3, 1.44 and 1.92 respectively for the standard k-ϵ by Launder and Spalding (1974) and as presented by the user guide of Star-CCM+ Siemens (2018).

2.4.1.2 k-ω two-equation model

The $k - \omega$ model was devised by Wilcox (2006) as an improvement over the $k - \epsilon$ treatment of strong shear flow near the wall. Since the objective of this chapter is

to provide insight on the existing turbulence models, only the Standard $k-\omega$ model formulated by Wilcox (2006) equations will be shown as used by Siemens (2018), although there are many variants that have been developed over the years improving upon the classic formulation. Once again the formulation begins with a modelling of the turbulent viscosity, this time utilizing the TKE and the specific dissipation rate ω. ω shows the rate at which the exiting turbulent kinetic energy is dissipated into thermal energy in terms of time (1/s) with a relationship ϵ/k. Both values are then transported in equations 2.19 and 2.20.

$$\mu_t = \rho k T \tag{2.18}$$

where T is the turbulent time scale computed by $T = a/\omega$, in which a is a model coefficient equal to 1 in the Standard model.

$$\frac{\partial}{\partial t}(\rho k) + \nabla(\rho k \overline{\mathbf{u_i}}) = \nabla\big[\big(\mu + \mu_t s_k\big)\nabla k\big] + P_k - \beta^* \rho(\omega k - \omega_0 k_0) + S_k \tag{2.19}$$

$$\frac{\partial}{\partial t}(\rho \omega) + \nabla(\rho \omega \overline{\mathbf{u_i}}) = \nabla\big[\big(\mu + \mu_t s_\omega\big)\nabla \omega\big] + P_\omega - \beta \rho(\omega^2 - \omega_0^2 + S_\omega \tag{2.20}$$

Model constants are: $\beta^* = .09, \beta = 0.72, s_k = -0.6, s_\omega = 0.5$. While ω_0 and k_0 are initial conditions that help counteract turbulence decay.

There are several other families of RANS models ranging from one-equation models (Spallart-Allmeras) to highly sophisticated second order closure models (Reynolds Stress Transport models), each with their unsteady variant. Yet, all of these models still fall under the modeled unresolved treatment of turbulent eddies. Unsteady effects are lost under these models, even if they are very capable of giving us a cheap quick accurate enough idea of the turbulent energy in the flow. It is necessary to look to higher capability models if discussing true turbulent simulation.

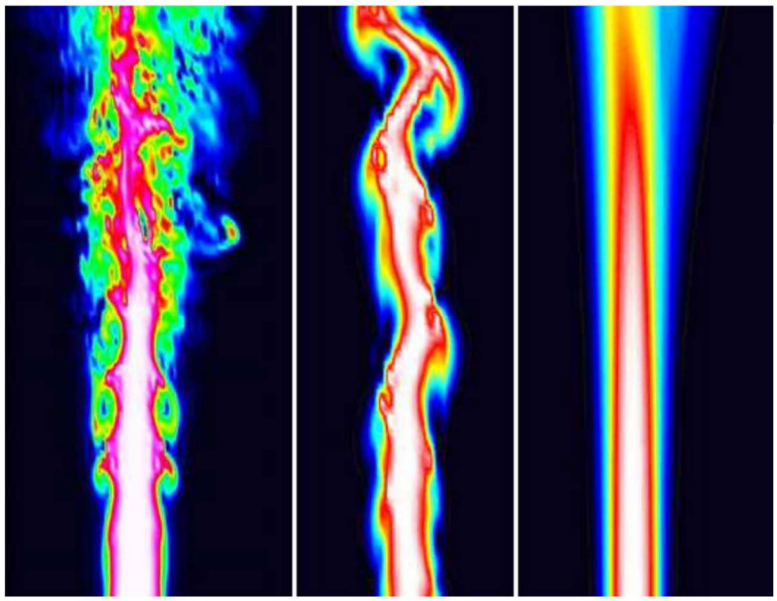

Figure 2.3: DNS (left), LES (middle) and RANS (right) predictions of a turbulent jet. Maries et al. (2012)

2.4.2 Scale Resolving Turbulence Models

LES simulations function on a similar mathematical decomposition as the RANS models, yet under a completely different concept. The LES decomposition is divided into a filtered component $\widetilde{u_i}$ and a sub-grid component u_i' for velocity fields u_i.

$$u_i = \widetilde{u_i} + u_i' \tag{2.21}$$

$$\widetilde{u_i} = \iiint_V G(x_i - x_i', \Delta) u_i \, dx_i' \tag{2.22}$$

Here G is a filter function, proportional to a filer size $\Delta = (\Delta_{x_i}\Delta_{x_j}\Delta_{x_k})^{1/3}$. As the filter size decreases in an LES model results become quasi-DNS, leaving the subgrid component negligible. Equation 2.23 shows the result of using the decomposition from equation 2.21 for the constant property Navier-Stokes momentum equation.

$$\frac{\partial \widetilde{u_i}}{\partial t} + \widetilde{u_j}\frac{\partial \widetilde{u_i}}{\partial x_j} = \frac{1}{\rho}\frac{\partial \widetilde{p}}{\partial x_j} + \frac{\partial}{\partial x_j}\left(\nu \frac{\partial \widetilde{u_i}}{\partial x_j}\right) + \frac{1}{\rho}\frac{\partial(\widetilde{u_i}\widetilde{u_j} - \widetilde{u_i u_j})}{\partial x_j} \tag{2.23}$$

It becomes clear in the last term that the Reynolds stress tensor runs into the same closure problem as before.

2.4.3 Sub-grid scale Models

As a consequence of the inequality between the terms $(\widetilde{u_i}\widetilde{u_j} - \widetilde{u_i u_j})$ the Boussineq hypothesis must be used once more. This introduces the turbulent viscosity in a similar way to the RANS equations, to be able to calculate the sub-grid contribution. Each subgrid model will equate the μ_t in a different way for each model, yet always related to a spatial filter size Δ.

Several sub-grid scale models are currently in use for commercial and open software packages or variations of them. In the interest of brevity, we will mention the workings of the three most used: Smagorinsky, Dynamic Smagorinsky and WALE (Wall Adaptive Large Eddy).

2.4.3.1 Smagorinsky Subgrid Scale

The first of the subgrid scales commonly used was developed by Smagorinsky (1963) and later refined by Lilly (1967), thus sometimes going by the name of Smagorinsky-Lilly model. The subgrid model was first developed to deal with atmospheric boundary layers, which dealt mostly with larger sized eddies and did not need an extreme level of accuracy for smaller eddies. The closure issue was addressed in equation 2.24 finding a value for the turbulent viscosity proportional to the strain rate by a Δ filtered length scale usually related to a grid cell size. This length scale may be limited for accuracy and stability.

$$\mu_\tau = \rho\Delta^2\widetilde{\mathbf{S_{ij}}} \tag{2.24}$$

$$\Delta = \begin{cases} f_v C_s V^{1/3}, & \text{no length scale limit} \\ f_v min(\kappa d, C_s V^{1/3}, & \text{if length scale limited} \end{cases} \tag{2.25}$$

C_s is the Smagorinsky coefficient equal to 0.1, yet requires a certain amount of tuning depending on the flow. $\kappa = 0.41$ is the von karman constant and f_v is the Van Driest damping function (Driest, 1956) while d is the distance to the wall. The tuning of the Smagorinsky coefficient for different flows led to the development of the Dynamic Smagorinsky coefficient that changes without necessary user tuning.

$$f_v = \begin{cases} 1, & \text{no damping used} \\ 1 - e^{(-\frac{y^+}{25})}, & \text{standard damping used} \\ \sqrt{1 - e^{(-\frac{y^+}{25})^3}}, & \text{modified damping activated} \end{cases} \tag{2.26}$$

The Van Driest function is important in wall bounded flows for stability and accuracy of the filtering process at smaller scales occurring next to the wall. Common issues with the model was problems dealing with backscatter(energy transfer from smaller to larger eddies), over prediction of near wall dissipation and changing strong shear near walls. Some of these issues have been solved or at least treated by later developments.

2.4.3.2 Dynamic Subgrid Scale Model

The dynamic Smagorinsky model was developed by Germano et al. (1991) and later modified by Lilly (1992). The Navier-Stokes equation undergoes a second filtering to find a C_s for each time step dependant on the length scale for the local cell volume. Equation 2.27 shows the filter relationship to the local volume cell while equation 2.28 is the relationship to calculate the eddy viscosity from the strain and filter size.

$$\Delta^2 = C_s^2 V^{2/3} \tag{2.27}$$

$$\mu_t = \rho \Delta^2 S \tag{2.28}$$

The second filtering is calculated for each cell by comparing it to all of the neigh-

boring cells. Equation 2.29 shows how variables (represented generically as ϕ) are averaged for all of the cells next to the one undergoing the second filtering. Subscript 0 refers to the cell itself while its neighbors are numbered from 0 to N.

$$\widetilde{\widetilde{\phi}} = \frac{1}{\sum_{n=0}^{N} V_n} \sum_{n=1}^{N} \widetilde{\phi_n} V_n \tag{2.29}$$

Thus the last term of the Navier-Stokes LES equations (2.23) is named as the tensor $\mathbf{L_{ij}}$. Equation 2.30 is a model tensor that helps calculate the final Smagorinsky coefficient from the difference between filtered $\mathbf{L_{ij}}$ in equation 2.31.

$$\boldsymbol{M_{ij}} = 2\tilde{L}^2 \left(|\tilde{S}|\widetilde{S_ij} - \frac{\widetilde{L^2}}{\widetilde{L^2}} |\tilde{S}\widetilde{S_ij} \right) \tag{2.30}$$

$$C_s^2 = \frac{\overline{\boldsymbol{L_{ij}} \boldsymbol{M_{ij}}}}{\overline{\boldsymbol{M_{ij}} \boldsymbol{M_{ij}}}} \tag{2.31}$$

It is recommended, for stability and convergence reasons to keep the Smagorinsky coefficient within a minimum and maximum range as well as the ratios between each filtering generic variables.

The WALE sub-grid scale will be explained in detail in Chapter 3. It is important to introduce the model when discussing the entire simulation description, as it was the model used for the body of work. High shear values near the seabed wall and complex geometries were the main reason for choosing the WALE model. Smagronisky sub-grid models are too dependant on fine tuning the C_s coefficient leaving only dynamic Smagorinsky and WALE as options within the software package available even for cases of idealized turbulent flow (Jeanmart and Winckelmans, 2002). Ma et al. (2008) compared the aforementioned subgrid models for complex geometries of turbulent flow for water turbines. This comparison showed WALE to be the best performing subgrid model, followed by the dynamic Smagorinsky, particularly in predicting pressure distributions.

Engineering applications may require further fidelity than RANS model solutions, without falling under the complexity of LES simulations. Intermediate models

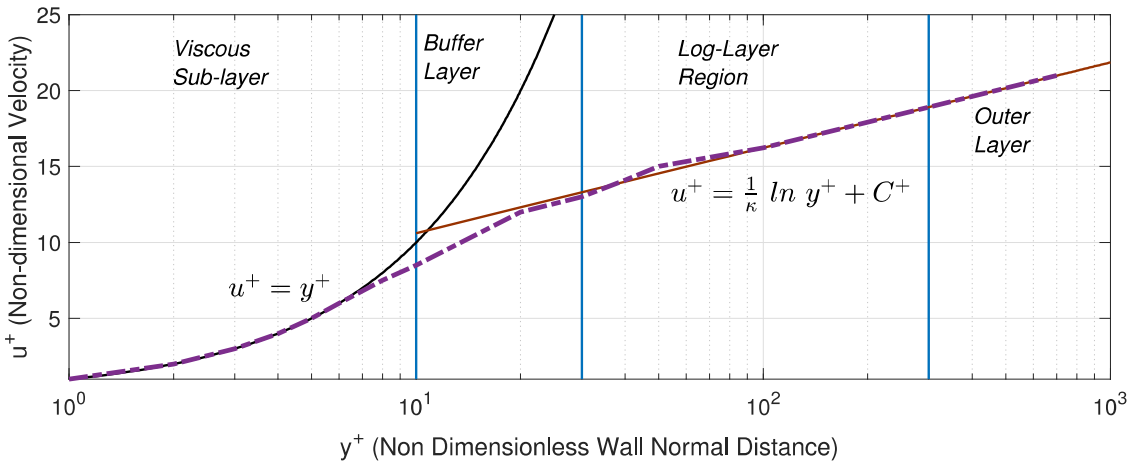

Figure 2.4: Wall Treatment models

such as the aforementioned DES or VLES are typically used for resolution of only the largest integral length eddies, although are dependent on cell resolution size and could capture smaller eddie regions. LES itself may be used in a less stringent manner by combining it with near wall models to become wall modelled large eddy simulation (WMLES). Wall models take over the most strict of resolution requirements near the wall, enabling a discounted version of LES.

2.4.4 Wall Modelling

Turbulent boundary layers and channel flows fall under the strong influence of their walled boundary conditions. The strong shear gradient at the wall can create large resolution requirements to capture the vorticity, shear and velocity gradients. Velocity gradients increase with accelerating Re near the wall, making it impossible in practical computational terms to resolve the smallest turbulent scales. Models have been constructed to predict the velocity gradient for control volumes near the wall.

Flow can be divided into an inner region (viscous, buffer and log-law layers) and an outer region if seen in a wall-normal direction, as first mentioned in Chapter 1. Velocity profiles behave differently from region to region. The viscous sub layer is dominated, as its name suggests, by viscous forces and time scales. The strength of the viscous forces is usually measured by the wall shear stress τ_w. Wall shear stress

can be defined as follows:

$$\tau_w = \mu \frac{\partial \overline{u_i}}{\partial x_j} \tag{2.32}$$

From the wall shear stress a velocity scale can be defined as u_τ or friction velocity.

$$u_\tau = \sqrt{\frac{\tau_w}{\rho}} \tag{2.33}$$

where ρ corresponds to the density of the fluid. The friction velocity can be used as a scale to non-dimensionalize flows parameters in terms of their viscous effects. Equations 2.34 and 2.35 show how the friction velocity non-dimensionalizes the wall normal position y and velocities u to contextualize scales for all flows.

$$y^+ = \frac{u_\tau y}{\nu} \tag{2.34}$$

$$u^+ = \frac{u}{u_\tau} \tag{2.35}$$

Figure 2.4 shows the behavior of the velocity as it extends from the viscous sub-layer into the outer layer. Wall-normal locations from $0 < y^+ < (6 - 10)$ behave in a manner fitting the equation $u^+ = y^+$. The log-layer is named as such due to its behaviour following the equation:

$$u^+ = \frac{1}{\kappa}\, ln\ y^+ + C^+ \tag{2.36}$$

where κ is the Von Karman constant and is usually approximated to 0.41 and C^+ is a constant dependent on smooth or rough walls, yet set as equal to 5 for smooth flows as recommended by the Star-CCM+ package. This constant can be tuned if the exact roughness of the wall is known for a better fit near the wall. The precise location of the beginning of the log-layer is a point of contention and highly flow

dependent. However, several CFD packages such as Star-CCM+ establish a default value of $y^+ = 30$. It is the behavior in the buffer layer which does not fit any of the latter equations for the viscous sub layer or the log-layer, it is important that the first cell not be in the buffer layer to have an accurate wall modelling of the velocity.

2.5 Summary

The basics of turbulent motions and their modelling have been presented with the objective of having a clear picture of concepts that will be the focus for the analysis of tidal energy sites. Turbulent modelling concepts need to be understood to be able to make the best decision when creating the numerical model of the Fall of Warness.

Offshore flows are turbulent environments at such a high Reynolds number that it would be amiss to not see turbulence as a major player when studying them. The basics of turbulence and its parameters (Reynolds decomposition, Reynolds stresses, spectrum etc.) show the importance of viewing turbulent flows not only as mean flows but as a statistical phenomena where fluctuations play as important or more of a role than the mean flow. The energy content of the flow will be broken up in a great number of time and space varying scales. Each one of these scales contributes in its own way to the energetic structures that will interact with tidal energy converters.

In a perfect world with unlimited resources every simulation would be run as a DNS simulation to have near experimental levels of data. Yet it is clear that in engineering applications speed and accuracy must be balanced for an appropriate answer that can be used in the analysis and design process. Not every researcher has the time or computer to run unlimited number of simulations or computational power for real world solutions.

Tidal Energy device development require a strong level of fidelity for both mean and transient loads. While it would be simple to keep using RANS models as numerical tools, boundaries must be kept pushed forward. LES appears to be the driving direction of numerical modelling as computational power grows accessible,

and it's use may be aided by additional coupled models for further accuracy. Thus it is concluded that LES is the best realistic option available to study the turbulent phenomena of tidal marine sites, and has been chosen as the numerical tool used for the remainder of the work in this thesis in it's WALE sub-grid version.

CHAPTER 3

LITERATURE REVIEW

3.1 Tidal Energy Numerical Modeling

Although our understanding of the sea state has been enriched by the many previously mentioned surveys of tidal energy sites, both laboratory and numerical model experiments allow us to create representative environments that study the physical phenomena of the sea. Both methods are carried out in a manner that permit us to isolate variables in controlled settings. Previous experiments have been an effort at understanding the different components and scales within tidal energy devices, ranging from entire coastlines to singular elements within the device.

3.1.1 Regional Scale Ocean Models

The largest scale of marine energy physics modelling is in the realm of regional ocean models. Regional ocean models are numerical codes that attempt to solve for areas in the order of kilometres up to entire seas, oceans and global current systems. They are a powerful tool when studying tidal energy sites due to their large reach, rapid run-times and their long history and use. Tidal energy regional modelling has been attempted for many locations such as the Pentland Firth in Scotland (Adcock

et al., 2015; Robins et al., 2015), Wales(Togneri et al., 2017), Puget Sound (Thyng et al., 2013), Norway (Grabbe et al. (2009) has an ample review of the models and resource assessments done in Norway) and the Orkney Islands, amongst others.

The Fall of Warness, in particular, has been studied using regional models to study the effects of the flow for entire site scale using a mixture of open source code (ROMS,Delft3D) or commercial codes (Mike21, Mike3) (Neill et al., 2014; Lawson et al., 2011; Waldman et al., 2017; Venugopal and Nemalidinne, 2014). Assessment of the site was analyzed by Venugopal and Nemalidinne (2014) taking into account not only tidal velocities but attempting to include the effect of waves on the oceanic free surface.Venugopal and Nemalidinne (2014) coupled wave and 3D tidal flow numerical models aided by site measurement data for more realistic inflow boundary conditions, a technique that would later be used by several other modelling methodologies. Larger regional models have been used not only for resource assessments but also as industry standard models capable of modelling energy extraction and flow modifying effects of tidal turbines. Waldman et al. (2017) showed that Delft3D and MIKE 3, can be used both accurately to predict the bed stress and depth-averaged current speed for the entire area modeled. Waldman et al. (2017) does underline the use of these regional models for mainly larger purposes. Smaller scale effects at a turbine scale should be attempted with other numerical models. This limitation leads us to look at other numerical modelling tools when seeking an understanding of local instabilities that have a direct impact on the tidal turbine and its components. It is important to note that while the regional ocean models can make assumptions on the flow (depth or time averaged) that make them, while computationally cheaper, less accurate when looking for small scale local turbulent parameters.

3.1.2 Computational Fluid Dynamics Models

Computational fluid dynamics (CFD) modelling is a much used and powerful tool, used for diverse applications in fluid dynamics over a spectrum of scales. CFD modelling greatly aids fluid dynamic research by making numerical experiments available to gather comprehensive details of the flow and its interaction with submersed struc-

tures. It is important to highlight that every CFD simulation/model always carries a *caveat emptor*. The data gathered is the result of modelling considerations, and is not without discretisation and modelling assumption errors for the corresponding physics. CFD constraints for tidal energy flow models are particularly linked to the high Reynolds number of tidal energy flows ($Re \approx 10^7$) and the corresponding high computational cost when meshing and time stepping. Models range in complexity from computationally cheap Reynolds averaged models to scale dependant resolving models (Detached eddy and large eddy simulations) and finally direct numerical simulations that are prohibitively expensive for most engineering purposes. Every model has it's advantages and disadvantages depending on the objective of the modeler. RANS models continue to be the workhorse in the CFD community for simulations that require speed over accuracy or time-discrete values. More complex models increase in fidelity as they pay the price in computational expense and time.

Several simplifications are done to tidal energy extraction devices to be able to model the interaction of the domain and the device in CFD models. Reynolds Averaged Navier Stokes models (RANS) were used with great success by Afgan et al. (2013); McNaughton et al. (2012); Batten et al. (2013); Turnock et al. (2011). Ahmed et al. (2015) coupled a large eddy simulation with porous disc model and blade element momentum theory models (BEMT) in an effort to get around the high Reynolds meshing requirements for complete blade resolving of tidal turbines. Creech et al. (2017) used actuator line modelling coupled with a resolved device structure to study wake effects and unsteady characteristics in device performance. The modelling of the flow domain was not of particular interest to the aforementioned studies, rather a view of the turbine performance and loading curves. Domains were simplified as flat channels, at times enhanced by turbulent inflows using turbulence generator methods. The Synthetic Eddy Method (SEM) (Jarrin et al., 2006) was compared to the Von Karman spectral approach by Gant and Stallard (2008) for tidal streams. Both methods were observed to decay rapidly from the inflow as the shear rate did not produce enough turbulence to balance dissipation.

Ahmed et al. (2015) and Creech et al. (2017) stood out in their use of the Syn-

thetic Eddy Method (SEM) coupled with Large Eddy Simulation (LES) turbulence models to simulate coherent turbulence in the domain based on depth profiles from previous simulations or site measurements. The same method would prove to be useful in modelling the EMEC site turbulence characteristics for the present study in combination with highly resolved turbulence models.

Afgan et al. (2013) and Ahmed et al. (2015) showed the furthered capabilities that LES could achieve in comparison to RANS, specially with regards to for tidal streams and their flow environments. Afgan et al. (2013) upon comparing the two models found an under prediction of turbulent kinetic energy in flow regions far from tidal turbines and the outlet. Due to its averaged nature, RANS could not capture the detached tip vortices that transport turbulent kinetic energy. The study recommended use of LES modelling over RANS when seeking deeper insights into the flow-physics of the domain. Ahmed et al. (2015) supported the use of LES over RANS when possible in a blade resolved simulation coupled with data from the EMEC test site, seeking to best capture the turbulent statistics from site measurements. Only LES was found to be able to capture a representative spectrum of the flow turbulence. Results from Ouro and Stoesser (2018) LES simulation of a turbine on a dune at a laboratory scale showed how turbulent statistics can drastically modify turbine performance and stresses. The study went further in emphasizing the need for further research into bathymetry in tidal flows.

LES turbulence models allow for greater resolution of the turbulent eddies bursting from the seabed, vortices shedding from turbine blades and of the coherent structures that are continually produced by the flow. In the present work, the modelling of turbulence in LES shows the importance of instantaneous bursting events in the context of a larger period of time within the flow. Statistical analysis of discrete events have aided in the description of turbulence structure and turbulent kinetic energy production, from both an experimental perspective (Lu and Willmarth, 1973; Willmarth and Lu, 1972; Milne et al., 2017; Wu and Christensen, 2007) as well as supported by numerical simulations (Yue et al., 2007; Spalart, 1988; Omidyeganeh and Piomelli, 2013a).

The use of LES on rough seabed floors has not been developed beyond roughness effects for high resolution realistic bathymetries, as to the knowledge of the author. However, a number of LES topographical simulations of wind energy sites have been developed over the long history of wind energy in comparison with tidal. Although not fully analogous to the atmospheric flow of wind turbines, tidal current flows may use previous lessons of the wind industry to develop its own standard. The depth of the water column for tidal environments is of magnitudes lower than the required modelled height for atmospheric boundary layers. This is advantageous to the modelling of oceanic water column even after the taking of account of different Reynolds number.

Topographical simulations were developed with the primary purpose of understanding how separation from hills interact with the wind turbine wakes of different sizes. Yang et al. (2015) was one of the first to do an exhaustive study using increasingly larger hill sizes and comparing it to flat bottom simulations as has been the norm for both tidal and wind simulations, be it averaged models (RANS) or scale resolving models (LES, DES or similar).

Han et al. (2016); Bechmann et al. (2010); Breton et al. (2017) successfully show the use of complex bed forms to predict and generate turbulence at device scale for turbulent resolving models for realistic wind energy sites. The use of high resolution Large Eddy Simulation (LES) models of turbulent sites, in tandem with site data injections of turbulence as well as irregular site bathymetry create a powerful tool when analyzing the fluid dynamics of the site and allows for improved insight of the structure and scale of turbulent flow.

Uchida (2017) stands out as an LES realistic topography simulation as it showed precise information of the vortices near the lower ground boundary. The scale of the site was 6 x 1.44 x 2 km with a 20m spanwise and streamwise resolution. Vertical meshing, due to the height of the atmospheric boundary layer reached up to 288m. Roughness blocks were used to induce turbulence at the inflow. The simulation demonstrated the capabilities of LES-topography simulations to select the optimum locations for wind turbines. Uchidas analysis shows how topography can create

vortex shedding that are capable of reaching turbine blade heights and affect its performance.

Shamsoddin and Porté-Agel (2017) developed a LES in constant feedback with field data to validate and improve the model of a wind turbine site at Brent Knoll in Somerset. The geometry used is similar to the idealized bumps and dunes from past LES research (Stoesser et al., 2007; Fröhlich et al., 2005a; Chang and Constantinescu, 2013; Xie et al., 2013). Turbulence was generated by precursory simulations of a flat boundary layer. Shamsoddin and Porté-Agel (2017) cite the need for more realistic topographies to truly be able to validate in comparison with experimental databases. Vortex shedding from sharp contrasts in the geometry act as a strong modifier of turbine wakes.

LES simulations require high level of confidence in spatial resolution quality to properly understand the frequencies being solved. Sub-grid comparison was analyzed by Laval et al. (2011), by comparing meshing requirements needed for a converging-diverging turbulent channel flow simulation. Laval et al. (2011) highlighted the need of sufficient streamwise resolution for high Reynolds numbers, in this case $Re_\tau > 395$. Further LES meshing guidelines will be highlighted in the numerical modelling chapters but readers should be referred to Celik et al. (2005, 2006, 2009); Davidson (2009).

Both convergent-divergent geometry LES models by Laval et al. (2011) and Shamsoddin and Porté-Agel (2017)'s hill LES simulations show turbulence intensities being modified from flat wall simulations in a manner similar to the asymmetrical ebb flows reported by Ouro and Stoesser (2018) at streamwise positions after a decline in the wall topography.

The use of LES for energy sites modelling, even with complex topography, has been well established. Best practices for meshing and quality control have even begun to be standardized. However, at the time of this work being written little research has been taken that has had the primary objective of studying the effects of the topography on the coherent structures and turbulence statistics themselves, without involving any energy capturing devices. Zangiabadi et al. (2015) developed

a site scale simulation of the Ramsey Sound in Pembrokshire, Wales. The simulation was of a sufficient area large enough to capture the fluid dynamics of the site (800 m x 1800 m), the site had elevation deltas of up to 80m making it a perfect domain to analyze drastic changes in bathymetry depth. However, the study showed a resolution too coarse to sufficiently resolve device scale characteristic coherent structures. Results were encouraging for future uses of LES for tidal sites, it did capture larger eddies and their pressure modifications close to the surface.

Recent advances in computational resources and improved knowledge on large eddy simulations lay the groundwork for future analysis of realistic tidal energy flow. The exhaustive work in the literature shows the need for realistic boundary conditions at the inflow and at the bottom seabed boundary for adequate turbulent kinetic energy production. The shear stress from the seabed is bound to create complex turbulent interactions and lasting coherent vortices previously not captured by larger numerical models yet well known in the field of fundamental fluid dynamics.

3.2 Turbulence & Coherent Structures

The characteristics of tidal sites identified for energy extraction are strongly influenced by turbulent flow and coherent structures, which are produced and dissipated by a myriad site-dependent features. These unique site features create uncertainty in predicting flow conditions, which can influence the design and maintenance program of tidal energy devices. An increase in turbulence intensity of just 10% has been found to decrease power output up to 10% and highly increased fatigue loading uncertainty (Blackmore et al., 2016). Figure 3.1 by Ouro and Stoesser (2018) shows the tidal turbine environment and the main flow variables at play that interact to produce, dissipate or transport the turbulent flow. In a turbine-less environment the most important driver is the seabed. Larger coherent structures or eddies are present far away from the seabed closer to the turbine rotor, while smaller structures are strongly linked to the seabed itself.

However, before beginning to discuss them we must first define what a coherent

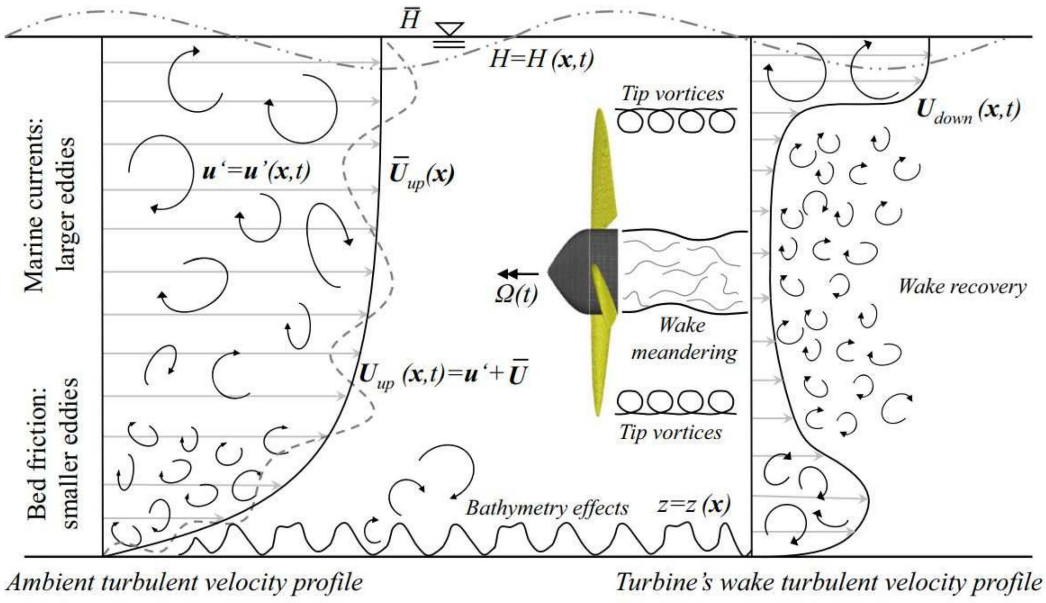

Figure 3.1: Tidal Turbine Flow Environment Phenomena as seen in Ouro and Stoesser (2018).

structure is and why they matter so much for a turbulent environment. The preferred use of the term is defined by Jeong and Hussain (1995), who call them connected organized turbulent fluid masses, coherent in sufficient time and space as to be visible after statistical averaging of instantaneous fluctuations. They are active in the energy dynamics of the flow, continually moving, dissipating and/or generating turbulent energy. Thus any study of turbulent flow must take into account possible coherent structures to understand the character and strength of turbulence in an environment.

Coherent structures come in various shapes and sizes. Marusic and Adrian (2010) and Robinson (2002) provide excellent review and discussion on the taxonomy of coherent structures. The length scales mentioned, in descending order, are very-large scale motions (VLSM), large scale motions (LSM), bursting events and dissipation length scales. Figure 3.2 shows the vertical layers of a typical ocean flow from the seabed (be it smooth or rough) to the moving free surface. The viscous sublayer is dominated by viscous length scales (ν_τ) and effects. The buffer layer connects the viscous sublayer to the log layer where the velocity profile has a logarithmic behavior

and finally the outer layer where the bulk of the flow is located. Further discussion of the theory will be seen in Chapter 3. The size of the eddies does decrease from the outer layer to the smallest in the viscous sublayer, on and on until dissipation. Smith et al. (2005) categorizes turbulence near the seabed of the ocean by temporal and spatial size. Larger scale turbulence is named as intermittent high energy gusts versus smaller anisotropical scales. Gusts changed the structural nature of ocean turbulence into streamwise dominant scales that scaled with the Reynolds number independently from surface waves. These gusts were deemed by Smith to be closely linked to the hairpin vortices mentioned by Adrian et al. (2001). Hairpin vortices, closely linked to the structures called horseshoe vortices by Theodorsen (1952) are vortice filaments traveling in the direction of the mean flow tilted in the opposite direction of the wall (see figure 3.3). Hairpins appear at high Reynolds number, as the legs of the horseshoe vortex come closer and closer together with an increasing Re and elongating as it blends in with the rest of the hairpins in the packet (Head and Bandyopadhyay, 1981; Smith, 1984). Adrian (2007) linked the hairpin packets to turbulent producing bursting events, these are violent intermittent energy rich vortices that may either be "erupting "(fluid moving against the wall) or "sweeping" (rapid flow moving towards the wall from the outer layer) first touched on in research by Willmarth and Lu (1972); Moin and Kim (1982). These hairpin vortices were found in the log layer and sometimes even in the outer layer, up to 20% of the water column for a boundary layer flow at higher Reynolds numbers (Christensen and Adrian, 2001; Perry et al., 1995). In terms of oceannic flows Steele et al. (2016) shows an experimental analysis of the three dimensional flow in the bottom boundary layer of a 1.5 m/s ebb tide near the seabed. Steele et al. (2016) found vortices with occurring every 4.3 s within the log layer (see figure 3.2 for visual location of the log law). The vortices travelled in increasingly large scale packets continuously decreasing in size as location neared the seabed.

Larger scale motions were found to be of the scale of a 2-3 times the boundary layer thickness (δ) or the half channel height in the log and outer layers by Kim and Adrian (1999). The energy content of LSM or VSLM structures only increases

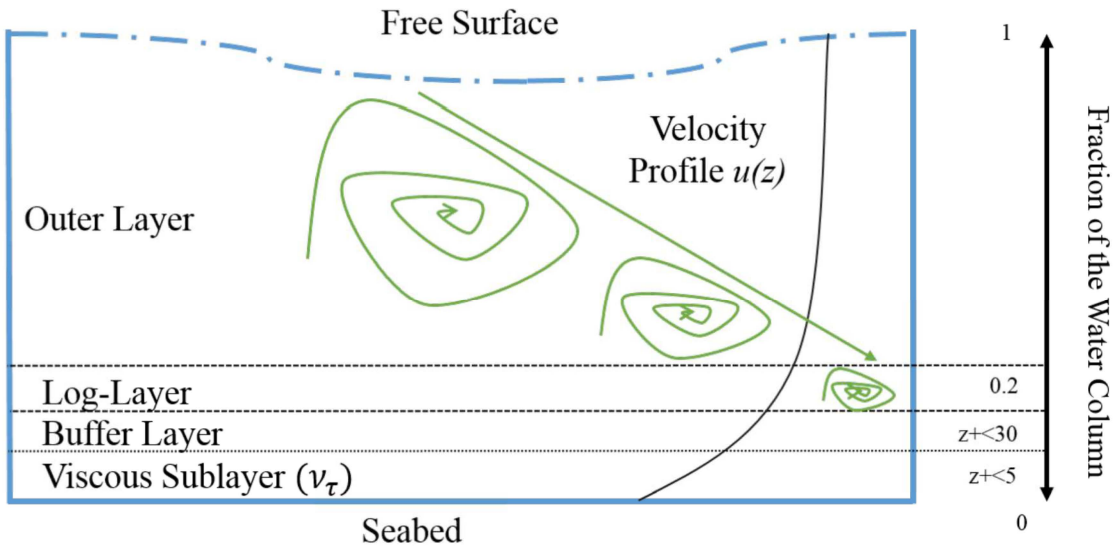

Figure 3.2: Vertical Structure of the Water Column

in importance at higher Reynolds numbers, reaching up to 65% of the TKE budget (Balakumar and Adrian, 2007), while Smits et al. (2011) suggests that they are the modulating mechanism for peaks of near-bed Reynolds stress.

The effect of irregular surfaces or wall roughness on turbulence structures for boundary layer flows and channel flow has been well studied. Turbulence structure dependence and velocity profile divergence from smooth channels have been analyzed for cube roughened surfaces (Cui et al., 2003; Leonardi et al., 2004), 2D and 3D surface roughness (De Marchis and Napoli, 2012; Choi et al., 2001; Antonia and Krogstad, 2001) in addition to realistic urban surfaces (Xie et al., 2008), aforementioned wind energy site topography Bechmann et al. (2010) or plant canopies (Yue et al., 2007).

Antonia and Krogstad (2001) specifically showed how anisotropy is decreased in rough flows in comparison to smooth surfaces. The same was found in Xie and Castro's Xie et al. (2008) work for urban environments; both agreed on finding higher level of bursting events above roughness elements. Grass (1971), in an experimental study of boundary layer turbulence, found an increase of 30-90% shear stress and TKE production for rough surfaces. Bursting events were seen to increase in scale, production and frequency. This was supported by research done by Ashrafian and

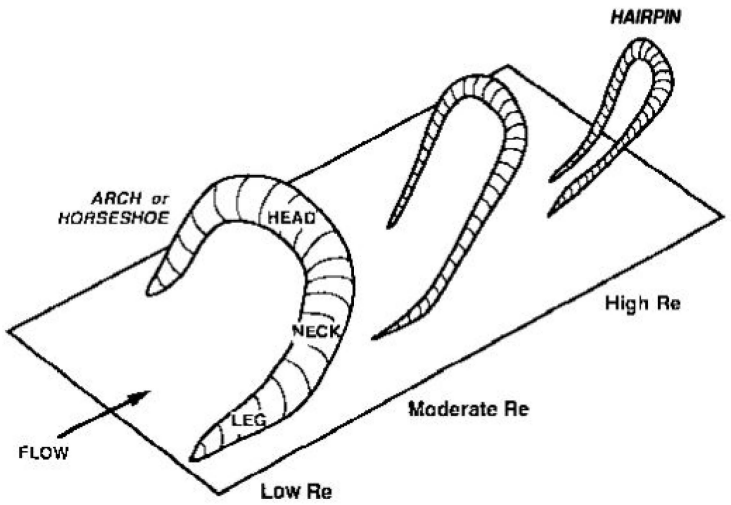

Figure 3.3: Evolution of horseshoe vortices to hairpin vortices as Reynolds number increases. (Robins et al., 2015)

Andersson (2006), however adding that the effect of the eddies shed from roughness elements was mostly dissipated in the outer layer of the floor.

The ratio between the height of the irregular feature to the total depth of the water column was found to be a metric of the influence of the turbulent bursts (Fröhlich et al., 2005b; Jimenez, 2004). And, due to a lower ratio at tidal sites the applicability of some of these studies cannot be fully realistic and allow for greater improvement in research. Research into non-uniform bed forms in turbulent flows has been an ongoing endeavour; both experimental and numerical simulation work have been carried out with regards to topographical features such as dunes, periodic hills and other surface roughness based domains at different scales. Past work has been mostly focused on local topographical irregularities such as dunes (Yue et al., 2005; Stoesser, 2013), periodic channels (Fröhlich et al., 2005b) at a very high resolution and in certain cases (De Marchis and Napoli, 2012; Omidyeganeh and Piomelli, 2013b,a; Krogstad and Antonia, 1999) at the collection of the irregularities, roughnesss and their interaction for 2D and 3D cases.

In summary, it can be seen that the turbulent statistics of high energy events and structure are a fundamental part of site resource assessment for tidal energy devices. The interaction of site hydrodynamic characteristics with tidal turbines creates a

complex system that will have a major impact on the feasibility and design of future tidal energy arrays. The combination of waves, current, bathymetry and turbulence lead to intricate interactions affecting the ocean flow field. It is of considerable interest to tidal energy engineering to have the most complete understanding and data of turbulent phenomena as possible using combinations of numerical, laboratory and site survey analysis. Thus a functioning working model is needed that can work as a tool that covers the majority of the aforementioned phenomena while remaining accessible within engineering design analysis constraints.

CHAPTER 4

SIMULATION DESCRIPTION

4.1 Introduction

This chapter aims to discuss the design of a group of simulations created with the objective of predicting the turbulent velocity flow fields seen at the EMEC tidal energy site. As chapter 2 presented the basic concepts relating to turbulent channels and their computational modelling, it is now time to present their application to the present work.

This chapter will not only explain and justify the decisions taken when developing the simulation but cover the due diligence ensuring its accuracy by verification and validation. Verification of the spatial mesh discretization, temporal discretization and general quality evaluation of the LES model are included in the following sections with relevant discussion. Validation will compare actual data from the test site measurements with simulations to quantify any discrepancies between the two. The validation process is explained in this chapter and extended into the next chapter as well as part of the discussion of the output of the model.

This chapter begins with an overview of the LES WALE model within the Star-CCM+ multiphysics software. This is a continuation on the discussion of subgrid models from chapter 2 and the additional numerical models (SEM) coupled with

the main solvers. Following a short explanation of the application of the previously seen Navier-Stokes equations into a computational finite volume method package. The rest of the chapter will deal with the specifics of simulation description.

4.2 Numerical Model

Chapter 2 introduced the equations the principles and general theory behind turbulence modelling, describing the advantages and disadvantages of different models . After the review on the different models it was clear that the aims of the work required a model which fit within a computationally affordable scope, while pushing into a model sophistication range capable of high resolution turbulence modelling. Thus, the numerical model chosen was chosen to be within the LES family of models paying particular attention to wall effects.

The simulation was run utilizing a Large Eddy Simulation (LES) with a Wall Adaptive Local-Eddy Viscosity (WALE) sub grid scale model on the commercial software Star-CCM+ (Siemens, 2018). Turbulence was generated at the inlet of the model domain utilizing the Synthetic Eddy Method (SEM) (Jarrin et al., 2006) based on site depth profiles of turbulence Reynolds stress,turbulence intensity and integral length scales. Both the LES technique and SEM method will be explained in this section. The filtered continuity and Navier-Stokes momentum equations for an incompressible Newtonian fluid are, respectively

$$\frac{\partial \widetilde{u_i}}{\partial x_i} = 0 \tag{4.1}$$

$$\frac{1}{\rho}\frac{\partial \widetilde{u_i}}{\partial t} + \frac{1}{\rho}\frac{\partial \widetilde{u_i}\widetilde{u_j}}{\partial x_j} = -\frac{\partial \widetilde{p}}{\partial x_i} - \frac{\partial \tau_{\mathbf{ij}}}{\partial x_j} + \frac{\partial 2\nu\widetilde{\mathbf{S_{ij}}}}{\partial x_j} \tag{4.2}$$

where, the filtered variables for velocity and pressure are $\widetilde{u_i}$ and $\widetilde{p}$, $\tau_{\mathbf{ij}}$ is the subgrid stress tensor, ν is the kinematic viscosity, and $\widetilde{\mathbf{S_{ij}}}$ is the filtered strain rate tensor expressed by $\widetilde{\mathbf{S_{ij}}} = \frac{1}{2}(\frac{\partial \tilde{u_i}}{\partial x_j} + \frac{\partial \tilde{u_j}}{\partial x_i})$. Notation continues using the sub-indice in $\widetilde{u_i}$ to indicate direction of the domain, where i, j, k are the streamwise, spanwise and

vertical directions respectively. The subgrid scale (SGS) stress tensor $\tau_{\mathbf{ij}}$ is specified as

$$\tau_{\mathbf{ij}} = \widetilde{u_i u_j} - \widetilde{u}_i \widetilde{u}_j = -2\mu_t \widetilde{\mathbf{S_{ij}}} \tag{4.3}$$

For the current simulations in Star-CCM+; the WALE sub-grid model was utilized (Nicoud and Ducros, 1999). The model defines the eddy viscosity (μ_t) as shown in Eq.(4.4).

$$\mu_t = \rho \Delta^2 \widetilde{\mathbf{S_w}} \tag{4.4}$$

The filter length is determined as $\Delta = C_w V^{\frac{1}{3}}$, where C_w is a model coefficient with a value of 0.544 and V is the local control volume. The SGS WALE model uses a tensor $\widetilde{\mathbf{S_w}}$ given in Eq.(4.5), that is based on the symmetrical part of the velocity gradient tensor in order to have a more precise scaling of the turbulent viscosity near the wall. The tensor $\widetilde{\mathbf{S_w}}$ is defined as:

$$\widetilde{\mathbf{S_w}} = \frac{(S_d : S_d)^{\frac{3}{2}}}{(S : S)^{\frac{5}{2}} + (S_d : S_d)^{\frac{5}{4}}} \tag{4.5}$$

Where S is the modulus of the strain rate tensor computed from the resolved velocity field and $\mathbf{S_d}$ is a model tensor defined by an isotropical assumption of the strain rate. The equation for $\mathbf{S_d}$ has been simplified by using the abbreviation $\overline{g_{kk}} = \frac{\partial \overline{u_i}}{\partial \overline{x_j}}$

$$\mathbf{S_d} = \frac{1}{2}(\overline{g_{ij}}^2 + \overline{g_{ij}}^2) - \frac{1}{3}\delta_{ij}\overline{g_{kk}}^2 \tag{4.6}$$

The scaling of the wall will be of great importance when dealing with turbulence production near the sea bottom wall in comparison to other SGS models such as Smagorinsky-Lilly, where a specific tuning of the Smagorinsky coefficient would have the potential for greater error. A second order time advancing scheme was used for solving the temporal discretisation. Equations were discretised spatially by a rectilinear structure grid boundary-fitted grid.

4.3 Numerical Discretisation

The LES simulation was run using the Star-CCM+ commercial CFD finite volume method software package. The finite volume method (Versteeg and Malalasekera, 2007) solves the Navier Stokes equations in addition to any additional transport equations needed to be modelled by discretizing the differential equations for both space and time.

Equations are discretized by the general transport equation for any scalar variable ϕ. Equation 4.7 takes a scalar value $(\mathbf{u_i}, p)$ and discritises it for a volume cell V with a surface area A and a surface vector $\boldsymbol{a}$ across a surface flux S_ϕ. The transport equation sums up the volume integral of the temporal rate of change with the rate of change across each of the cell surface areas; these terms balance any diffusive terms across the surface areas proportional to a diffusion coefficient Γ and any source terms that might arise in the local cell volume.

$$\frac{d}{dt}\int_V \rho\phi dV + \int_A \rho u_i \phi d\boldsymbol{a} = \int_A \Gamma\nabla\phi d\boldsymbol{a} + \int_V S_\phi dV \tag{4.7}$$

Spatial discretisation is done by creating three-dimensional volume cells with a number of faces dependent on the type of volume cell. StarCCM+ uses a quadrature approximation to calculate face values on cells. Face value is calculated as the value at the center of the cell and calculated from:

$$\int_A \mathbf{J}^\phi d\mathbf{a} = \sum_f \mathbf{J}^\phi_\mathbf{f}\mathbf{a_f} \tag{4.8}$$

Thus the face area integral of convective or diffusive $\mathbf{J}^\phi$ fluxes are approximated as the sum of the same flux by the neighboring cell volume face cells $\mathbf{a_f}$. Cell volume integration approximates the value at the cell center. Temporal discretization is done by dividing a Δ_t time step into inner iterations. Cell gradients are calculated by the Hybrid Gauss-Least-squares method which uses Gauss' divergence theorem in equation 4.9, i.e.

$$\int_V \nabla\phi dV = \int_A \phi d\mathbf{a} \tag{4.9}$$

This theorem states that the gradient of a scalar variable in a volume is equal to the integral of the same variable across all of the face areas. Each face value is is the

average of adjacent cell values. The method itself is explained further in Siemens (2018); Issa (1985)

Differential mass, momentum and pressure conservation equations are solved by a segregated flow solver. Pressure and velocity fields are coupled by a predictor-corrector approach, in which velocity is predicted $\mathbf{u}^*$ after which the pressure field is corrected p'' to fulfil the continuity equation balance as a mass flux $\dot{m}_f$ for each cell face area. StarCCM+ uses the Pressure-Implicit with Splitting of Operators (PISO) algorithm (Shima et al., 2013) as a pressure-velocity segregated flow solver. The segregated solver goes through each one of its equations separately and iteratively matching each equation through pressure-correction equations as part of the PISO algorithm. The algorithm for the PISO is presented in Figure 4.1.

The segregated pressure and velocity solvers use the algebraic multigrid method (AMG) accelerated by a conjugate-gradient method. The general working principle of AMG is to solve cell volume equations by grouping cells into coarser subgroups. The resulting residual is used with finer subdivisions until reaching the actual mesh cell. This is done to eliminate higher frequency errors that come from fine mesh sizes such as the ones needed in LES simulations. Simulations were run on a flexible cycle that does not run the same grouping each iteration but will only group cells into finer and finer levels if residuals exceed a threshold. For more explanation on AMG solvers the reader is directed towards Raw (1995); Ferziger and Peric (2002)

Iterative solutions are solved carrying an error between each iteration (i), and this error is expressed as $\Delta\phi_p = \phi_p^{i+1} - \phi_p^i$. The residual r is calculated in equation 4.10, as the conjunction of errors for all neighboring cells $\Delta\phi_n$.

$$\frac{a_p}{f_r}\Delta\phi_p + \Sigma_n a_n \Delta\phi_n = r \tag{4.10}$$

Coefficients a_p and a_n relate directly to the discretization of the generic scalar transport equation and f_r is a user determined under-relaxation factor. The residual is a show of the convergence of the equation. In an ideal no-error situation the residual would reach 0, converging to a full balance of the equations with no numerical error. However, any numerical model will carry residuals no matter the quality,

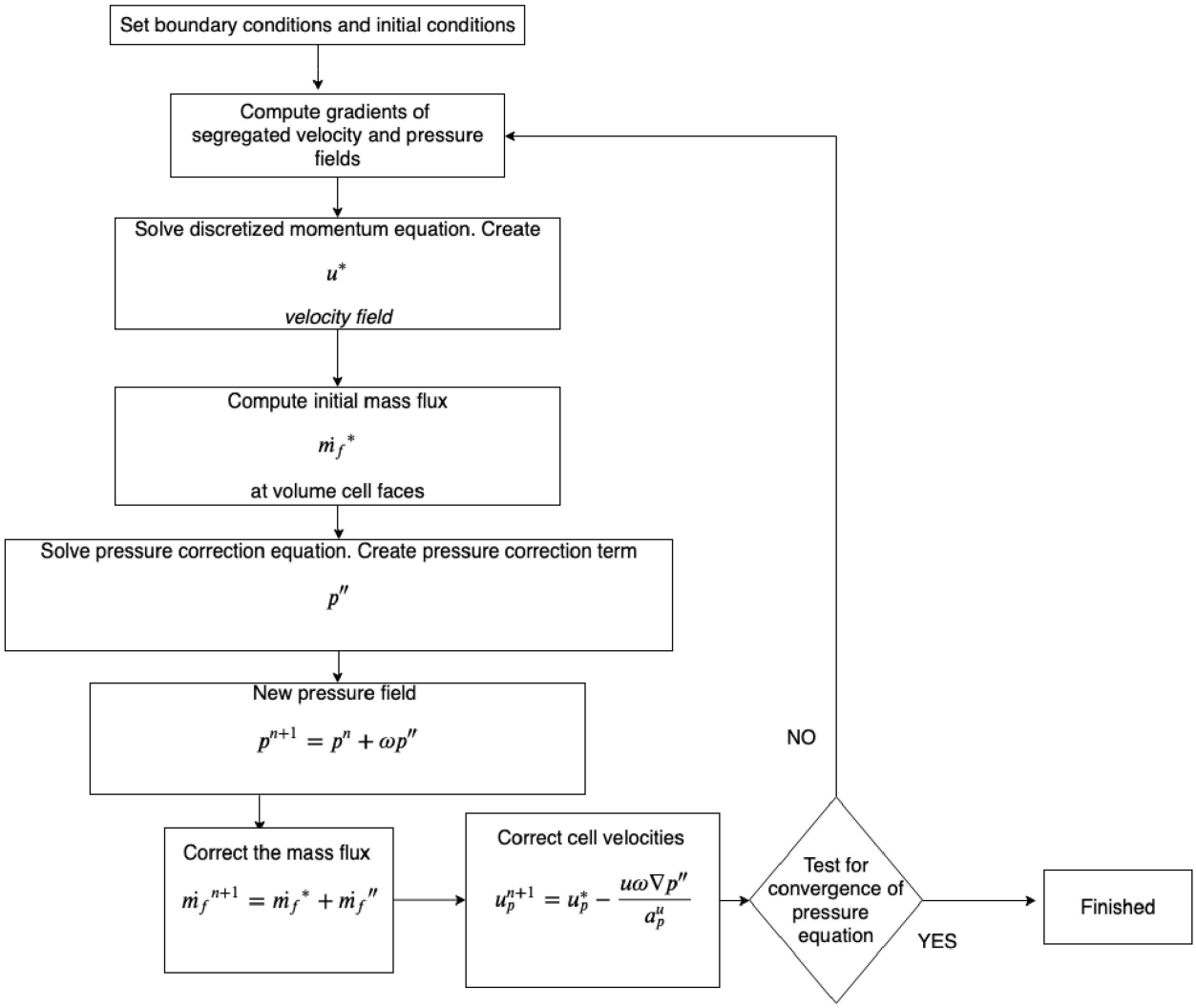

Figure 4.1: Pressure-Implicit with Splitting of Operators (PISO) Algorithm flowchart

resolution or solver method. A solution is considered coarsely converged when the residual r is $r < 10^{-4}$ for all equations, and values of $r < 10^{-5}$ for higher quality solutions. Unsteady simulations require iterations within each time-step changing the value of the residual. Due to this cyclical nature for each time step, convergence is checked for the final iteration of each time step and not for each iteration of the time step.

4.4 Synthetic Eddy Method

The realistic turbulent site inflow required additional methods to best generate a modeled turbulent signal in the domain. These turbulent signals are generated using the Synthetic Eddy Method (SEM) as formulated by Jarrin et al. (2006). Star-CCM+ generates the SEM signal from the Reynolds stress tensor or if the tensor is unknown, an isotropic turbulence intensity value is used. The SEM method helps create unsteadiness from the beginning of the inlet and as an initial condition producing randomized velocity injections based on turbulence parameters.

Figure 4.2 shows the total five depth profiles injected into the velocity inlet boundary condition of the domain, and these depth profiles were also used to initialize the simulation. The y-axis of the profiles are non-dimensionalized by dividing the vertical position by the local maximum depth. This gives 0 at the highest point of the water column and -1 for the sea bed location.

The SEM generates a fluctuating velocity signal (u_i) based on a eddy turbulent length scale (σ_k) seen in Eq.(4.11) composed of a steady averaged component $\overline{u_i}$ and a fluctuating convective component u_i'.

$$u_i(\mathbf{x}, t) = \overline{u_i}(\mathbf{x}, t) + a_{ij} u_i'(\mathbf{x}, t) \tag{4.11}$$

The convective fluctuating component is formulated by the a_{ij} factors, which are obtained from a Cholesky decomposition of the Reynolds Stress tensor $\mathbf{R_{ij}}$.

$$u_i'(\mathbf{x}, t) = \frac{1}{\sqrt{N}} \sum_{k=1}^{N} \epsilon_{i,k} f_k(\sigma_k, \mathbf{x}, t) \tag{4.12}$$

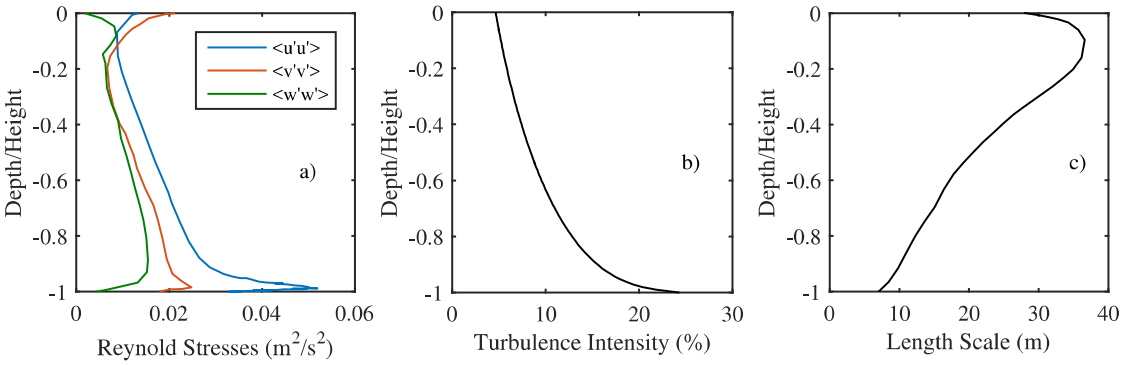

Figure 4.2: Inlet depth profiles for Synthetic Eddy Method: a) Reynolds Stress diagonal components (Case1 input), b) Turbulence Intensity Profile (Case 2 input), c) Integral Length Scale (Case 1 & 2).

This generates a velocity signal with a length scale σ_k, spin $\epsilon_{k,i}$ as well as a position x_k for each randomized eddy generated by the SEM. $\epsilon_{k,i}$ is a unit value with a positive or negative rotation direction for the eddy and f_k is a tent function to influence the position x by the eddy generated from the signal.

$$\mathbf{R_{ii}} = I^2U^2 \tag{4.13}$$

Assuming an isotropic turbulence intensity input the relations are made to the diagonal components $\mathbf{R_{ii}}$ of a generalized Reynolds tensor $\mathbf{R_{ij}}$ from Eq.(4.12) where $I = \frac{u_{rms}}{U}$ is the turbulent intensity and U represents the average over the inflow of the mean velocity profile.

SEM requires a set of velocity and Reynolds stress profiles along the water column to create the turbulent signal. As a complete set of Reynolds stress components was unavailable from site measurements two different cases were run based on either a) the diagonal components of the Reynolds stress and turbulence intensity (Case 1) or b) the tensor length scale (L) and turbulence intensity (Case 2).

Case 2 was run using the turbulence intensity profile extracted from site data during a 2.1 m/s inflow velocity of a flood tide averaged period. Site measurements did not have data points for the first 3 meters from the sea bottom, and in this case

the profile was modified using idealized turbulence intensity profiles. Length scale profiles as well as Reynolds stresses were obtained from a pre-run of a flat channel at low resolution taken at the midpoint of the domain in accordance with similar modelling attempts (Ahmed et al., 2015). It was expected that the flow geometry in the domain would improve the shape and magnitude of these profiles for both Case 1 (Reynolds Stress Profiles) as well as Case 2 (Turbulence Intensity profile). The comparison of both cases will help to compare the development of anisotropic turbulence across the domain when starting from an isotropic starting point or when injecting anisotropy straight from the inlet.

4.5 Spatial Discretisation

The selected bathymetry represents an area of the Fall of Warness, Scotland, in the vicinity of the EMEC test site located on the straight line between the two islands of Eday and Muckle Green Holm. Measurements of tidal elevation, tidal current velocity profiles and turbulence parameters have been processed and reported by Sellar et al. (2018). The large amount of data specific to tidal turbines allows for great support when comparing to numerical experiments. Developments and available test data make the site a prime candidate to analyze turbulent tidal characteristics for tidal extraction device applications.

Bathymetry data was available from the UK Hydrographic Office (https://data.admiralty.co.uk) from the Sanday Sound to Westray Firth Survey, at a resolution of 1 m. Data was then re-sampled for a smaller area at the EMEC test site. Bathymetrical constriction in the flow direction suggests a ramp up effect during flood tides or a slowing down during ebb, with other bathymetrical effects due to the proximity of shallow areas near the test site. Larger eddies originating from the nearby island and coastline may play a part in averaged velocity and turbulence depth profiles, but are not part of the scope of this simulation due to computational constraints. However, data from the nearby eddies is taken into account indirectly by the injected turbulence profiles obtained from the site data.

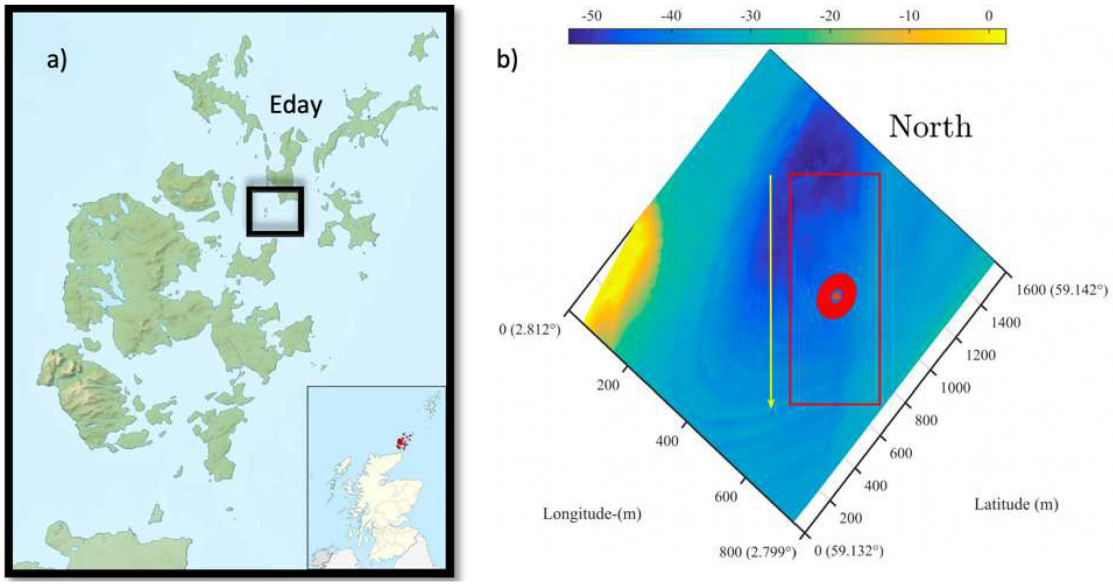

Figure 4.3: a) Location of the Fall of Warness in the Orkney Islands b) Bathymetry Map of the Fall of Warness EMEC site colored by depth. Red Rectangle indicates the sampled numerical domain aligned to the flow direction (320) during a flood tide indicated by the yellow arrow. Central circle and elipses correspond to the location of the installed turbine and Acoustic Doppler Current Profilers

Figure 4.3 b) shows the final domain selected from the area around the EMEC site, aligned towards the direction of the flow. Due to the restraints on computational resources there was a limit placed on the range of the area being modelled. The spanwise length was decided upon by having the ratio between the spanwise and the vertical direction (y/z) be $5 < y/z < 8$ to avoid any major influence from lateral boundary conditions. Due to the average depth being approximately 40 m (minimum depth is around 31 m, while the maximum depth is around 52 m) this gave possible spanwise lengths of 200 to 320 m. For greater coverage area the upper bound (320 m) was selected, with the turbine location assumed being selected as the centre point of the span. The size of the domain was limited by available computational resources: effective LES required a mesh resolution of at least 1-2 m. Simulations in previous LES tidal channel simulations with SEM by Creech et al. (2017) and preliminary simulations have shown a start-up length of approximately 250 m is required, thus giving an effective domain 1 km long in the streamwise direction. This startup length allows the flow to be developed by the boundary conditions of the domain and not solely by the injected profiles at the inlet. Figure 4.4 shows a more complete visualization of the domain, the cross-sectional area velocity contours demonstrate, at a first glance, the capabilities of LES with the SEM to simulate a full 3D flow, as well as the chaotic velocity field at the inlet and its development at different cross-sectional areas as the domain develops. SEM initialized the flow with 300 randomized coherent structures throughout the domain.

4.5.1 Boundary Conditions

Boundary conditions force the simulation to change according to the physical limitations of the case. Cell volumes at the boundary conditions have certain conditions imposed on them for any variable. Boundary condition forcing is usually done through acting upon the variable itself on the face (Dirichlet condition) or on the gradient value (Neumann condition). Boundary conditions used in the simulation will be introduced shortly, before mentioning how they were applied to the resampled domain of the Fall of Warness.

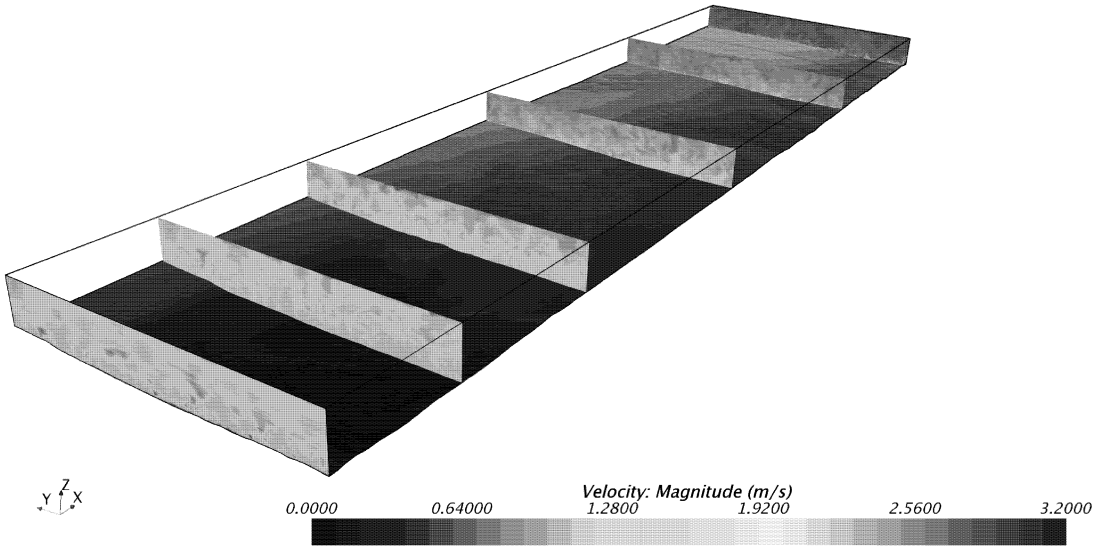

Figure 4.4: 3D visualization of the domain, selected cross-sectional areas are shown to best show the accelerating flow with the streamwise direction. Seabed is colored by depth for an appreciation of bathymetrical change. Flow direction follows the x direction from left to right.

- Inlet: Defines the mass flow injected into the domain. The SEM employs a Dirichlet condition specified by the user to create a coherent random velocity field that shoes the turbulent values specified as well.

- Outlet: The direction of the outgoing velocity field can be set to extrapolated for higher solution convergence and stability instead of the normally utilized normal to outlet wall direction. The main objective of the boundary condition is to apply a pressure gradient ∂p to a static pressure of 0, following the conditions of a Neumann condition.

- Walls: Walls may be no-slip or slip. Wall boundary conditions will be changed when applying wall models as seen in Chapter 1. It is necessary for the wall to have no mass flux creating an impenetrable lid.

- Symmetry planes: Symmetry planes are used to avoid interference from wall limiting the domain, In the case of tidal channel flow it is convenient to apply

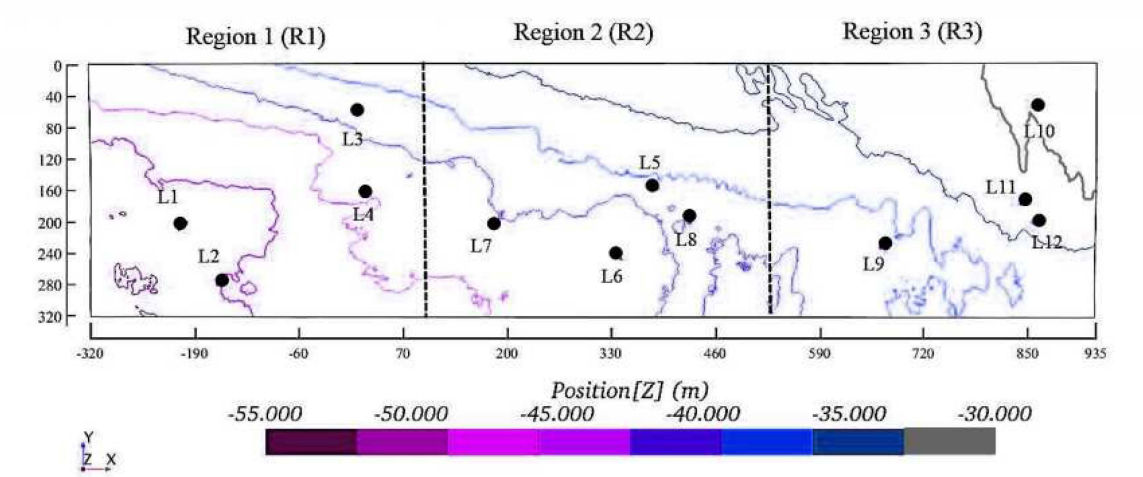

Figure 4.5: Aerial view of the Domain showing contour lines colored for depth. All probe lines are shown as well as the delimitation for their respective regions. Location of probe lines can be best seen in Tables 4.5.1

symmetry planes when the domain is large enough. Both the pressure and wall normal velocity is set to zero, avoiding any reflective effects.

Figure 4.5 shows an streamwise-spanwise upper view of the domain with bathymetry contour lines to visually show how the domain depth decreases as the streamwise direction progresses as well as the extent of the domain in absolute terms. The location of the line probes from which data was sampled is shown in table 4.5.1 for reference.

Streamwise normal surfaces were set as a velocity inlet at x=-320 m and a pressure outlet at x=935 m with an extrapolated backflow. The velocity inlet was set to a power law as seen in Eq.(4.14), with a α=7. in order to have an inflow closer to the site measurements as per the observations at the site :

$$u(z) = u_{ref}\left(\frac{z}{h_{ref}}\right)^{\frac{1}{\alpha}} \tag{4.14}$$

where, u_{ref} was the reference velocity taken at turbine hub height h_{ref} reference. The difference in the size of the cross sectional areas perpendicular to the streamwise direction, due to variable depth, leads to a ramp up of the velocity in shallow regions.

Table 4.1: Line Probe Coordinates

	X (m)	Y (m)	Max Depth (m)	Region
L1	-200	204	50	R1
L2	-150	285	47.8	R1
L3	18	61	41.3	R1
L4	30	169	44.4	R1
L5	385	161	40.5	R2
L6	341	247	43.5	R2
L7	185	204	43	R2
L8	425	204	42	R2
L9	664	235	41.5	R3
L10	850	55	34.1	R3
L11	834	175	33	R3
L12	850	204	35.6	R3

For this reason the velocity at the inlet will only be a fraction of the velocity at the location of the turbine.

The inlet velocity was set to 1.7 m/s. This equated to a speed of 2.1 m/s at the turbine location, due to the cross-sectional area ratio at the inlet and at site location, which means comparisons could be made to the EMEC site measurements for 2.1 m/s flood tide data.

Spanwise lateral boundary conditions were set to symmetrical planes. Top boundary of the domain was set to a slip wall as per the closed lid method for open channel flow. The lower boundary condition, corresponding to the bathymetry of the channel was set as a no-slip wall with a logarithmic wall function. The classic cases for turbulent channel flow have used periodic boundary conditions in the span and streamwise directions such as (Fröhlich et al. (2005b),Moin and Kim (1982) & Davidson and Dahlström (2005)). A visual summary of the boundary conditions of

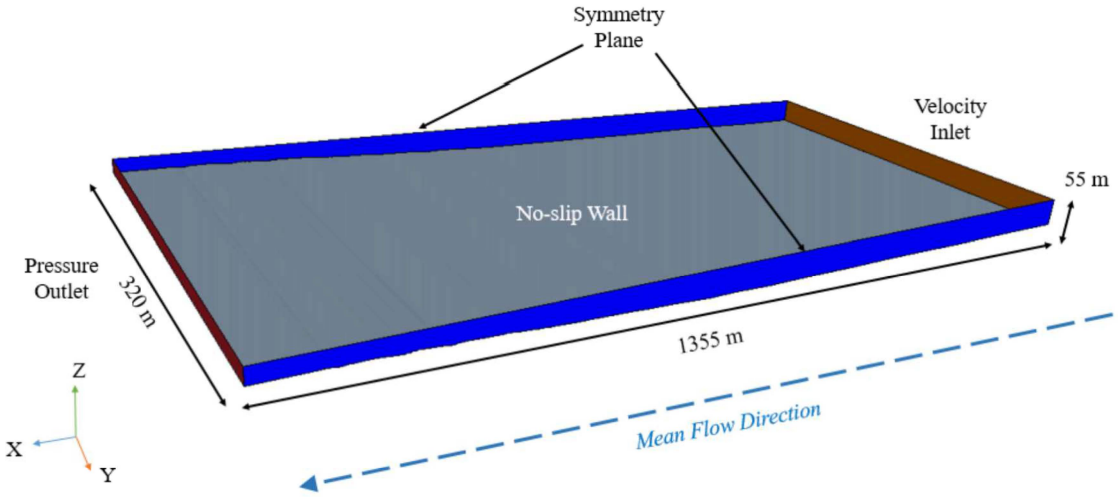

Figure 4.6: Boundary Conditions of the sampled domain

the domain can be seen in figure 4.6.

4.5.2 Mesh Construction

Spatial discretization quality was tested for 3 different mesh resolutions (denoted as M1, M2 and M3). Each resolution was attempted as a trial run at an increasing level of grid spacing refinement with M1 being the coarsest and M3 the finest. The three mesh resolutions used a relation $\Delta_x = \Delta_y = 2\Delta_z$ for the majority of the water column. The coarsest mesh resolution trial simulation used a $\Delta_{x_1} = 3$ m, followed by a finer mesh resolution Δ_{x_2}=2.1 m and the finest grid resolution being equal to Δ_{x3}=1.5 m (see table4.2 for more details of each mesh and its parameters). Figures 4.7 shows a cut of the cross section of the mesh at the span midpoint to help visualize the finest mesh resolution used for the entire depth, while figure 4.8 shows a zoom of figure 4.7 to emphasize the the bottom inflation layer.

A wall resolved simulation was not feasible for a Reynolds number (Re) of such a magnitude (10^7) due to the complexities of meshing the flow near to the sea floor limited by the computational resources available. Choi and Moin (2012) estimate a wall resolved number of necessary cells at $Re^{13/7}$, while a wall modeled LES at a lesser approximation was calculated at approximately Re. Thus wall functions

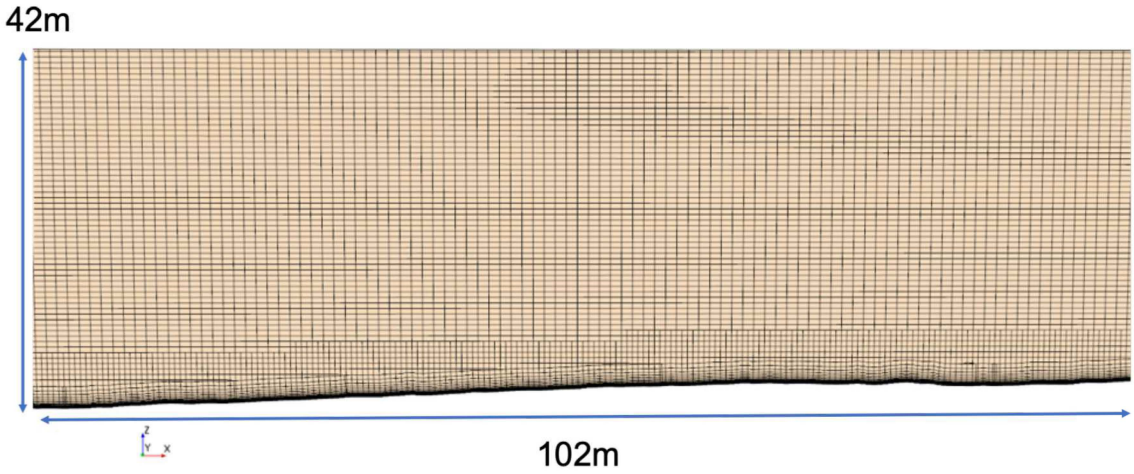

Figure 4.7: Cross-sectional view of mesh at midpoint of the span direction of the domain.

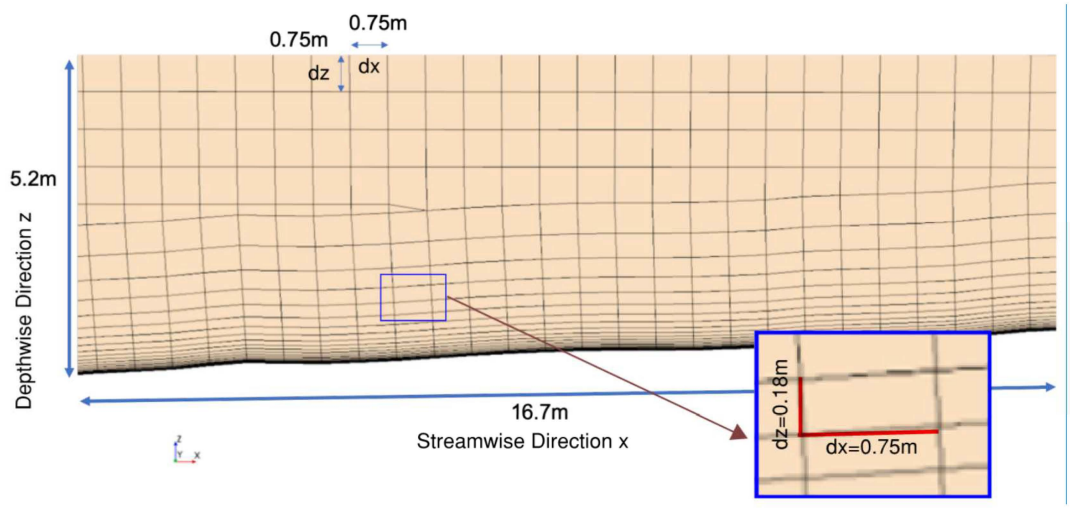

Figure 4.8: Magnified view of mesh showing inflation layers near the bed

were introduced as part of the LES model, instead of resolving down to the viscous sublayer as in traditional LES. The simulation follows the wall modeled LES methodology used by Bechmann et al. (2010) and is covered extensively in a review by Bose and Park (2018).

All mesh resolution cases were meshed in such a way that the first cell above the wall averaged $\overline{z^+} = 30$ throughout the domain, thus capturing the majority of the log layer. The finest mesh used 24 prism cells for the first $3m$ near the wall, each subsequent layer had a geometric progression of 1.2. The final mesh contained a value of N_x x N_y x N_z= 1204 x 305 x 76 for a domain size of $32.2H$ x $7.8H$ x H where H is the averaged depth of the domain. Figure 4.7 shows a streamwise-vertical cross section of the domain to visualize the size and distribution of the volume cells. A zoomed in image can be seen in figure 4.8 to understand the geometric progression of the prism cells in the first 3 m near the wall. Inflation was chosen as a combination of having the greatest possible resolution in the first 10% of the smallest depth which is where initial simulations showed the greatest turbulent effects, as well as being computationally affordable and within mesh correct practices of inflation rate and size of the first cell near the wall. Appendix A shows the validation of a flat channel case using the same parameters against canonic

Convergence of the mesh resolution was studied to eliminate the spatial discretization mesh error as much as possible, within the computational resources available. Figures 4.9 and 4.10 show time averaged depth profiles for streamwise velocity u_i and turbulent kinetic energy k from all three meshes at $x = 425m$, $y = 160m$. Differences between all three meshes were negligible for velocity and TKE. Grid convergence indices were calculated using the 2-norm (*aka* Euclidean norm) $||\mathbf{x}|| = \sqrt{x_1^2 + x_2^2 + ...}$ of each depth profile, as per Creech et al. (2017), for the aforementioned values. The Grid Convergence Index (GCI) was developed by Roache (1998) as measure of the error stemming from mesh size.

$$GCI = \frac{SF}{(r^{np} - 1)} \left| \frac{f_1 - f_2}{f_1} \right| \tag{4.15}$$

Where refinement ratio r is the ratio between the Δ_x for each mesh. Ratios between

meshes had a $r_{12} = 1.4$ and $r_{23} = 1.42$, where the subscript indicates the meshes being compared. The safety factor SF is recommended by Roache (1998) to be set to 1.25 when comparing more than 2 grids to ensure a conservative convergence comparison between grids. The second term in equation 4.15 compares a specific value f_1 and f_2 computed for each mesh to gather a measure of error. Order of convergence np is a local value and always lower than the theoretical order of the entire simulation, it is defined as:

$$np = \frac{1}{\ln(\mathrm{r})} \ln\left(\frac{(f_3 - f_2)}{f_2 - f_1)}\right) \tag{4.16}$$

The GCI calculated for the finest grid was equal to 0.166% when analyzing the streamwise velocity and 6.67% for the turbulent kinetic energy, however the latter is not a clear error due to the influence of the sub-grid contribution changing the value simultaneously with the spatial error. Both values were calculated to be within the asymptotic range and thus sufficiently refined. Convergence is also studied through depth profile comparison of averaged streamwise velocities (Figure 4.9) and turbulent kinetic energy k (Figure 4.10) of all three meshes. Both figures averaged data from mid-domain along the water column from all previously mentioned meshes. Averaged velocity depth profiles showed little to no discrepancy between meshes. Turbulent kinetic energy depth profiles were a better comparison for the convergence of turbulent parameter grid values. While the majority of the watercolumn ($Depth/H = -0.96$) held within a 5% difference between meshes, peak values near the seabed were conditioned to the filtered meshing of LES models. The higher the resolution of the mesh the higher the near bed cell k values. Higher resolution of the peak bulge near the seabed also helps for a smoother transition to the rest of the watercolumn.

Values such as the GCI is a powerful tool to study the quality of meshes, however due to the filtered nature of LES simulations, mesh quality must be ascertained through other methods and values that connect the mesh resolution with the modeled and resolved portions of the turbulent energy spectrum. Figure 4.11 shows a energy spectra plot calculated for the mid-column point streamwise velocity u_i. The

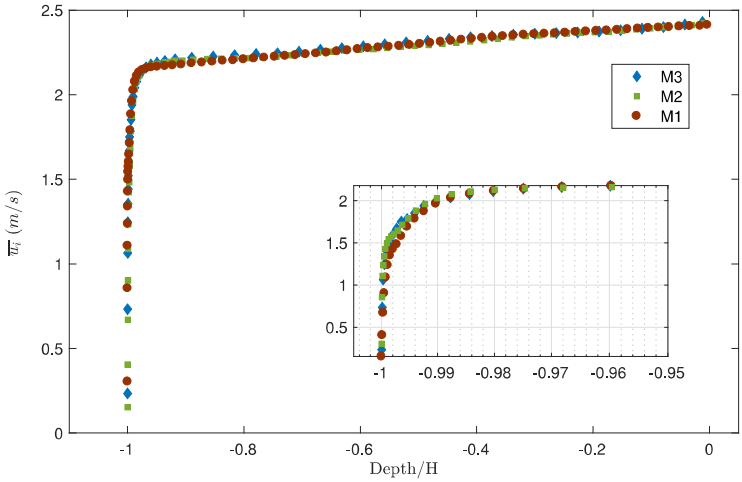

Figure 4.9: Time averaged streamwise velocity u_i Depth Profile Mesh Convergence Comparison with zoomed in view of near sea bed values.

drop off after the filter frequency is clear in each of the spectra, fluctuations begin to smooth out drastically compared to lower frequencies. All meshes filter frequencies are within the inertial subrange, yet even in a visual manner it is clear that M3 is much too coarse for any serious engineering purpose, as it fails to appropriately capture the energy content of some lower frequency content.

4.6 Temporal Discretisation

Time discretisation is based on a second order scheme where the average Courant-Friedrichs-Lewy number (CFL) was 0.5, however local quality throughout the domain can be seen in Figure 4.12 a) for 4 representative line probes throughout the domain. The zoomed in box within the figure shows the height at the inflation layer with a logarithmic y-axis for clarity. Values had a $CFL \sim 0.3$ for the bulk of the flow, as recommended for wall modelled LES by Kornhaas et al. (2008), only reaching higher values for the wall modelled area near the seabed due to the computational expense of resolving it completely. The set time step Δt at the finest resolution mesh was set to 0.2 s ($t^* = 0.0106$), where $t^* = \frac{t}{H/U}$ is non-dimensionalized by the mean velocity U and characteristic length which is established as the depth H.

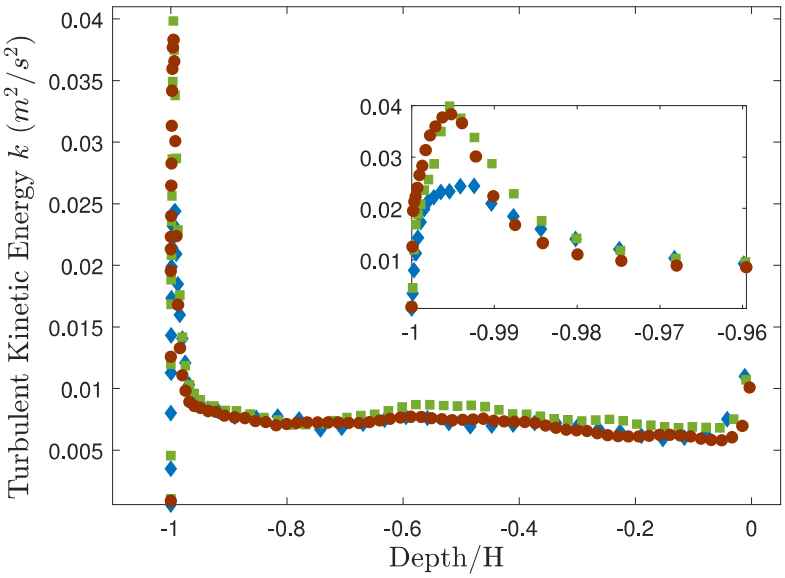

Figure 4.10: Turbulent Kinetic Energy k Depth Profile Mesh Convergence Comparison with zoomed in view of near sea bed values. Symbols are as in figure 4.9.

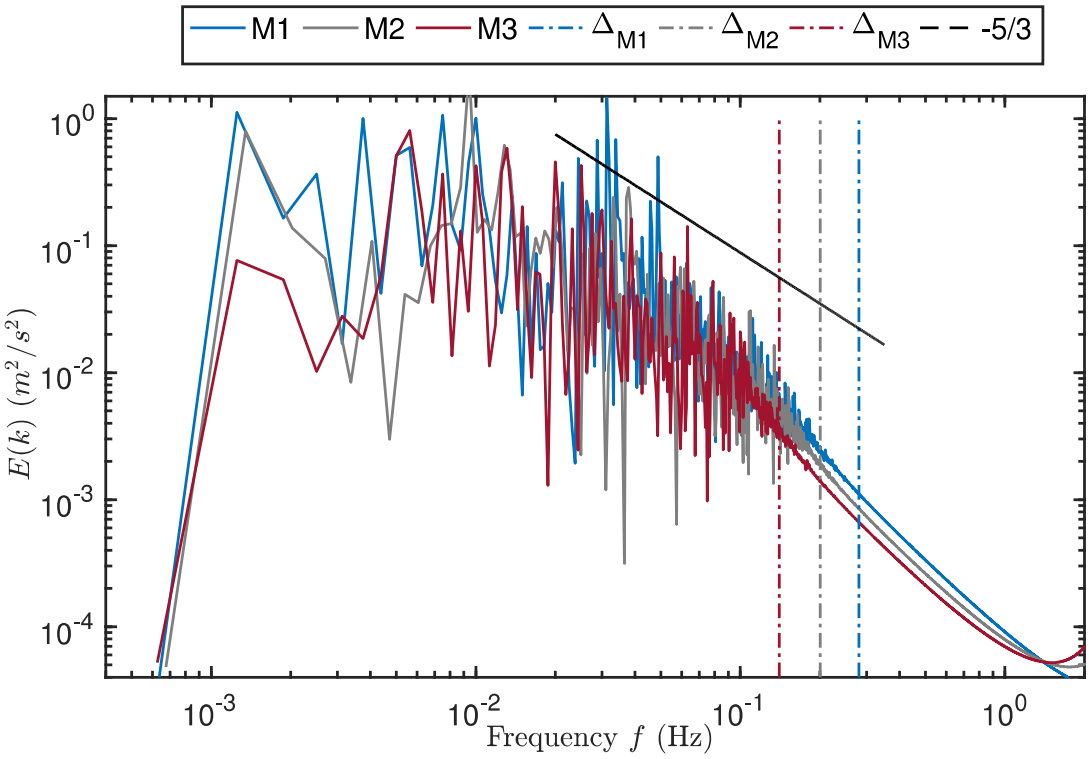

Figure 4.11: Turbulent Kinetic Energy k Depth Profile Mesh Convergence Comparison with zoomed in view of near sea bed values. Symbols are as in figure 4.9.

The simulation was run and sampled for a total of 30 minutes ($t^* = 95.77$), after an initial start-up time of 20 minutes ($t^* = 63.78$); this gave a total number of samples $Ns = 9000$ and a sampling frequency of 5 Hz. Sampling was run for enough time and samples for statistical convergence of scalar vectors throughout their $1^{st} - 4^{th}$ statistical moments(mean, standard deviation, skewness and kurtosis). Here statistical moments are defined as

$$m_n = \int_{\infty}^{\infty} x^n dF(x) \tag{4.17}$$

where n is the order of the moment, x is the scalar value being analyzed that follows a cumulative probability distribution function $F(x)$. The second moment is formally defined as the variance m_2, but is replaced by the standard deviation $\sigma = \sqrt{m_2})$ to relate it better to turbulence parameters I and $\mathbf{R_{ii}}$.

Statistical convergence confirms the sufficient number of samples so that any additional samples would have a negligible change when calculating the statistical moment. For this a sliding window is useful to compare changing behavior of the sampled value as more samples are taken into statistical calculation. Each statistical moment sliding window was non-dimensionalized by the following equation:

$$N^{th}Moment^*_{Ns} = \frac{N^{th}Moment_{Ns} - N^{th}Moment_{i=1:Ns}}{N^{th}Moment_{Ns}} \tag{4.18}$$

Four points ($P1 - P4$) were selected at $x = -635m$, $y = 160m$ and $z_{1-4} = -20, -22.5, -25, -27.5\ m$. Each point streamwise velocity time history was subjected to equation 4.18 sliding window equation to quantify the statistical convergence power and ensure sufficient sample time and number. Figure 4.13 shows the effect of increased sampling for all four normalized statistical moments as per equation 4.18. As the number of samples increases, the fluctuation between the calculated value of each statistical moment converges to 0. The number of samples required for this convergence is lower the order of the statistical moment. Statistical convergence was found to be .02%, .2%, 2% and 1% for the mean, standard deviation, skewness and kurtosis respectively after 9000 samples for all points. All fall under acceptable error levels and it was considered that any additional run time would not be necessary for the studies requirements.

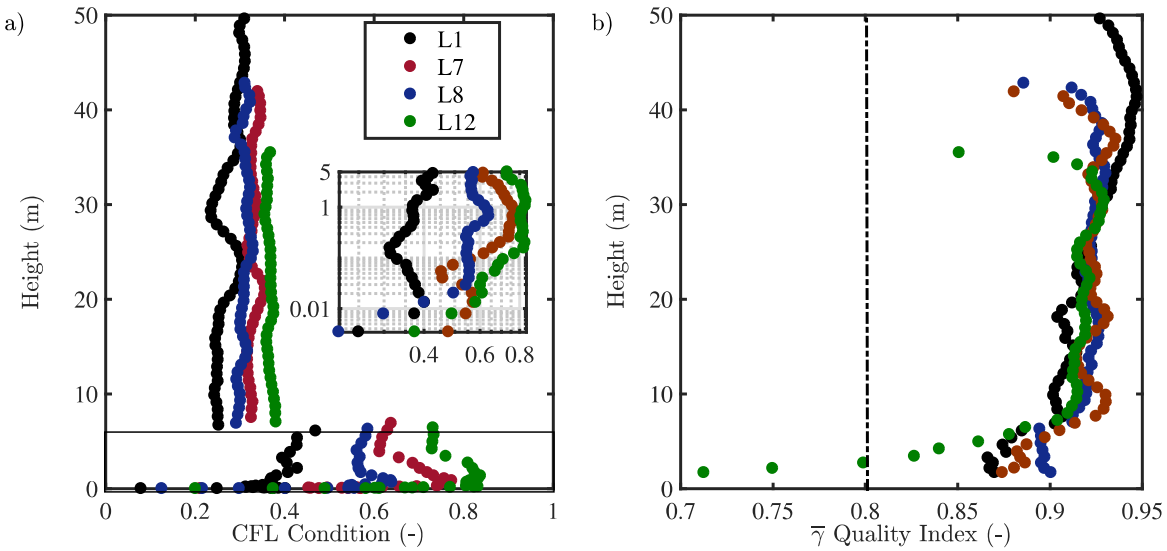

Figure 4.12: a) Depth Profiles of the Courant-Friedrichs-Lewy condition for a selected number of probes in different regions of the domain (L1,L7,L8,L12). See Table 4.2 for more details on probe location. b) Depth Profiles showing the local $\overline{\gamma}$ for the same line probes as in a) for all vertical control volumes above the inflation layer.

Table 4.2: Mesh Resolution Study

	# of Cells	Δ_x (m)	Δ_y (m)	Δ_z (m)	γ	2-Norm u_i	2-Norm k	Δ_t (s)
M1	3.7 M	3	3	1.5	0.443	14.4391	0.0861	0.333
M2	10.9 M	2.1	2.1	1.05	0.608	16.7154	0.1162	0.285
M3	30.1 M	1.5	1.5	0.75	0.924	16.9312	0.1276	0.200

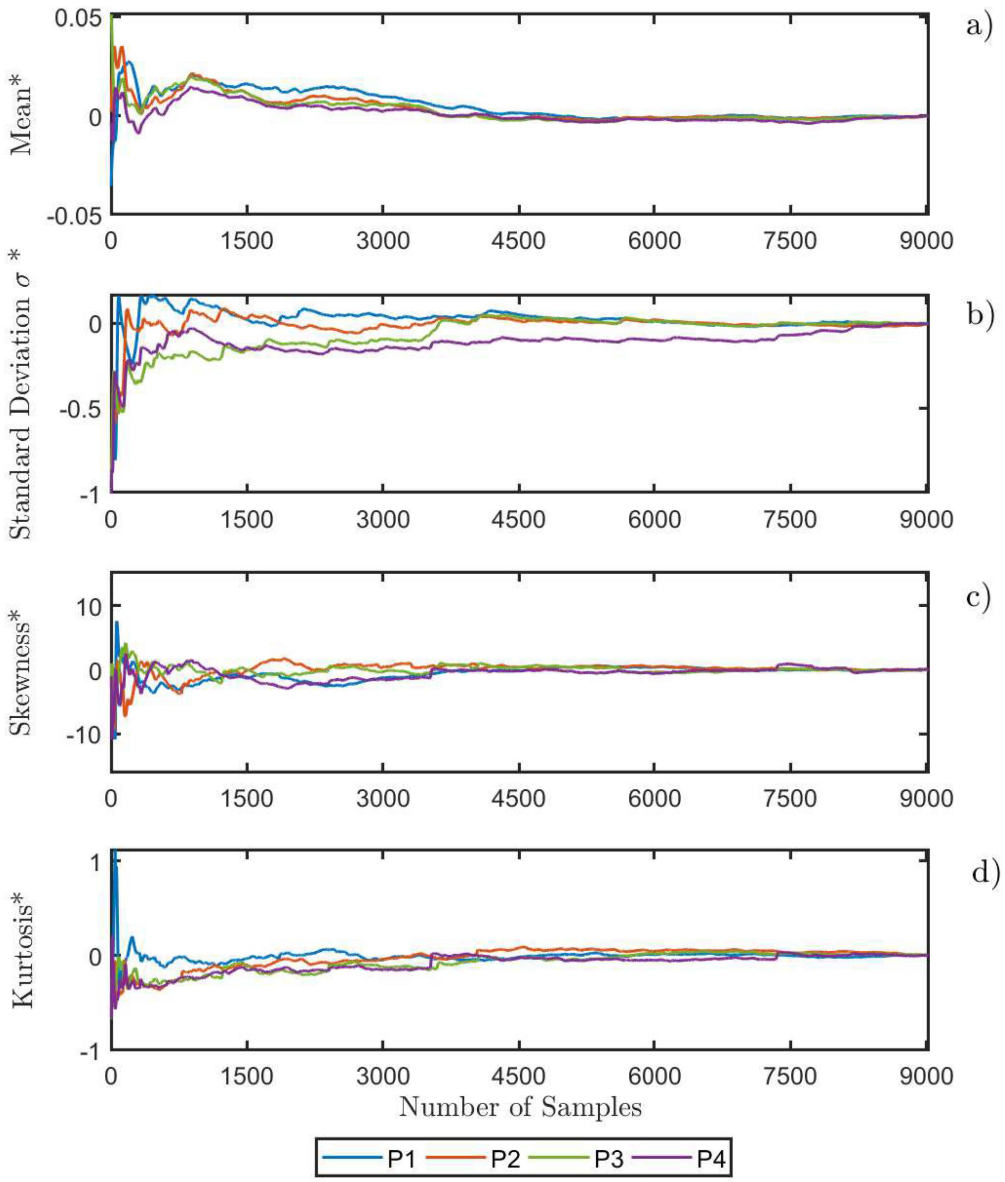

Figure 4.13: Statistical convergence of four N^{th} statistical moments of streamwise velocity u_i. a)Mean b)Standard deviation c)Skewness d)Kurtosis

4.7 Quality Indices

Quality of the simulation was indicated using the γ quality index as used by Pope (2004), which shows the amount of turbulent kinetic energy(TKE) being resolved, in relation to the total TKE. The total TKE is a sum of the subgrid and resolved TKE, as well as quality indicators suggested by Davidson (2009) regarding the resolution of the integral length scales measured in the number of cells per resolving eddy length scale.

In order to verify the quality of the simulation, several quality tests were done to assess the resolution of the mesh for an LES scale resolved model. The resolved TKE (κ_{res}) and subgrid scale TKE (κ_{SGS}) are calculated respectively by

$$\kappa_{res} = \overline{u_i' u_i'} \tag{4.19}$$

$$\kappa_{SGS} = C_t S \frac{\mu_t}{\rho} \tag{4.20}$$

Here C_t is a model coefficient which must be greater than $\sqrt{3}/2$ and set at 3.5 by the Star-CCM+ environment as a default. The ratio of the resolved TKE to the total TKE, γ, is then given as

$$\gamma = \frac{\kappa_{res}}{\kappa_{res} + \kappa_{SGS}} \tag{4.21}$$

This ratio was calculated over the whole domain, with the finest mesh resolution giving a mean value of $\overline{\gamma} = 0.924$ for M3, this is far above the recommended values for kinetic energy resolution set by Celik et al. (2009); Pope (2004) of 0.8-0.85. Both meshes M2 and M1 were under the recommended values showing a high subgrid scale contribution, especially for the coarsest grid. Local values of γ_{M3} for depth line probes at different locations in the domain can be seen in Figure 4.12 b). The figure shows how the quality increases from 0 in the modelled wall region to highly resolved ($\gamma > 0.8$) 3 m above the seabed at all locations.

Largest length scale resolution of the mesh was measured using the ratio of the number of grid points (Δ) that resolve the largest length scale ($\mathcal{L}$), as shown

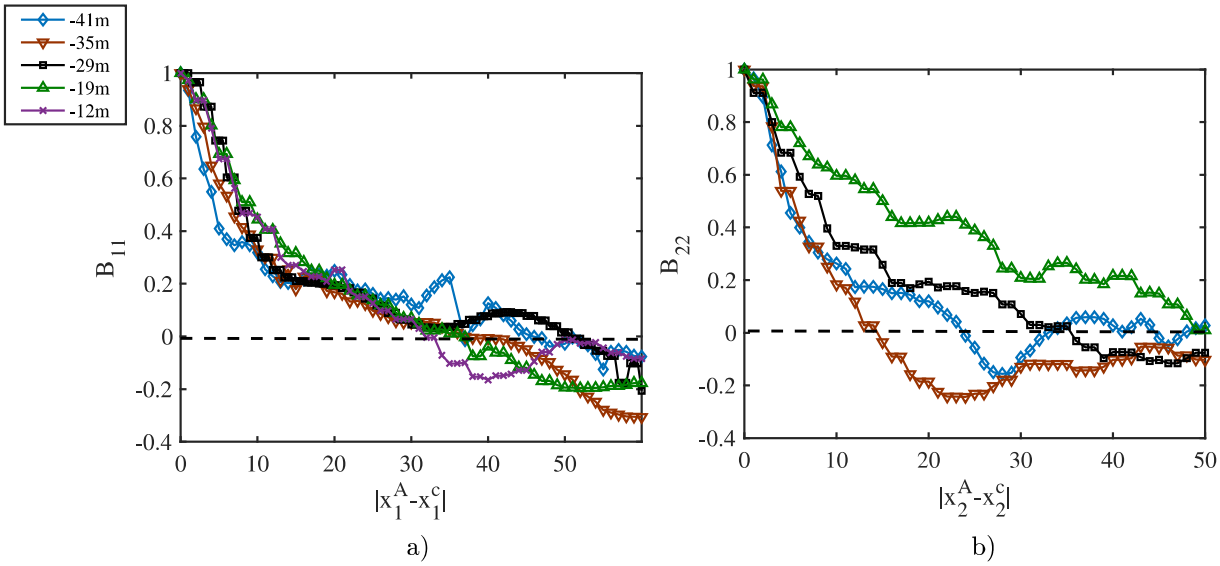

Figure 4.14: Two point correlation for a) streamwise and b) spanwise direction at 4 vertical depth locations as shown in the legend. Here B_{ii} is the correlation coefficient and x_i^A (m) is the point of interest and x_i^C (m) is the second point to where the correlation is measured. Each marker is taken at cell location.

in figure 4.14. Figure 4.14 shows two point correlations normalized by root mean square values u^2_{rms}, on the y axis, expressed as B_{11} in the streamwise direction and B_{22} for the spanwise direction, respectively. Each correlation is plotted against the distance between two points, one fixed $x_A(m)$ and the other increasingly away $x_C(m)$. Each plot posts 4 correlation functions taken at 4 vertical locations ($z = -41, -35, -28$ & -19 m) in order to show the changing resolution throughout the water column. The least resolved direction correlation (spanwise) B_{22} showed a minimum of $\mathcal{L}/\Delta = 16$. The ratio increases as the vertical location moved further away from the seabed.

The average of the cell/length scale ratio $\overline{\mathcal{L}/\Delta}$ was calculated for the 4 line probes taken throughout the domain. The ratio showed an average of 26 points for streamwise resolution for all cells above the inflation layer of the mesh. All line probes showed values of $\mathcal{L}/\Delta > 8$, as recommended as a baseline for the least resolved direction in coarse LES simulations (Davidson, 2009). The length scale resolution in conjunction with the calculations of resolved turbulent kinetic energy

give a strong measure of sufficiently high quality.

4.8 Summary

Each section in the chapter explained and discussed a different aspect of the numerical model, as well as the metrics necessary to grant the model a level of credibility and reliability. The analysis of the tidal energy site simulation results are only relevant when the mechanism, limitations and errors are known and measured. Large eddy simulations are of such a high complexity that each component of its design must be deconstructed and analyzed separately.

This section has shown the inner numerical models of the commercial package StarCCM+ as far as the documentation can show. The present body of work was helped greatly by understanding some of the inner workings of the CFD software. The simulation was of such an ambitious nature for the resources available that tuning and use of additional methods proved vital to running a quality simulation.

Results from the simulation described will be shown in the remaining chapters. It was important that any questions about the nature of the simulation be addressed, particularly with respect to the numerical verification and initial validation of the model. Both were shown here through a series of quality indices, indicators and standards of the literature. Future work may take this methodology and improve it using all of the details to reproduce the simulation and use it as a building block to develop upon.

CHAPTER 5

BATHYMETRY ROLE IN TURBULENT PRODUCTION OF A FLOOD TIDE

5.1 Introduction

A Wall Modelled Large Eddy Simulation is carried out of a sampled area of the Fall of Warness, Scotland, encompassing a tidal energy site, as introduced and verified in chapter 3. Simulated results shown in this chapter were validated with velocity, turbulent intensity and turbulent kinetic energy density site data from the European Marine Energy Centre, Orkney. In this chapter, results will show the influence of the sea bottom as a modifier of flow velocities and a driver of turbulence production at local areas important for the purposes of tidal converter performance and loading.

The aforementioned numerical model is carried out using high resolution bathymetry and site inflow related measurements for a 2.1 m/s steady flow flood tide. High order turbulence parameters such as: Reynolds stresses, length scales, frequency spectra and turbulence intensities are analysed at different depths and locations in the domain, to better understand their dependence on the changing bathymetry. Results will show the three-dimensionality of the flow field for time-averaged values as well

as instantaneous events. These outcomes will help establish the necessity of high resolution time-variating turbulence models over the traditional use of averaged RANS models. The present chapter aims to strengthen confidence in the method for developing high fidelity realistic numerical simulations at tidal energy device scale, by being capable of showing unsteady temporal and spatial turbulent characteristics of tidal flow. Turbulence characterization demonstrated will be fundamental to recreate and predict flow fields in offshore applications for renewable energy.

This chapter will begin with a comparison of the LES simulation, described in Chapter 3, and site data; in order to fully validate the model. A brief discussion will also be shown of the site data for full context of what the model results are being compared and their inherent processing characteristics.

5.2 Site Measurement Data

Data was supplied in both raw and processed formats from the ReDAPT project (http://redapt.eng.ed.ac.uk). The data was obtained from measurement campaigns during 2012 to 2014. Diverging-beam Acoustic Doppler Current Profilers (ADCP) were flow aligned 60-100 m in front and behind a tidal turbine, while a long-range Single Beam Acoustic Doppler Profiler (SB-ADP) was placed on top of the tidal turbine. The data from different instruments were recorded at varying sampling frequencies. Tidal current parameters (spanwise, streamwise and vertical component velocities, TKE, TI etc.) were calculated based on 5-minute length quality controled data samples. Further details of the measurement campaign may be found in Sellar et al. (2018).

The data presented as site measurement depth profiles for velocity, turbulence intensity and turbulent kinetic energy density are the result of post processed ensemble averaging of 5-minute period bin profiles from the ADCPs sampled at 0.5 Hz.

For the purposes of validation, the site measurement data used for the present study is an average of 1890 blocks of 5-minute data, corresponding to conditions of

$2.1 \pm 0.2\ m/s$ under insignificant wave height $H_{m0} < 0.8$ at flood tide.

It is mentioned by Sellar et al. (2018) that values are sensitive to post-processing methods, particularly noise filtering and detrending for turbulent intensity. Single point data is also presented from the ADP. Profiles are not available for the ADP, as the nature of the ADP is not as a current profiler, however it is mentioned by Sellar et al. (2018) as having higher reliability.

5.3 Site Measurement Data Validation

Velocity depth profiles extracted from depth aligned probes in the simulation, are analyzed to compare simulations with test site data for validation. Streamwise velocity, turbulence intensity, TKE density and frequency spectra will be shown comparing site data and simulation depth profiles. Site measurement data is gathered from a height range of 3-40 m due to the inaccuracies or inability of the sensors to capture ranges near surface of the water column and the seabed.

Table 5.1 shows the location details of the depth aligned line probes in the streamwise and spanwise directions within the computational domain, this table was previously seen in chapter 3 and is repeated here for clarity. These line probes were classified in terms of their position along the domain in the streamwise direction which correlated with their maximum depth. In order to distinguish the flow patterns at its related parameters, the whole computational domain has been divided into three regions, each 417 m long. In total 12 probes, 4 for each region have been selected for assessing the flow parameters. The details of probe locations within each region are listed in the tables.

Region 1 (R1) is dominated by the start-up region of the domain, where L1 and L2 were selected, with which one could be able to compare the developing behaviour of flow near to the inlet. However, L3 and L4 show developed behaviour, only differing in their spanwise positions and thus depth. Region 2 (R2) is the central region in the vicinity of the EMEC turbine location. All site measurement data is taken from points near this region. Lines 5-8 were selected to have a view of

Table 5.1: Line Probe Coordinates

	X (m)	Y (m)	Max Depth (m)	Region
L1	-200	204	50	R1
L2	-150	285	47.8	R1
L3	18	61	41.3	R1
L4	30	169	44.4	R1
L5	385	161	40.5	R2
L6	341	247	43.5	R2
L7	185	204	43	R2
L8	425	204	42	R2
L9	664	235	41.5	R3
L10	850	55	34.1	R3
L11	834	175	33	R3
L12	850	204	35.6	R3

spanwise and streamwise variation. Finally, region 3 (R3) shows the region closest to the pressure outlet where depth is at the shallowest point, lines 9-12 were selected in similar fashion to region R2 to see the variation in the region for both streamwise and spanwise directions. Figure 4.5 shows a graphic visualization of the location of each probe and the extent of each region.

Figure 5.1 a) shows comparisons between simulation Case 2 data at the midpoint of the domain, the EMEC site data at flood tide for a 2.1 m/s at hub height velocity as well as a theoretical boundary layer profile fitted for a Reynolds number of 10^7. The agreement between the theoretical power law for boundary layers and test site data suggests a boundary layer velocity profile, agreeing well with the analysis done by Sellar et al. (2018), where a 1/7 power law was fitted to the site data for flood tides with no wave conditions. Several trial cases were attempted with different SEM velocity profiles injected at the inlet besides Cases 1 and 2, with all developing

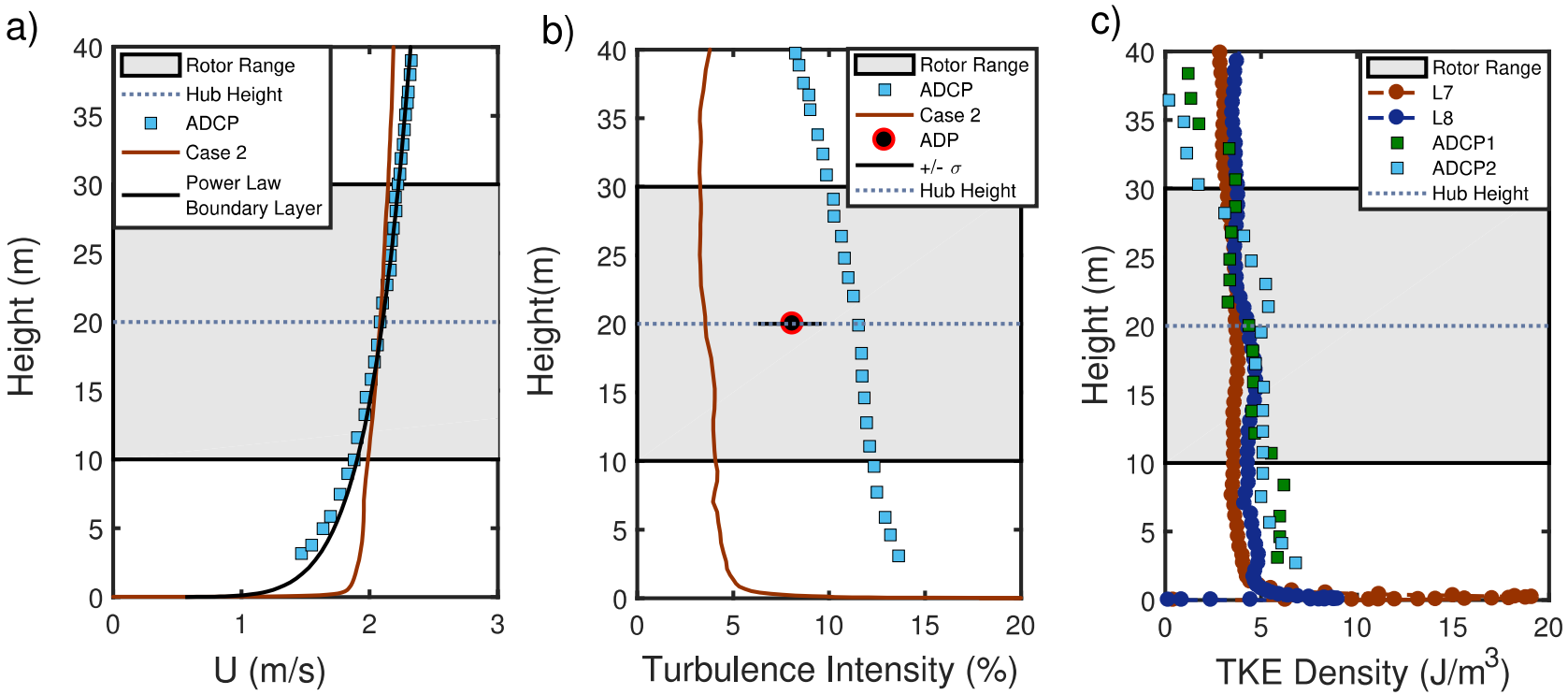

Figure 5.1: a) Velocity (m/s) b), Turbulence Intensity (%) c) and TKE density (J/m^3) Depth Profile Comparisons between simulation data and site measurements. Grey area corresponds to the rotor range for all sub-figures as well as a dotted blue line for the hub height. Solid red line indicates simulation data taken at the midpoint of the domain for case 2. ADCP markers are shown in blue squares and are the result of ensemble averaged profiles from both ADCPs. a) shows a theoretical power law boundary layer b) includes ADP single point measurement with a $\pm\sigma$ standard deviation range in a solid black line with median value in a black circle c) Shows TKE density lines at L7 and L8 compared to ADCP1 and ADCP2 at the aproximate same location.

a near identical profile as the ones shown. Case 2 (Injection of site information for TI and LS) was finally chosen instead of case 1(flat bathymetry trial run data) and the other trial cases due to improved convergence and profile results. Agreement with site data is high in the upper half of the water column for the no wave site data. Comparison between the models and the site data diverges strongly in the bottom 20% of the water column with an average error of 11% compared to 4.28% for the entire water column. As the site measurements go through ensemble averaging of several 5-minute profiles, comparison is expected to have some divergence. Several 5 minute stationary velocity depth profiles were found to be in agreement with simulation data near the bed, as well as having very strong accuracy in the rotor range (3.7% error). In order to have an improved model of the velocity profile during a tidal cycle it would be necessary to have a time varying inflow representing the main components of the tidal cycle to be able to compare similar sets of data.

Tidal energy converter analysis utilizes turbulence intensity and turbulent kinetic energy as important parameters for fatigue loading. Comparisons of the present simulation values to test site data will help with the validation of the model and understanding its limitations.

The turbulence intensity (TI) obtained from the model simulations Case 2 and site data (ADCP and ADP) are compared in Figure 5.1 b). Values of TI near the sea bottom show good agreement with the site data, but quickly reduces to about 5% TI for both simulation cases in the majority of the water column. ADCP ensemble averaged site measurements show a depth profile in the (9-14 % range) while the ADP showed a much lower estimate at hub height (8.6 $\pm$ 2 %), with margins within a standard deviation σ. Measurements from the ADP are mentioned as being of higher reliability in the ReDAPT report leading to some uncertainty of the TI magnitude from the site measurements. Preliminary simulations show similar results even when turbulence intensity profile magnitude, injected into the inflow, was increased to double or triple the value. Turbulence production is insufficient to keep turbulence intensity values above the 5% mark in comparison with site data; the lack of turbulence in the model could be attributed to the lack of larger eddies

coming from nearby land features, particularly eddies originating off of the coast of Eday during Ebb tide, and the aforementioned need for an oscillating inflow.

The availability of turbulent kinetic energy (TKE) Density depth profile site measurements allowed for a greater validation of the turbulent parameters for the simulation. TKE density $k_{rho} = \rho\overline{u_i' u_i'}$ is similar to the sum of the resolved k_{res}, only differing in its units (J/m^3) for site measurements, however the subgrid contribution was added and taken into account for the numerical data. Figure 5.1 c) shows profiles from the seabed mounted ADCPs located near probes L7 and L8 allowing us to compare to both probes. It is to be noted that the location of probes with regards to site measurements will not be precise yet still within a range of $\pm$ 50 m due to uncertainties in both bathymetry and ADCP location information. Close agreement within 3.5% average error is seen between site measurement and simulation data, only diverging near the upper boundary wall. Maximum values from the simulation data near the seabed were unable to be compared due to the placement of the seabed mounted ADCP. Absolute values of TKE density show appropriate levels of turbulence throughout the water column. This is in contrast to the underestimation of turbulence intensity that is highly sensitive to mean velocity non-dimensionalization of rms values, as well as site measurement sensitivity to post-processing detrending of the signal. A greater analysis of the turbulent kinetic budget will be analyzed in the results. This was done to best understand the manner and location in which turbulence energy was being produced and dissipated for further improvement of the model.

Spectral analysis was conducted to best contextualize the distribution of turbulent energy in the flow structure. Thus providing context of the wall modelled LES resolution capabilities and a comparison to site measurement spectra. The spectra shown was calculated to understand the frequency distribution in individual velocity components near the sea bottom as well as at hub height for the purposes of energy extraction.

Figure 5.2 a) shows a sample power spectrum density (PSD) ϕ_{ii} normalized by the variance σ_i^2 and the wave number κ for each velocity component in a one-dimensional

frequency spectra at hub height from a line probe at mid-domain . The inertial sub range -4/3 slope is also plotted to aid visibility with a dashed line, while the LES filter is shown with a dotted line. It is worth highlighting that for both frequency spectra plots shown in this section the LES filter size seems to filter appropriately by resolving inertial sub range sufficiently to capture more than 90% of the spectra energy for all three dimensions.

Hub height frequency spectra as seen in figure 5.2 a), for each velocity component, shows an increasing PSD ratio between components at the lower integral frequencies. The energy containing range in these lower frequencies show the u_i streamwise PSD as the dominant component and the vertical components integral energy containing range at a significant lower level than the other two components (span and streamwise). Anisotropy was visible at integral length scale frequencies with a higher value at u_i followed by u_j and u_k. Hub Height spectra was in good agreement with similar spectra from test site data seen in ReDAPT reports.

Figure 5.2 b) shows the cumulative sum of the energy spectra $E(k)$ for each component normalized by $\overline{u_i^2}$ for three vertical positions of the water column $z = -2.5, = 15, -20\ m$ with dash-dotted, dashed and solid lines respectively colored by dimensional component. Dotted vertical line shows the location of the filter, while the horizontal dotted line shows the minimum recommended ratio of energy resolved. This plot can be used to verify that at locations near the seabed all components are appropriately resolved without getting close to filtering the viscous dissipation range. Cumulative spectra also shows the increased energy at lower wave numbers as the vertical position furthers away from the seabed due, in part, to the growing bandwidth of the inertial subrange to lower and lower wave numbers with the distance to the seabed. Frequency spectra at both hub height, as well as, at locations near the wall show a great deal of anisotropy, particularly more pronounced at lower frequencies in the integral energy containing range.

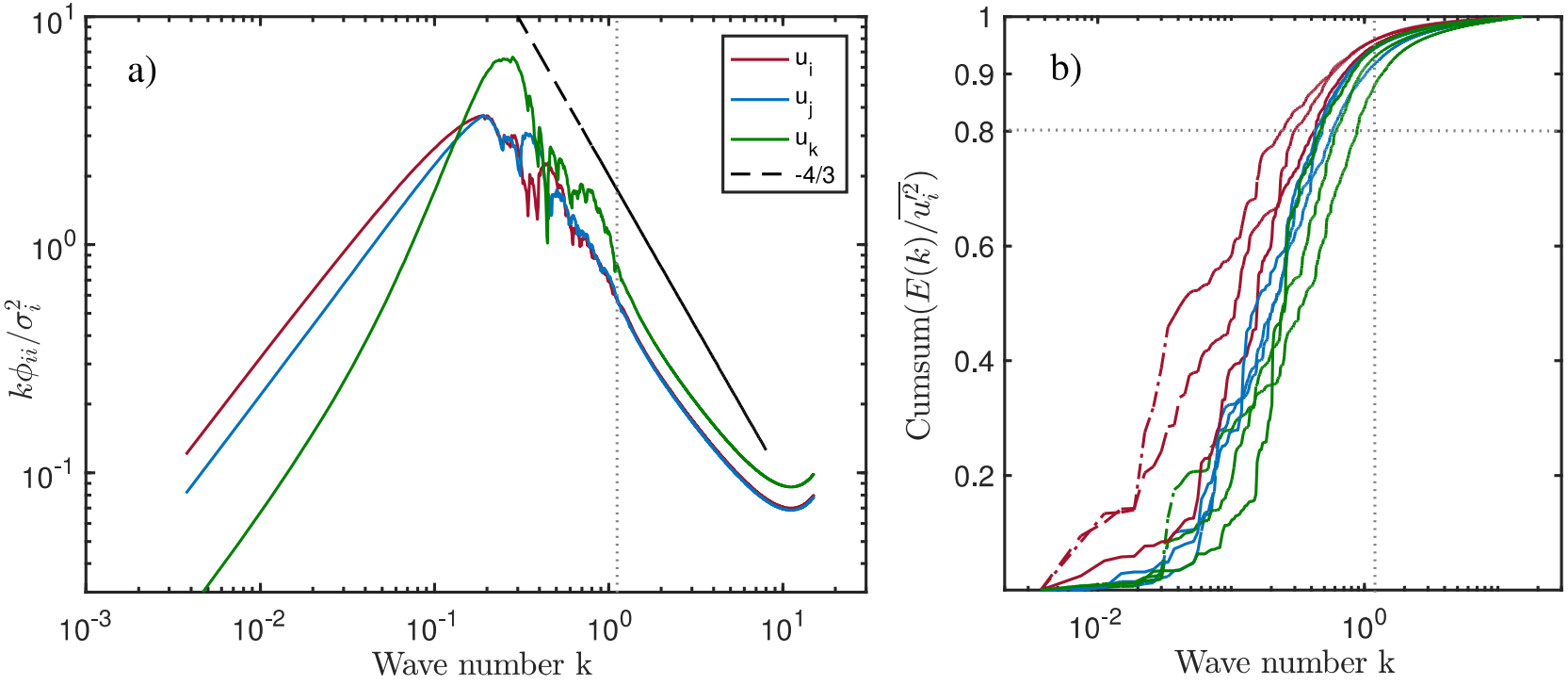

Figure 5.2: a) One dimensional normalized frequency spectra at hub height for line probe at mid-domain for all components. Solid lines show: velocity components u_i (blue),u_j (green),u_k (red). Dashed line shows the inertial subrange bandwidth slope while the dotted line shows the location of the LES filter. b) Cumulative Spectra plotted versus wave number k for three vertical points s at the same line probe as a). Color of lines corresponds to the same velocity component while solid lines are at $z = -20\ m$ dashed lines at $z = -10\ m$ and dotted and dashed lines at $z = -2.5\ m$

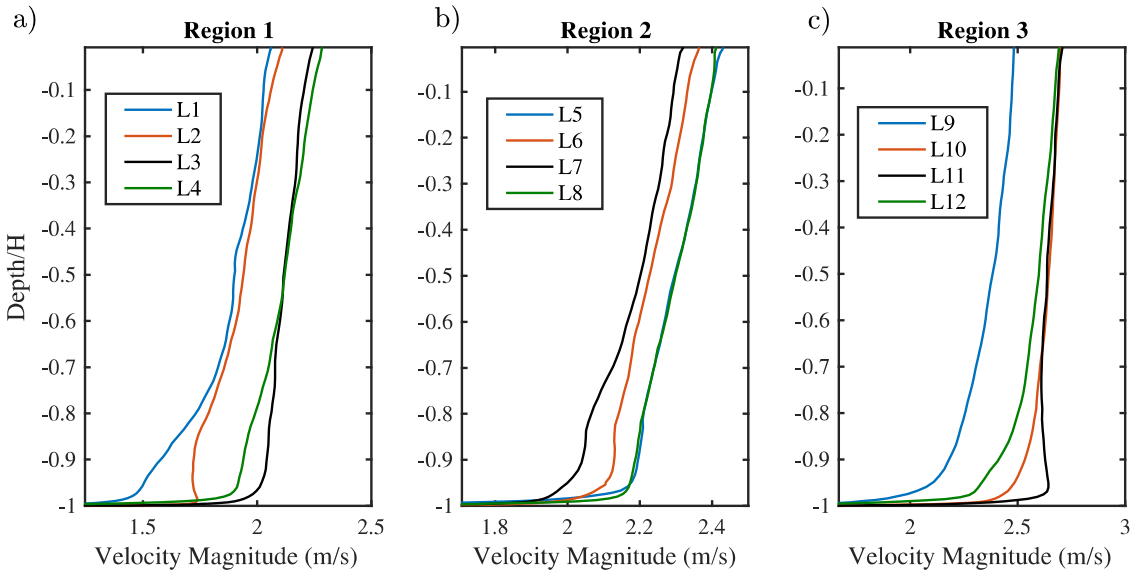

Figure 5.3: Averaged velocity magnitudes plotted along the water column: From left to right, a) Line probes in region 1 b) Line Probes in region 2 c) Line probes in region 3. The vertical axis in all subplots have height normalized by local depth. For location of each line probe refer to tables 1-3.

5.4 Averaged Velocity Profiles

The model predicted depth varying velocity profiles for all three regions are depicted in Figure 5.3. As already seen in Figure 4.5, water depth reduces as the domain evolves in the streamwise direction; this causes a decrease on the cross-sectional area of the flow which in turn creates an accelerating effect on the velocity. Probe locations L1 & L2 in Figure 5.3 (a) show the velocity profile changing from the initial input at the inlet, (as stated before, equal to 1.7 m/s) into a developed profile where L1, being closer to the inlet, resembles the injected profile more closely than probe L2, since the flow field is still developing.

In region R2 Figure 5.3 (b) the velocity magnitude continues increasing in comparison to region R1. The initial bottom 20% of the water column near the seabed shows different behavior across the probes. Probes L5 and L8, located in the mid-span direction, show an acceleration of the flow leading to a rapid increase of the velocity from the sea bottom with a bend into the linear increase with height at 5% of the water column while L6 and L7 have the same increase at the 18% mark.

Region R3 (in Figure 5.3(c)) shows the greatest effect of the ramp up effect taking velocities up to 2.6 m/s at hub height. Profile shape for probes L9,L10 and L12 show a profile more similar to the expected power law with a slower increase in velocity in the near sea bottom regions. Probe L11, however, shows a bulge in the bottom tenth of the water column before returning to the power law behaviour in the other lines. It is positioned at the same streamwise position as probe L10 yet differs strongly in the bottom quarter. This shows the irregular bathymetry that shifts the spanwise and vertical velocity components, rapidly creating a full 3D flow. Absolute velocities in the spanwise and vertical directions dissipate for most of the water column from their maximum value near the seabed.

Figure 5.4 shows the averaged depth profiles for vertical velocity (u_k). As seen in the previous studies by Flack and Schultz (2014); Jimenez (2004); Stoesser (2013) with wall irregularities such as dunes or roughness effects, irregularities on the wall have local effects highly dependent on local bathymetry which then result in instantaneous vertical bursting events which can rise through the water column. Non-

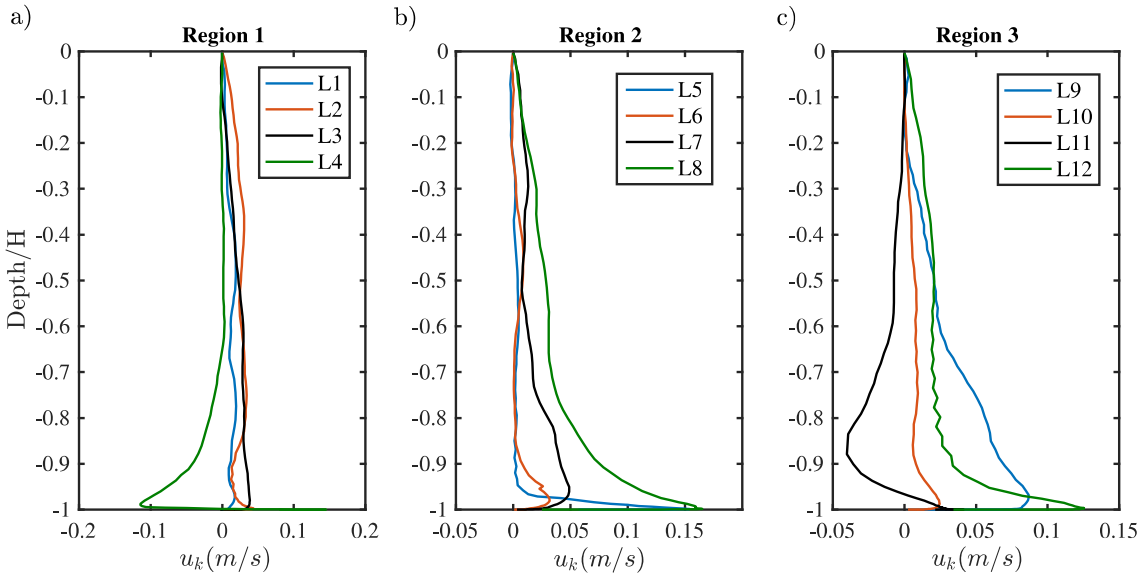

Figure 5.4: Velocity depth profiles for vertical direction: Regions 1-3 from are left to right.

uniform time-averaged u_k profiles at different line probe locations in Figure 5.4 would suggest the local effect of the bathymetry seen, not only for instantaneous events but for possibly sustained vertical movements as well. Regions R2 and R3 show averaged vertical velocity that decreases with distance from the sea bottom. Sudden vertical depth changes in bathymetry increases the vertical velocity values, and these high vertical velocity areas dissipate in magnitude at a lower rate than at areas with more uniform depth.

Velocity analysis of the streamwise and vertical directions show the influence of the bathymetry at all regions. The decrease in maximum depth from the initial domain to the outlet will throttle the maximum velocity magnitude while creating vertical motions for the bottom 10% of the water column.

5.5 Turbulence Statistics

5.5.1 Reynolds Stresses

The effect of the sea bottom on turbulence parameters can only be analyzed properly with higher order statistics regarding turbulent fluctuations in the domain. This section analyzes the main energy components of the Reynolds stress tensor in addition to different turbulence parameters important to tidal device resource and loading.

Figures 5.5-5.8 show the depth profiles for diagonal Reynolds stress components $\overline{u_i u_i}$ as well as $\overline{u_i u_k}$ (streamwise, spanwise, vetical for $u_{i,j,k}$ respectively . Components $\overline{u_i u_j}$ and $\overline{u_j u_k}$ are not shown due to their small contribution to the overall tensor for all line probes shown in Table 1. The shape of the depth profile remains almost constant for $\overline{u_i u_i}$ and $\overline{u_j u_j}$ with a peak very close to the sea bottom which quickly dissipates above in the water column to a constant value of $0.01(m^2/s^2)$ for the streamwise diagonal component $\overline{u_i u_i}$ and $\overline{u_j u_j} = 0.005(m^2/s^2)$ for the spanwise diagonal component. These two aforementioned Reynolds stress components show a difference only in the peak near the sea bottom which increased with the streamwise position (x_i) across the regions due to increased u_i.

Figure 5.7 shows the Reynolds stress component for the vertical direction ($\overline{u_k u_k}$). Maximum values for $\overline{u_k u_k}$ decreased from R1 to R3, yet had a strong dependence on spanwise location, as seen in the difference between line probes within each region. All line probes show a linear growth in the first bottom 10-15% of the water column except for lines 9 and 12, which show a peak near the sea bottom. Lines 3 and 4 in R1 have their maxima at 0.6 of the depth over height ratio. R2 holds similar behavior for all 4 probes with a sustained maximum from 0.8 to 0.6 in the water column while R3 holds the strongest bursts close to the sea bottom shown as peaks. In certain cases at locations near the sea bottom the profile has a positive peak which quickly changes to the negative profile. For all line probes the diagonal $\overline{u_i u_i}$ component was the highest value, followed by $\overline{u_j u_j}$ and $\overline{u_k u_k}$ having comparable magnitudes to the secondary stress $\overline{u_i u_k}$. The average ratio between diagonal components at hub height are 1:0.6:0.45.

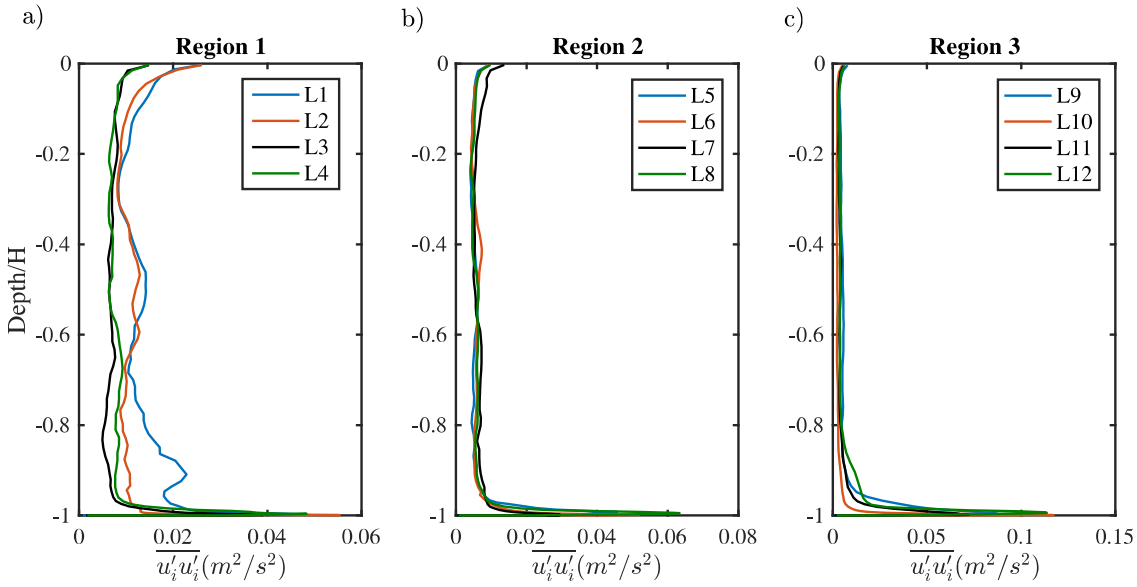

Figure 5.5: Streamwise Reynolds Stress $\overline{u_i'u_i'}$ depth profile: Regions 1-3 from left to right.

The observation of the main components of the Reynolds stress tensor shows a weak dependency on bathymetry throughout most of the water column. Peak values of Reynolds stress increase with the streamwise direction of the domain only near the sea bottom. Negative values for the $\overline{u_iu_k}$ reinforce the need to analyze previously mentioned vertical motions in the velocity analysis due to their high importance to the turbulence budget.

5.5.2 Length Scales

Integral turbulence length scales were calculated using a time autocorrelation for each line probe with Taylor's frozen turbulence hypothesis as shown in equations 13-15. The autocorrelation coefficient B_{ii} is normalized by its rms value $u_{i,rms}$.

$$B_{ii}^{norm}(\hat{t}) = \frac{\overline{u_i'(t)u_i'(t+\hat{t})}}{u_{i,rms}^2} \tag{5.1}$$

A time autocorrelation is calculated by comparing the velocity at a point with itself at different moments in time. The changing time is represented by adding $\hat{t}$ to the original data point at time t.

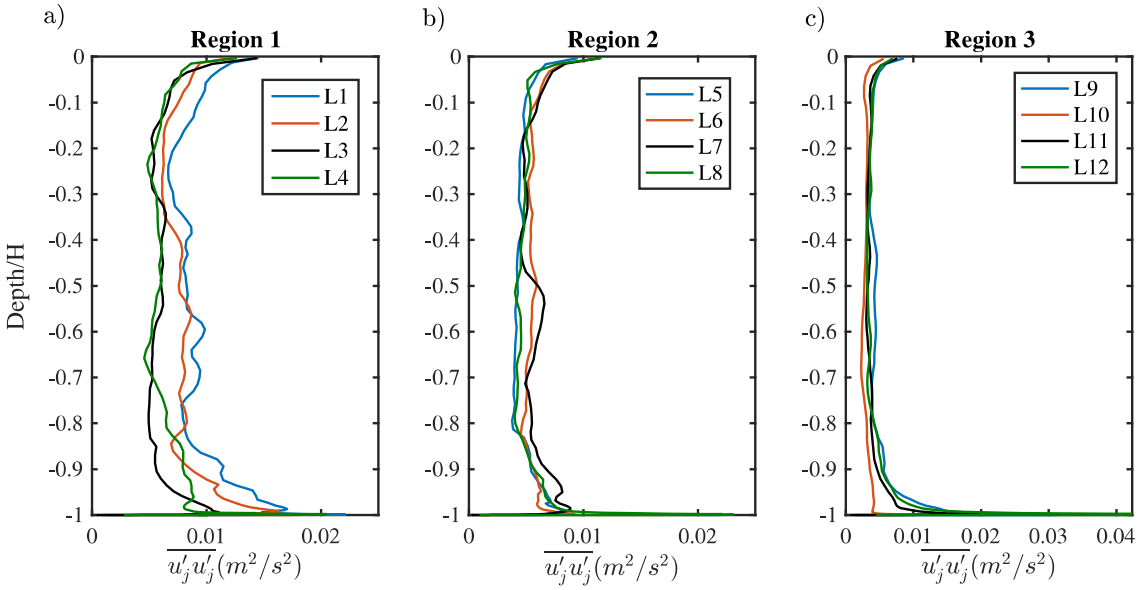

Figure 5.6: Spanwise Reynolds Stress $\overline{u_j'u_j'}$ depth profile: Regions 1-3 from left to right.

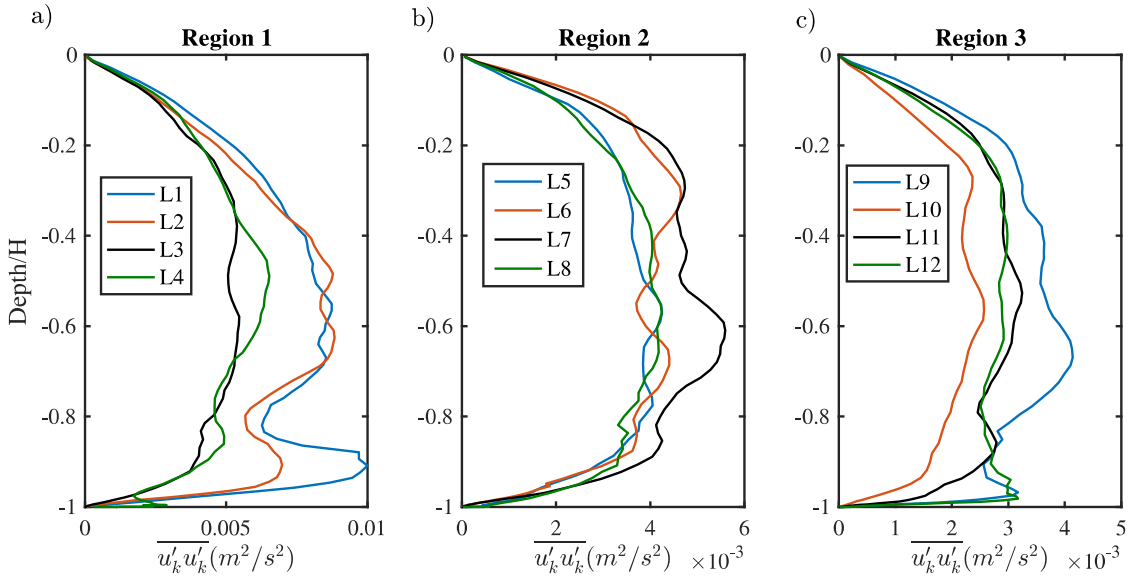

Figure 5.7: Vertical Reynolds Stress $\overline{u_k'u_k'}$ depth profile: Regions 1-3 from left to right.

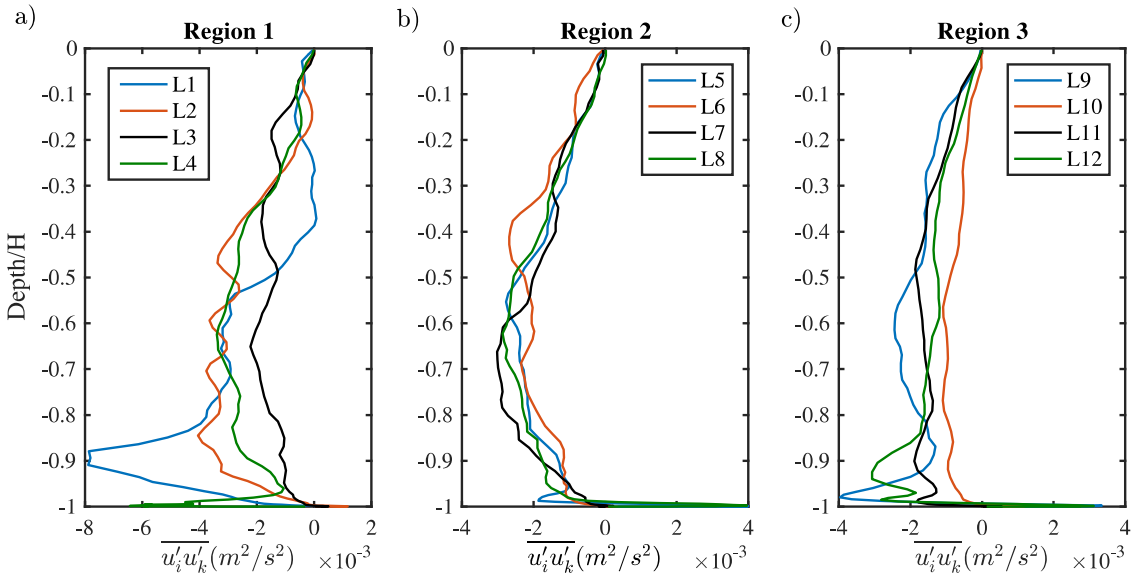

Figure 5.8: Cross streamwise-vertical Reynolds Stress $\overline{u_i'u_k'}$ depth profile: Regions 1-3 from left to right.

The integral time scale T_{int} is obtained from the integration of the time autocorrelation coefficient. This is in turn transformed into a measure of length L_{int} which is the basis of the results presented here.

$$T_{int} = \int_0^\infty B_{ii}^{norm}(\hat{t})d\hat{t} \tag{5.2}$$

$$L_{int} = \overline{u_i}T_{int} \tag{5.3}$$

The values of the integral length scales for three regions are shown in Figure 5.9. Region 1 follows similar behavior as seen for previous turbulence values with L1 & L2 showing development of the flow along the domain. Regions 2 & 3 show an increase of length scales along the water column up to the first quarter of depth followed by a quasi-constant length scale in the outer layer of the water column. Spanwise changes in bathymetry show minor changes in length scale depth profiles, however always preserving a similar depth profile shape. Depth probes at R3 show an increase of 15% in the outer layer constant length scale value compared to probes in R2. The shape of the profile of a rapid increase with a constant value at the 15-20% shows good agreement with profiles reported in other SEM LES channel simulations

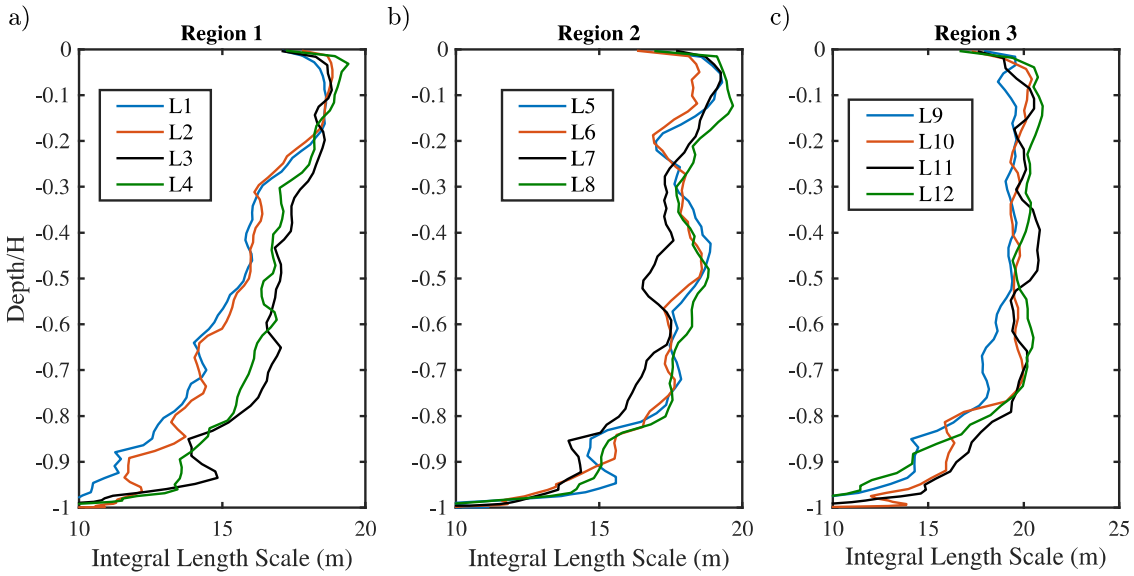

Figure 5.9: Integral Length Scale Depth Profiles.Regions 1-3 from Left to right.For legend see caption on 5.3

(Creech et al., 2017), site measurements from the Sound of Islay (Milne et al., 2017), and theoretical length scale depth equations by Nezu and Nakagawa (1993).

Alternative length scale calculation methods include the spatial autocorrelation and spectral method shown in chapter 4 . The noise within the spectral plot of turbulent kinetic energy makes estimation of the length scale difficult to a pin-point precise degree since it is dependent on finding the position where the -5/3 inertial sub-range slope ends, with that in mind the integral length scale may be approximated to a range of (0.07-0.05) Hz. This is converted into a spatial length scale through the relation $L = u/f$ yielding a length scale range of (28-40m) for a local velocity of 2 m/s at the midpoint of the domain and water-column. Two-point correlations analysis shown in figure 4.14 can be used to calculate length scales by the integration of the B_{11} up to the crossing of the first zero value. By using the same data point to compare to the spectral and autocorrelation the length scale was calculated at 16.1 m. Length scales based on temporal autocorrelation theory at the same position and velocity as the spectral and two-point correlation equal 18.3 m. This gives us three different values, one for each method. The autocorrelation

and two-point correlation are within 12% of each other while the spectral method is greater by an approximate factor of 2 even when contemplating the noise of the spectral plot. The correlation methods appear to calculate a half channel depth while the spectral plot would approximate the whole channel depth. Further discussion of integral length scales will use the half channel depth to be consistent with other site measurements previously mentioned, however use of the entire channel depth as an integral length scale may also be valid.

5.5.3 Turbulence Kinetic Energy Budget

Turbulent kinetic energy budget analysis was done for each region in an effort to view the vertical and streamwise location of highest TKE production. Figure 5.10 shows TKE Production $\mathcal{P}$ plotted vs TKE dissipation ϵ with a dotted line showing where they are of equal magnitude. Each subplot contains the 4 line probe points for its respective region colored by vertical depth. All three regions show the highest turbulence production and dissipation near the seabed. Net TKE, when subtracting ϵ from $\mathcal{P}$ remains positive for all regions. The point nearest to the boundary walls for each line probe is the exception, quickly crossing over to a positive net value. Production was kept at near constant levels for all regions with dissipation having the highest range throughout the water column in region 3. It is important to highlight the positive net turbulence for the entire domain, this would suggest a sustained level of TKE in opposition to the first impression of high over dissipation from turbulence intensity results.

5.6 Instantaneous Plane Analysis

The use of high order turbulence statistics allow us to have a better understanding of the turbulent flow. However, an analysis of instantaneous velocity and vorticity values will shed more light on the possibility of quick, high magnitude events relevant to turbine loading.

Figure 5.11 shows instantaneous cross-sectional YZ surfaces at different points

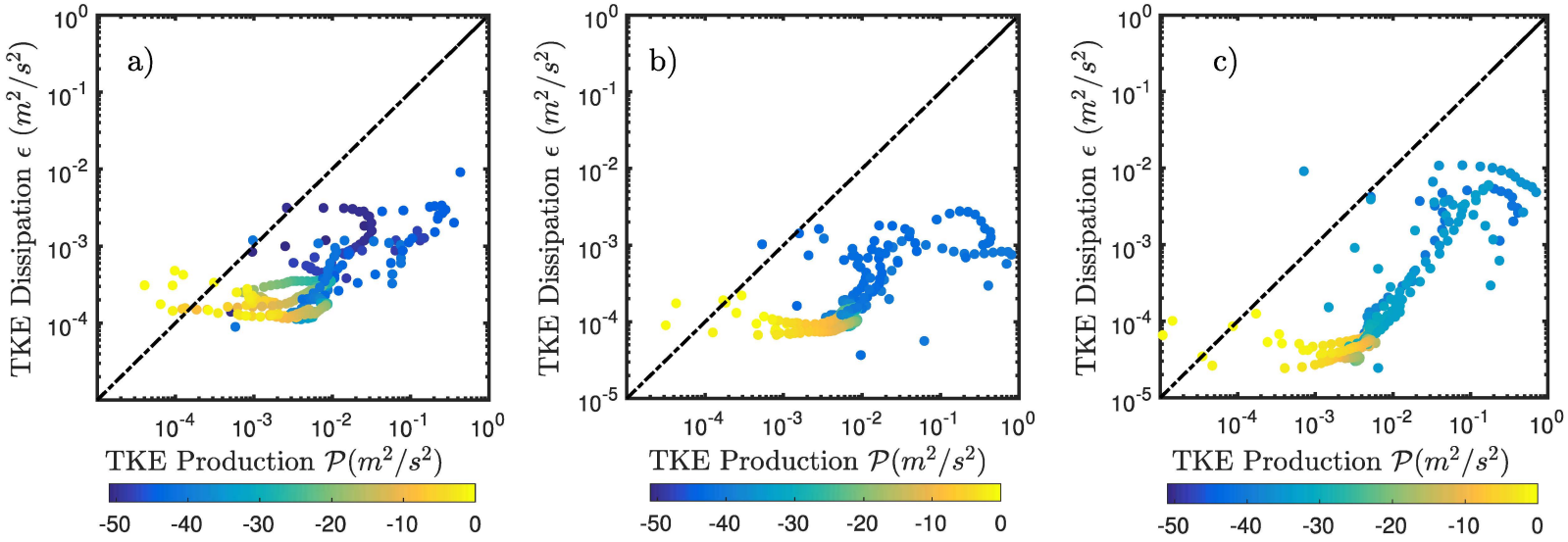

Figure 5.10: Turbulence production plotted against TKE dissipation for all line probes in each region (a) Region 1 b) Region 2 c) Region 3)). Each point shows a location in the water column colored by its depth (m). Dotted line shows the equilibrium point where dissipation is equal to production.

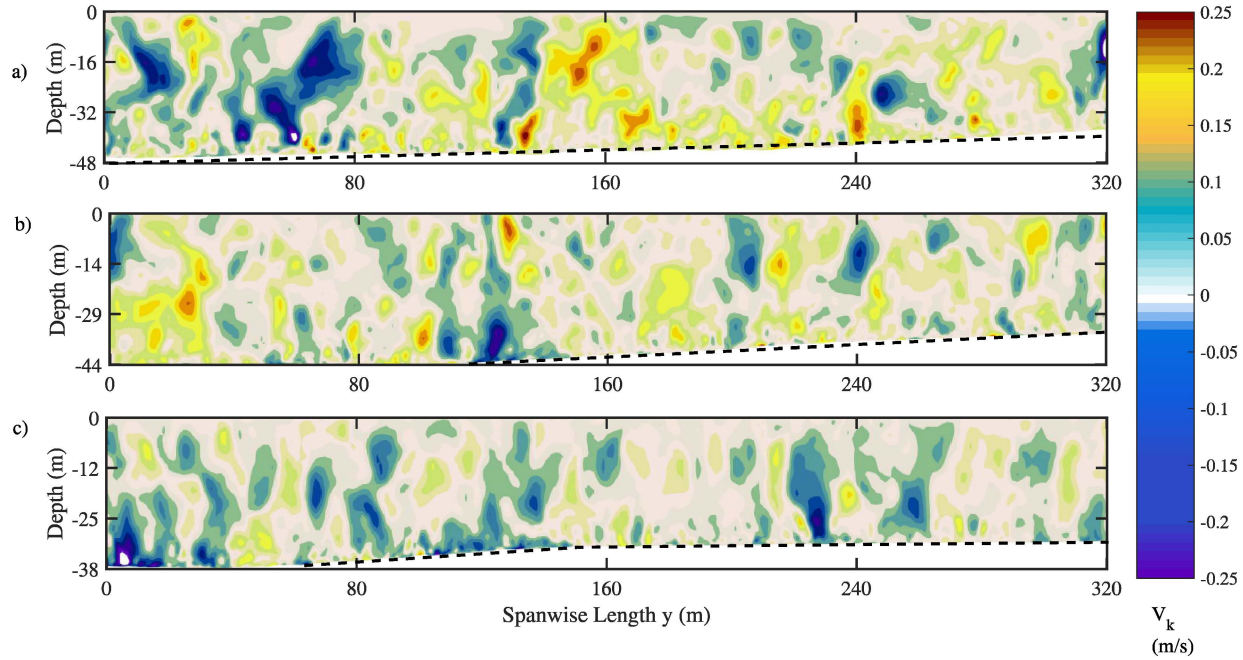

Figure 5.11: Instantaneous planar slice of u_k showing spanwise(y) plotted against depth(z) colored by u_k magnitude for selected points in every region: a)R1 at x=0, b) R2 at x=350, c)R3=900. Dotted line emphasizes bathymetry shape.

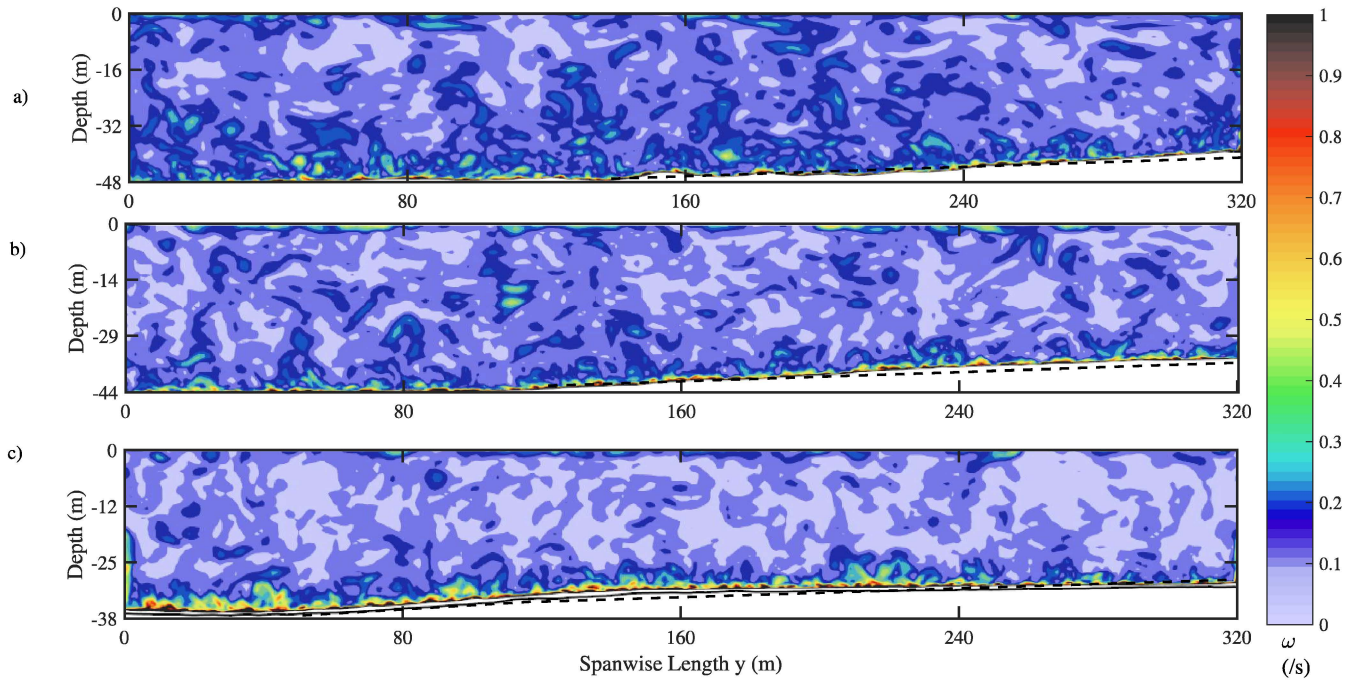

Figure 5.12: Instantaneous planar slice of ω_k showing spanwise(y) plotted a against depth(z) colored by ω_k magnitude for selected points in every region: a)R1 at x=0, b) R2 at x=350, c)R3=900. Dotted line emphasizes bathymetry shape.

along the domain colored by instantaneous vertical velocity u_k in order to see the variation of bursting events at a singular point in time at different depths. Highest value of absolute u_k is seen near to the sea bottom walls, dissipating as it travels along to the surface as was expected in accordance with Reynolds stress profiles for u_k. Instant velocity contours were seen in higher magnitude in the areas where depth was at its deepest for all regions due to interaction of the flow with the sea bottom. Here the absolute value of u_k velocity contours was highest in the subplot Figure 5.11 a), at the plane with the lowest depth. Maximum absolute values of u_k decreased in the subsequent planes further downstream as maximum depth decreased. High absolute u_k velocities at depths close to the rotor plane suggest the possibility of sustained bursting events (sweep and ejections) at heights relevant to tidal energy extraction devices.

Figure 5.12 shows instantaneous cross sectional YZ surfaces at the same locations as in Figure 5.12 for vorticity magnitude. For all YZ cross-sections high vorticity was seen originating from the sea bottom, due to shear stresses decreasing proportionally to the distance from the sea bottom. High vorticity values are seen for a greater proportion of the water column at more shallow depths of the domain yet average vorticity is higher at deeper locations. For instantaneous effects, high vorticity was seen in all regions as high as mid-column. Turbulent structure analysis is needed to identify the permanence in time of these aforementioned high vorticity regions, in order to view them as coherent structures related to bursting events or other structures of importance. However this is beyond the scope of this study and the authors will seek to investigate further in later work. Instant cross sections show the correlation between vertical movement and high vorticity near the sea bottom due to shear stress turbulent production. Evidence stemming from Reynolds stress profiles as well as instant cross sectional plots suggest high energy turbulent events previously mentioned as being possible origins of TKE production. A more complete turbulent structure analysis would be necessary to appropriately analyze these values to measure their lasting nature in magnitude and time.

5.7 Discussion

The work presented here shows the capabilities of LES when aided by site data to create a full picture of flow at realistic bathymetries in terms of flow velocities and turbulence statistics. High resolution grids are capable of showing unsteady fluctuations that would be lost in time averaged models, thus providing greater information on the mechanisms in which turbulence is produced and dissipated at different regions of the domain and its depth wise evolution. The turbulence profiles injected into the domain by way of the synthetic eddy method were attempted by both Case 1 and Case 2, these corresponded to an isotropic turbulence depth profile and to the diagonal components of the Reynolds stress tensor respectively. Flow development in the domain, modified by the wall boundary conditions, showed a waning influence of these profiles as the domain progressed, giving similar results for both cases. This would suggest that the turbulence injected was not the main component in the domain but the turbulence continually produced by the boundary conditions, particularly at the seabottom. The modeled site shows good characteristics in comparison to similar canonical flows. The Reynolds stress ratios at 5m above the seabed from this present work showed a 1:0.8:0.45 ratio for $\sigma_u/\sigma_u, \sigma_u/\sigma_v, \sigma_u/\sigma_w$ ratios respectively. This compares well with Milne et al. (2017) who measured 1:0.71:0.55 at lab experiments and similar values for site measurements and Nezu and Nakagawa (1993) who reported 1:0.8:0.68 ratios.

Turbulence statistics, in terms of turbulence intensity are over-dissipated in comparison to site measurements. Steady velocity boundary layers experiments at high Reynolds number show a similar decrease to 5-10% of turbulence intensity for rough and smooth surface boundary layers (Castro et al., 2013; Alfredsson et al., 2012), this is similar to the turbulence intensity shown in the present simulation and show that oscillating tide induced velocity might be needed to have a full explanation of the origin of turbulence intensity as well as the addition of direction reversed velocity component during Ebb tide. Turbulent length scale magnitudes ranging from 10-20 m, calculated in the model compared well with site measurements such as those taken 10 m from the seabed at the Bay of Fundy (McCaffrey et al., 2015) who found

an average length scale of 11.6 m, and the 11-14 m found by Milne et al. (2017) at the Sound of Islay. All analyzed turbulent statistics show the effect of the sea bottom in varying degrees, especially in increased Reynolds stress maxima near the seabed. These averaged Reynolds stress maxima suggest even higher energy intermittent turbulent events that requiere further statistical study. The cross-component $\overline{u_i u_k}$ at all probes in figure 5.8 show a negative value for most of the water column.This would suggest so called 'bursting events' dominating the domain. Bursting events are evident when $\overline{u_i u_k} < 0$, these events are responsible for 80% of total turbulence production according to Kim et al. (1971) & Kline et al. (1967). The influence of the changing sea bottom on most turbulent parameters and statistics are limited on average to the first bottom fifth of the water column. This area of influence could be compared to the area of influence of roughness elements on walls in canonical flows. It should be noted that the results given apply to a particular flow velocity at flood tide for the specific site. The influence of flow velocity and tidal cycle is expected to have major changes on turbulence parameters and even the shape of the velocity profile. The analysis and results from the present simulation suggest a stronger influence of the sea bottom bathymetry on turbulence statistics than previous flat channel simulations. Although the computational resources required are significant, the data gathered and its resultant turbulent parameters, give insights into turbulent production and dissipation. A more complete context of turbulence at the site shows the usefulness of high resolution LES, giving us a full picture of the flow for particular tidal energy sites. Improved high resolution simulations that provide understanding of turbulence near the seafloor bottom and its structure are important, not only for the tidal energy sector but for many offshore applications.

CHAPTER 6

TURBULENT STRUCTURE OF A FLOOD TIDE

6.1 Introduction

This chapter presents turbulence structure analysis carried out on the data from the flood tide Large Eddy Simulation presented and discussed in Chapters 3 and 4. The aim of the analysis in this chapter is to characterize the spatial and temporal attributes of the turbulence and coherent vortical structures of the flow as shaped and modified by the bathymetry of the site. Quadrant analysis for multiple depth probe locations is used to give a three-dimensional statistical understanding of bursting events, as modified by the seabed. The results delve into highly energetic coherent structures of a sufficiently large spatial and temporal size, connected to bathymetry variation. The following results are presented beginning with a turbulent structure study of the vertical water column for several points of the domain described in the previous section. This aims at understanding the distribution of turbulent kinetic energy for all three dimensions of the flow, as well as the mechanisms for its production and distribution. Statistical quadrant analysis is shown in the second

part of the results section. This portion of the analysis aims to examine the temporal and spatial characteristics of the turbulent producing $\overline{u_i u_k}$ Reynolds stress, by a probabilistic approach. Finally, coherent structure visualization is presented along with a discussion of its origins and connections to the statistical and structural characteristic events of the turbulent flow.

6.2 Anisotropy Analysis

6.2.1 Anisotropy Tensor and structure parameter

It is fundamental to identify and quantify the dominance of each individual component of the turbulent flow field, as well as recognize the importance of the main cross correlational components that lead to turbulent production. Understanding the main sources of turbulent kinetic energy at a tidal site, in addition to the mechanisms with which the sea bottom distributes TKE in every direction from the wall shear, is of utter importance to understanding the structure of the flow and how it deviates from smooth channels.

The Reynolds stress anisotropy tensor B_{ij} was first introduced by Choi and Lumley (2001) in order to isolate the Reynolds stress tensors' diagonal components from its contributions to the overall kinetic energy. The anisotropy tensor is defined in Eq. 6.1:

$$B_{ij} = \frac{\overline{u_i u_j}}{\overline{q^2}} - \frac{\delta_{ij}}{3} \tag{6.1}$$

The $\overline{u_i' u_j'}$ represents each component of the Reynolds stress tensor, normalized by $\overline{q^2}$. The mean kinetic energy $\overline{q^2}$ is equal the sum of the diagonal components of the Reynolds stress tensor $\overline{u_i u_i}$. The δ_{ij} equates to the the dirac function which will isolate the contribution of the diagonal components. This forces the diagonal components of the anisotropy tensor to a range of $-1/3 < B_{ij} < 2/3$. Isotropic cases reduce the diagonal components to 0, while 2/3 shows complete one dimensional dominance and thus complete anisotropy. It is worth noting that the sign of the diagonal components shows the contribution to the overall mean Reynolds stress.

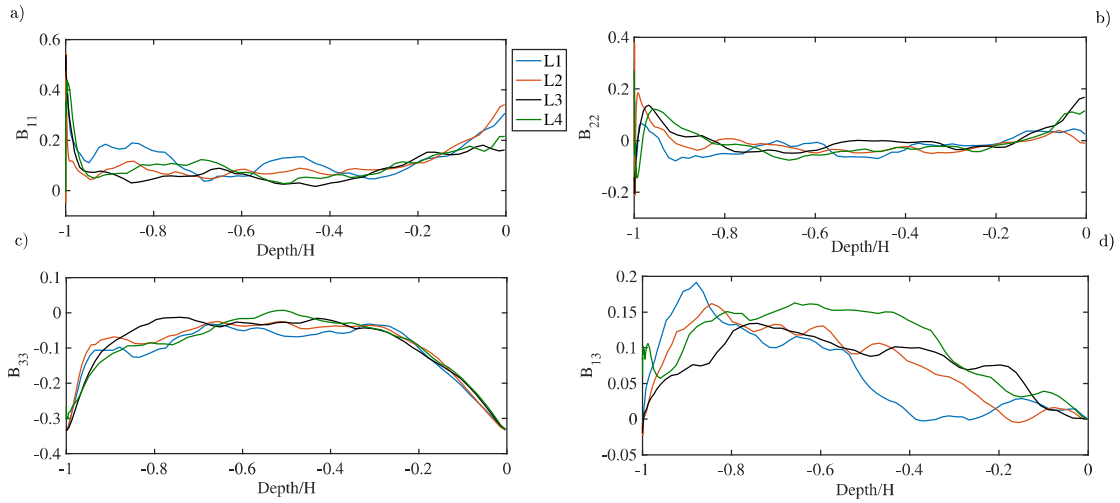

Figure 6.1: Region 1 Anisotropy tensor depth profiles: a) $\overline{B_{11}}$, b) $\overline{B_{22}}$, c) $\overline{B_{33}}$, d) $\overline{B_{13}}$. Depth is non-dimensionalized by dividing the vertical position Depth and dividing it by the maximum local depth H.

The Reynolds stress anisotropy tensor was calculated with the objective of quantifying the importance of component of the flow, and with it have a general idea of the anisotropic nature of the flow. Figures 6.1, 6.2 & 6.3 show the diagonal components of the anisotropy tensor $\overline{B_{11}}$, $\overline{B_{22}}$, $\overline{B_{33}}$ and the $\overline{B_{13}}$ component plotted as depth profiles, for all line probes divided into their respective regions as previously shown in table 4.1 (chapter 4). The non-diagonal component $\overline{B_{13}}$ is included due to its importance to turbulent kinetic energy in the flow. Also called the structure parameter by Townsend (1961), it measures the amount of turbulence extracted in the form of Reynolds shear stress from the available turbulent kinetic energy (Piomelli et al., 2002). The rest of the components in the B_{ij} tensor were of very low magnitude in comparison to the structure parameter and the diagonal components as the only main cross component was between the wall driving the flow and the main streamwise component.

Figure 6.1 shows anisotropic behaviour for all probes up to values of approximately the bottom 20% of the water column. At the sea bed boundary the streamwise component B_{11} reaches values up to 0.42, higher than the maximum B_{22}=0.19 spanwise component. The vertical diagonal component B_{33} has no effect on the

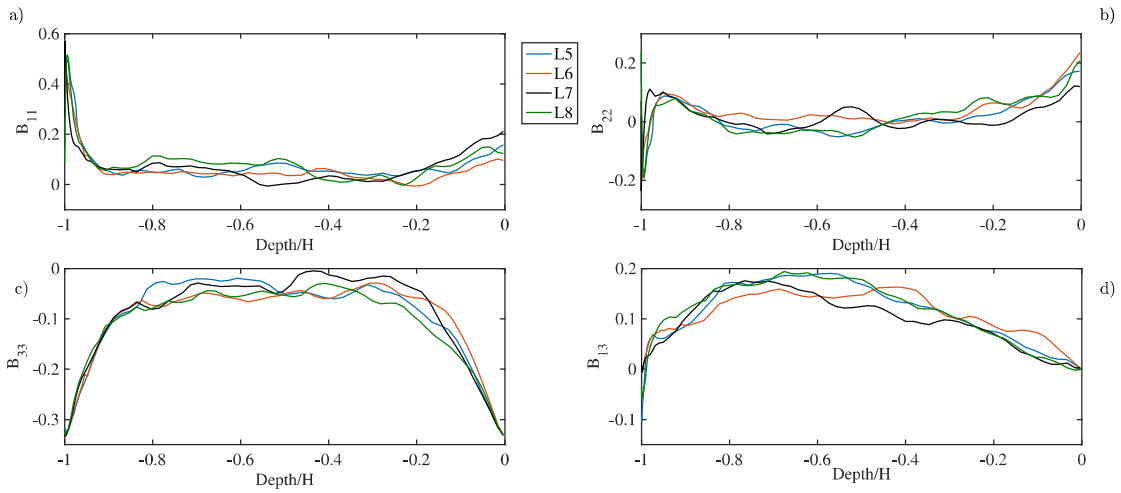

Figure 6.2: Region 2 Anisotropy tensor depth profiles: a) $\overline{B_{11}}$, b) $\overline{B_{22}}$, c) $\overline{B_{33}}$, d) $\overline{B_{13}}$. Depth is non-dimensionalized by dividing the vertical position Depth and dividing it by the maximum local depth H.

Reynolds stress at the wall boundary, yet receives the lost contribution from the other two diagonal components before hitting isotropic behaviour at mid-column. The structure parameter differed wildly, depending on line probe location, yet was consistent in value range between 0.1-0.15 up until the mid-column which coincides with the most isotropic point.

Regions 2 and 3 (figures 6.2 and 6.3 respectively) showed similar results in all 4 of their probes. This would suggest a dependency on the streamwise location of the domain rather than a spanwise location variability, due to depth being predominantly a streamwise variation in the domain. Region 2 does not reach full isotropy but shows similar behaviour than region 1 at the mid-column where the streamwise component redistributes TKE to the other minor components. However, the vertical component B_{33} never reaches full equality in contribution to the other components. Region 2 differs from region 1 with a larger streamwise contribution to the TKE while the structure parameter demonstrates a larger efficiency when extracting TKE from the shear stress. The structure parameter only decreased to levels below 0.1 from all line probes in the top 20% of the water column and showing maximum efficiency between the $Depth/H = (-0.7\ to\ -0.6)$.

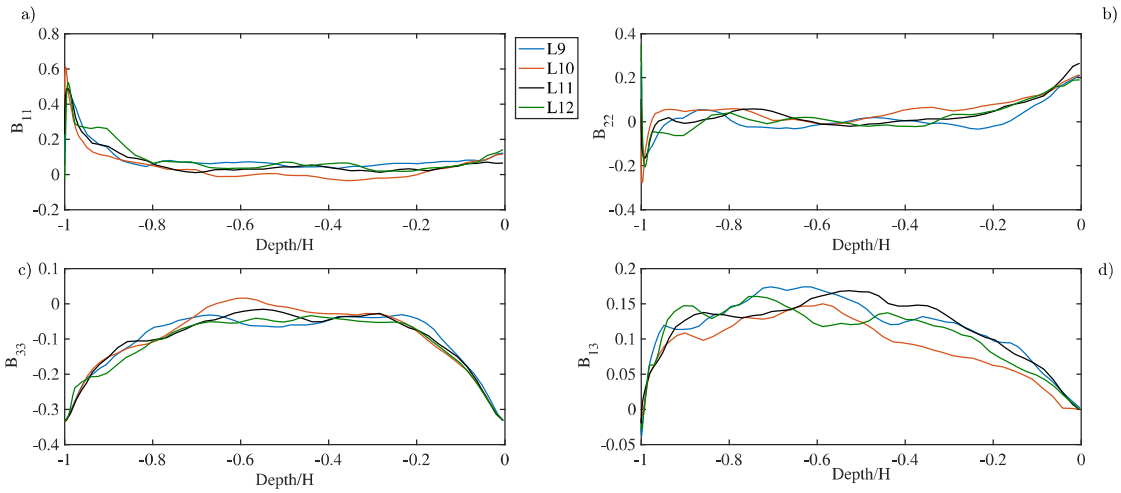

Figure 6.3: Region 3 Anisotropy tensor depth profiles: a) $\overline{B_{11}}$, b) $\overline{B_{22}}$, c) $\overline{B_{33}}$, d) $\overline{B_{13}}$. Depth is non-dimensionalized by dividing the vertical position Depth and dividing it by the maximum local depth H.

Region 3 continued showing a greater anisotropic behaviour than the previous regions. At the wall, line 10 showed near complete streamwise dominance with a maximum B_{11} value near 0.6 and spanwise B_{22} values decreasing to near zero values for the majority of the water column. Near isotropic values were seen for a lesser portion of the water column than in regions 1 and 2 . Structure parameter efficiency remained semi constant for values not near the sea bed boundary and the mid column, yet never reaching the high efficiencies of region 2. The values obtained for the anisotropy tensor are similar to those of rib-roughness and irregular roughened boundary layers reported experimentally and by DNS and LES simulations Krogstad and Antonia (1999), Roussinova (2009),Smalley et al. (2002) and Piomelli et al. (2002) respectively.

It is notable that the structure parameter reported by the previous authors only reached higher values than 0.15 for short periods near the boundaries and held constant values between 0.12 and 0.14. All line probes across regions showed lesser values of anisotropic tensor values near the walls than the smooth turbulent DNS results by Spalart (1988) at a momentum Reynolds Number $Re_\theta = 1410$. This is consistent with the conclusions of Krogstad and Antonia (1999) and Piomelli et al.

(2002). Piomelli argued for a roughness effect that would decrease anisotropy from near the wall. In the case of the present results this holds when comparing between different regions. Region 2 and region 3 have irregular changes in bathymetry more pronounced than in region 1 as well as having these bathymetry changes occupying a larger percentage of the water column.

6.2.2 Anisotropy Invariant map

Choi and Lumley (2001) created a visual technique for identifying the nature of the turbulent flow as one, two or three dimensional and all the intermediary states based on the previously utilized anisotropy tensor. There are several versions of Lumley's anisotropy mapping, yet we will refer to his original Anisotropy Invariant Map (AIM) determined by plotting the invariants of the B_{ij} tensor. The calculation of the second (II) and third (III) invariant are as follows:

$$II = -\frac{B_{ij}B_{ji}}{2} \tag{6.2}$$

$$III = \frac{B_{ij}B_{jk}B_{ki}}{3} \tag{6.3}$$

The Lumley triangle is bound by 3 curves, each showing a different turbulent state. Complete isotropy is located at areas near (0,0). Figure 6.4 from Simonsen and Krogstad (2005) shows a more graphic expression of the anisotropy states on the Lumley triangle. States include complete isotropy, one dimensional dominance, axi-symmetric states and 2D states.

The upper black line in Figure 6.5 represents a state of two-dimensional turbulence, while the red lateral lines delineate axisymmetric behavior. The axisymmetric line on the negative side of the third invariant suggests an expanding nature also called "disk-like" turbulent state by Simonsen and Krogstad (2005) where one component is of a relative much lower magnitude than the other two. However the axisymmetric curve on positive side of the III invariant is designated as a "rod-like" turbulence (Simonsen and Krogstad, 2005) and dominated by a single component. The point where the two-dimensional boundary line meets the axisymmetric line on

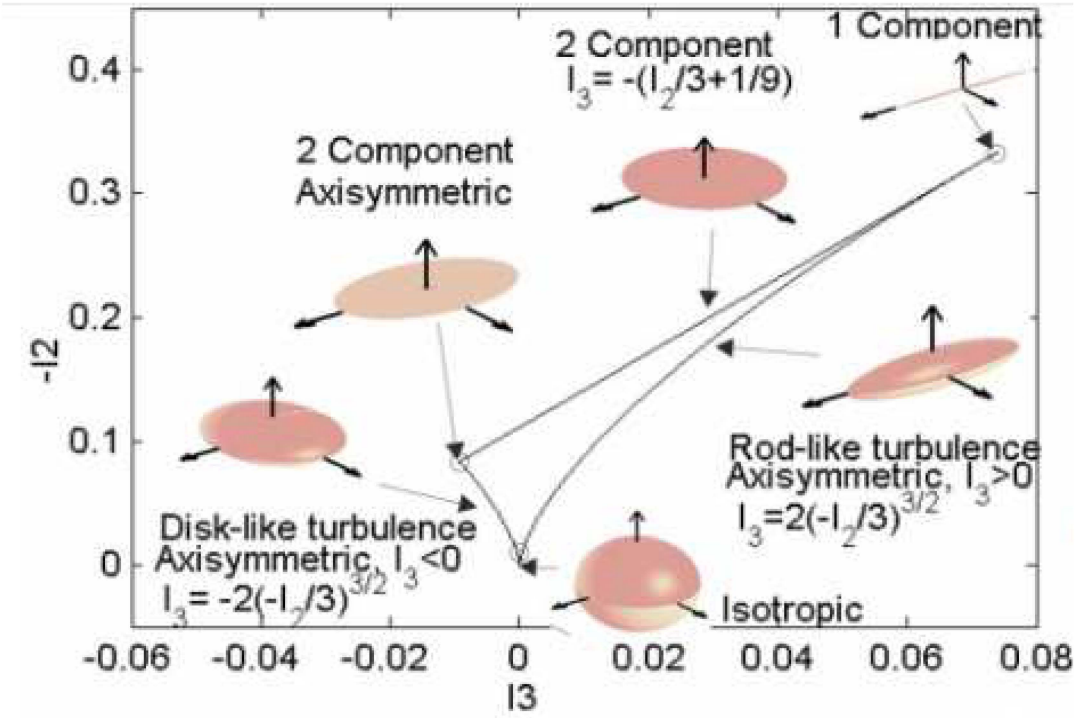

Figure 6.4: Anisotropy invariant map legend from Simonsen and Krogstad (2005) showing the states of turbulence as bound by the Lumley triangle.

the positive III axis signifies complete one dimensional turbulence. The AIM will allow us to do a visual comparison of the changing anisotropy along the sea floor of the domain by plotting every point for the group of line probes per region.

Figure 6.5 shows three anisotropy invariant maps that plot points for all of the line probes per each region of the domain. In order to follow the vertical direction evolution of the anisotropy, points were colored by their vertical position along the water column. In all subplots anisotropy began at its deepest point near the two dimensional turbulence boundary curve. This is due to the impermeability of the wall in its normal direction. This is perfectly seen in anisotropy invariant maps of smooth channels by Ashrafian and Andersson (2006) using data by Moser et al. (1999) in which smooth channel turbulence begins as two dimensional advances to one-dimensional and decays down to isotropy following the rod-like axisymetric line. However, due to the sea bottom irregularity of the domain the wall normal vector will not be aligned perfectly with the vertical direction. Alfredsson et al. (2012) observed a similar behavior when plotting rough channels with a rod like bottom. In the rod roughened boundary, turbulence began as two-dimensional moving towards a rod like turbulence state before decaying to isotropy. Similar results were seen by De Marchis and Napoli (2012) for 2D and 3D irregular roughened surfaces. As the roughness increased the degree of anisotropy decreased while straddling the axisymetric contracting line.

All regions showed isotropic values near the mid values of their respective water column. However the transition from the two dimensional state to isotropy followed a peak towards higher values of anisotropy before decaying back to isotropy. Major deviations between regions occurred in the bottom 10-15 m. Region 3 showed points straddling the right axisymetric line, with coordinates III reaching up to 0.057 and $II = 0.27$, this would suggest higher values of anisotropy than the other 2 regions. Values near the surface at the 0 mark were influenced by the upper slip boundary condition in all three regions such that the upper boundary forces a 2D turbulent state that had to expand from the isotropic state close to mid column. Region 2 and Region 3 showed points located 10-15 m from the sea bottom returning to

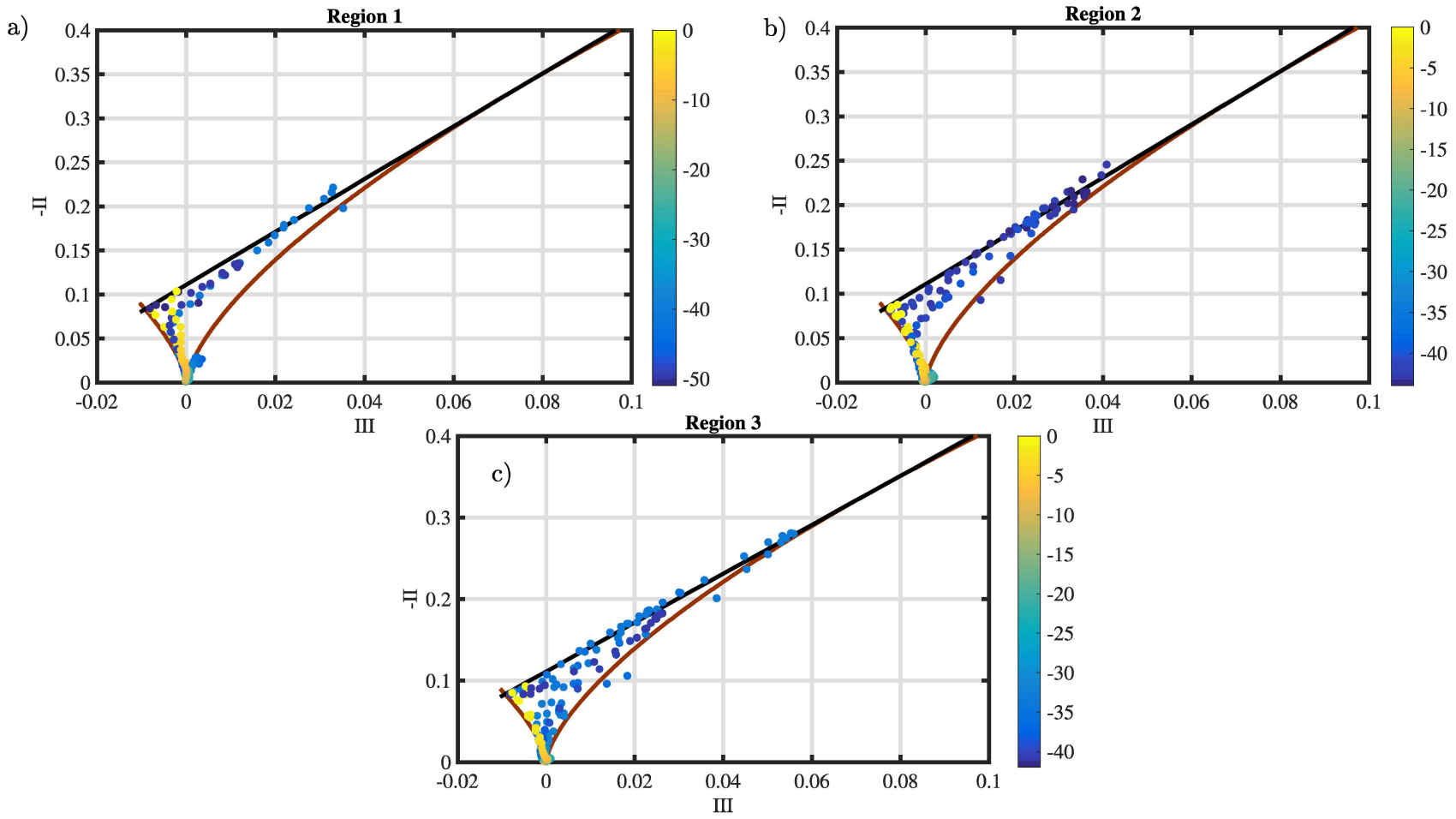

Figure 6.5: Anisotropy invariant map plotting invariants -II by III, for all line probes in the domain fort: a) Region 1 b) Region 2 c) Region 3. Points colored by vertical depth (m). Top solid black line delimits two-dimensional turbulence while red solid lines delimit axisymetric turbulence.

the isotropic values yet closer to contracting axisymmetry as was seen in previous studies that suggested the appearance of rod like hairpin vortices (De Marchis and Napoli, 2012; de Marchis et al., 2010; Alfredsson et al., 2012).

It must be noted that some data points were found just outside of the Lumley triangle, this is most probably due to discretization error during calculation. These points were found to have a similar error when calculating the form parameter, which is expressed by $F = 1 + 27III + 9II$. The maximum error was found to be 1.54% for the form parameter, thus we can assume a similar error which is within acceptable bounds.

The anisotropy invariant map of the 3 regions of our domain helped confirm the anisotropy due to the changing bathymetry. Lower depths in region 3 behaved more akin to a smooth channel than regions 2 and 1. Although the irregular sea bed did decrease anisotropy near the bed in comparison to flat channels and even some previous roughness studies. The presence of contracting anisotropy in areas 10-15 m from the seabed would suggest energy production rich hairpin vortices. It is necessary to look into Reynolds stresses as discrete events and not simply as averaged values to appropriately confirm these vortices due to their transient nature, particularly for the cross component uw responsible for up to 80% of turbulent production.

6.3 Quadrant Analysis

Due to the inherent unpredictability of turbulent flows any analysis of turbulent flow must be of a statistical nature. Quadrant analysis techniques fulfill these objectives as well as lead us into linking the Reynolds stress tensor to coherent structures and discrete events. A quadrant analysis is done for the most important of the cross-component Reynolds stresses $u_i'u_k'$ responsible for the production term $-\overline{u_i'u_j'}\frac{\partial \overline{u_i}}{\partial x_j}$ in the turbulent kinetic energy budget as a result of the wall shear stress at the sea boundary. Quadrant analysis will use an abbreviated nomenclature when referring to the $u_i'u_k'$ component following previous work. Here u' will be the streamwise velocity

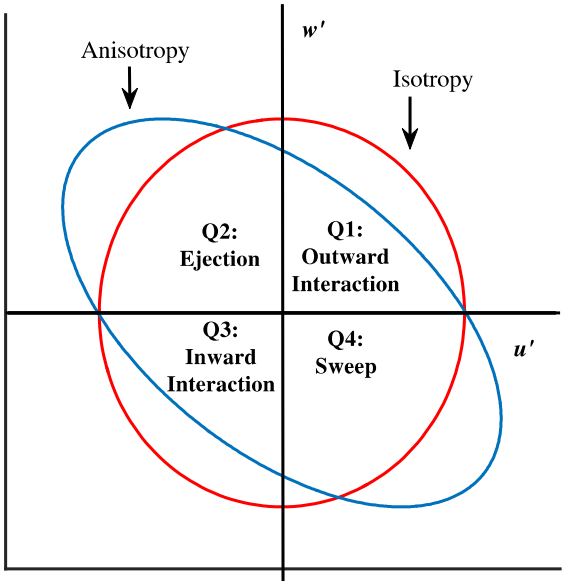

Figure 6.6: Quadrant Analysis Shapes and events of a cartesian mapping of u' and w' events. Red line shows isotropic behaviour, blue shows anisotropic behaviour.

variation, equivalent to u_i', while w' refers to the vertical velocity component. Figure 6.6 shows the mapping of possible locations for $u'w'$ Reynolds stresses.

The negative $-uw$ quadrants 2 and 4 are called bursting quadrants, also named ejection and sweep quadrants respectively and are responsible for the majority of the turbulent kinetic energy production (Kim et al., 1971). Positive quadrants Q1 and Q3 are simply called outward and inward interactions due to their directions out and into the flow. With a sufficient number of discrete points a shape emerges on the quadrant plot that can demonstrate the structural behaviour of the turbulent flow for the points plotted. Figure 6.6 shows a red outline that would be present during isotropic behaviour where both the streamwise u component and the vertical w component are of equal magnitude. During isotropic behaviour this outline becomes skewed towards a component showing a higher importance over the other. In order to filter uw events by their magnitude we define regions delimited by constant $|uw|$ curves. The delimited areas are called holes by Lu and Willmarth (1973) in their quadrant analysis formulation. The mathematical definition of the hole region is as

follows:

$$H = \frac{|u'w'|}{|u''w''|} \tag{6.4}$$

Here the u'' and w'' represent root-mean-square values, and aid as a normalization agent when comparing hole values.

A conditioned filtering was applied to all discrete samples taken during the simulation. This conditioned sampling was done to sort every discrete point into a hole value H and a quadrant number $i = 1, 2, 3, 4$. This filtering is shown in the following equation:

$$I_{i,H,t} = \begin{cases} 1, & \text{if } (u'w')\text{is in quadrant i \& } |u'w'| \geq Hu''w'' \\ 0, & \text{otherwise} \end{cases} \tag{6.5}$$

$I_{I,H,t}$ is our filtering function which places events in: $i = 1$ for $u > 0, w > 0$, $i = 2$ for $u < 0, w > 0$, $i = 3$ for $u < 0, w < 0$ and finally $i = 4$ for $u > 0, w < 0$.

An averaged value $S_{i,H}$ is then taken for each hole and quadrant to analyse the averaged fractional contribution of the values per quadrant outside of the hole value. This will give us an idea of the importance of each quadrant to the total $u'w'$ Reynolds stress. The mathematical formulation is as follows:

$$S_{i,H} = \frac{1}{T}\int_0^T u(x,z,t)w(x,z,t)I_{i,H,t}(u,w)dt \tag{6.6}$$

Here T is the total sampling period and dt is the sampling period at 5 Hz. It follows that the sum of all quadrants at a hole size of 0 would be equal to 1 since all fractional contributions should be accounted for as in equation 6.7.

$$\sum_{i=1}^{4} S_{i,0} = 1 \tag{6.7}$$

The purpose of the hole size study is to visualize the probability of high magnitude events while placing them within their appropriate quadrants. Hole size contours provide reference points and contextualization of their non-dimensional magnitude. This answers the question of how probable and how strong events are.

Figure 6.7 shows nine joint probability density contours calculated from instantaneous points sampled at 5 Hz for the streamwise velocity variation u' and vertical

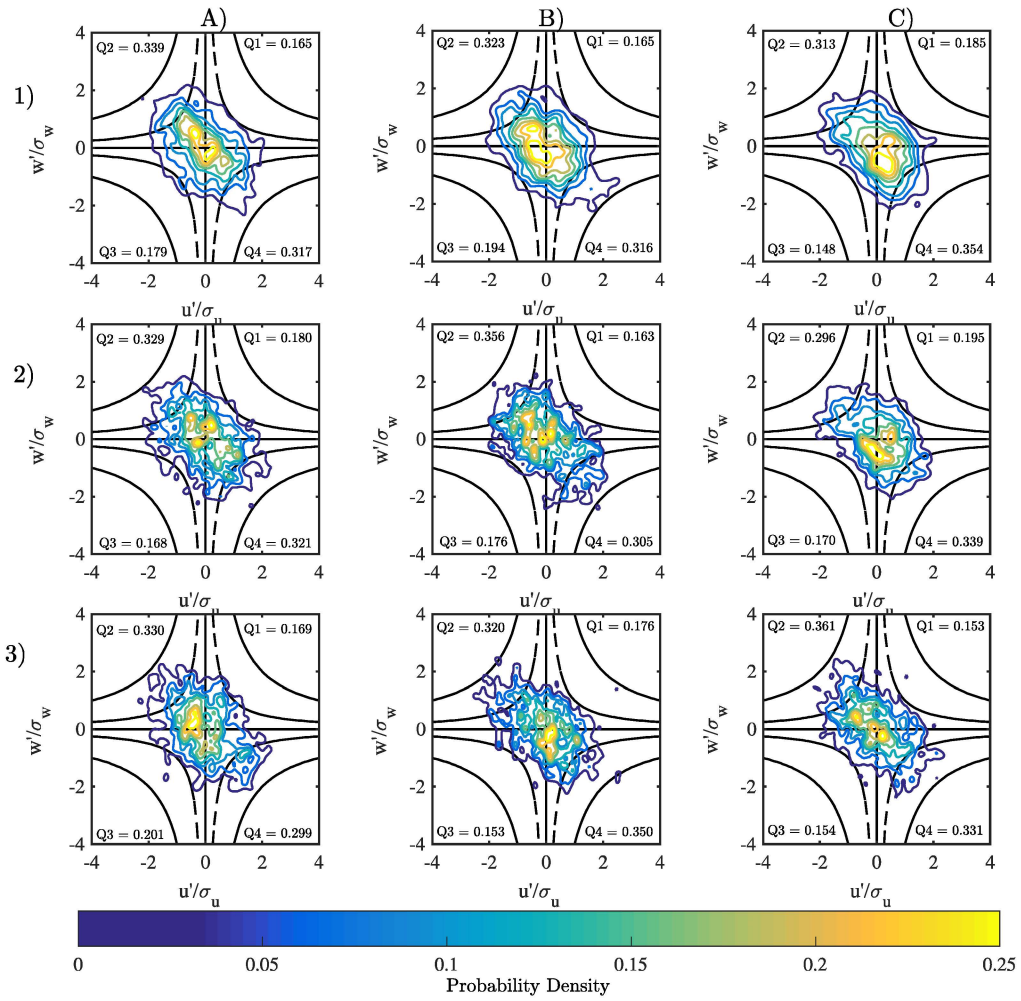

Figure 6.7: Quadrant Analysis contours coloured by their probability density function within 2 Hole (H) size=1 for the dashed and dotted line and H=4 for solid line. Legend in each quadrant refers to the contribution of each event to the totals Reynolds stress component $\overline{uw}$. Both the streamwise component u & vertical component w have been normalized. From left to right (A,B,C) are plots showing points at line probes for 3 regions (R1 left column, R2 middle column, R3 right column), from top to bottom (1,2,3) are plots at vertical positions of 10% of the water column, 20% and the bottom most row is at 50% of the water column.

velocity variation w' normalized by their respective standard deviation σ. Figure 6.7 shows points located at 10, 20 & 50 % of the water column for representative line probes in regions 1-3. Columns A, B and C correspond to R1, R2 and R3 respectively while rows 1-3 correspond to the vertical locations from 10% in row 1 to 50% in row 3. Constant Reynolds stress $|u'w'| = 1{,}4$ are plotted as dashed and straight lines to best contextualize the magnitude of the contours. The sum of the total probability for each quadrant is shown in each subplot.

All subplots showed a great deal of anisotropy with a particular dominance of the bursting quadrants Q2 and Q4. The sum of probabilities for bursting quadrants remained semi constant for plots in column A (R1) at 0.656 for the 10 and 20% mark dipping to 0.63 at 50% of the water column. Although the sum of the bursting quadrants showed small variation it is clear that the probability density distribution spread to higher magnitude hole values, suggesting high magnitude bursts reaching up to $|u'w'| = 4$ for the 20 and 50% positions whereas, the probability contours at the 10% mark showed high probability values near $|u'w'| = 0$. All vertical positions showed a slight dominance of Q2 events over Q4 by a maximum of 3%. Bursting events contributed the majority of the contribution to the $-\overline{u'w'}$ Reynolds stress component and increased as the water column positions ascended. Locations 10% and 20% of the water column were unbalanced in their bursting quadrants, with a higher tendency of sweeping motions yet the erupting quadrant showed probability contours at higher magnitudes than in region 1. For the 50% location of the water column bursting events contributed up to 0.67 of the $\overline{u'w'}$ stress and had dispersed high magnitude event contours.

Probability contours for all positions in region 3 were skewed for positive u' values and the highest erupting quadrants of all regions up to 0.354 of the $\overline{u'w'}$. Region 3 followed a similar trend of region 2 where the position in the water column drove a higher probability density of bursting events as well as higher magnitude events. The maximum bursting contribution was at 50% at 0.7 total probability.

The probability density contours showed a high dependency on the vertical location with higher values at the 50% position of the water column for bursting events.

Sweep and eruption events were balanced for region 1 while Q2 and Q4 were seen more in region 2 and 3 respectively suggesting an influence of the region location on bursting probabilities. All plots showed Q1 and Q3 confined to a hole size of H=1 along the water column, suggesting a continuous anisotropic flow. Total Reynolds stress contributions from each quadrant were shown to not always coincide with the total amount of discrete samples per quadrant due to certain quadrants having low probability high magnitude events. More statistical analysis is required to have a full understanding of quadrant behaviour, this leads us to analyze the contribution per hole size in figure 6.8.

6.3.1 Bursting Event Filtered Spatial Distribution and Decay

Figure 6.8 shows nine subplots at the same spatial coordinates than in figure 6.7 showing the fractional contribution of all $u'w'$ events as confined by hole sizes H=1-5 for each quadrant. All quadrant contributions eventually converge to 0 as the H becomes sufficiently large. Inwards and outward quadrants were balanced in their contribution with the exception of region 2 at the bottom most 10% and disappeared in Reynolds stress contribution for hole sizes above H=1 with the exception of the bottom 10% of the water column in all regions. Ejections had a larger contribution across all of the holes for regions 1 and 2 for the two bottom most points. Region 3 showed a clear difference between Q2 and Q4 contributions with Q2 decreasing its highest contribution at H=0 from 0.78 at the bottom 10% mark down to 0.6 while Q4 remains semi-constant as it rises in the water column.

Line probe regional location had an effect on the balance between Q2 and Q4 events as well as the higher contribution for H=0. Region 3 contributions of bursting quadrants for large hole sizes $H > 4$ remained relatively high compared to other regions where they supplied less than 0.1 of the contribution to the averaged $\overline{u'w'}$. All regions demonstrated a sharp decay in hole size contribution for values above H=2.5.

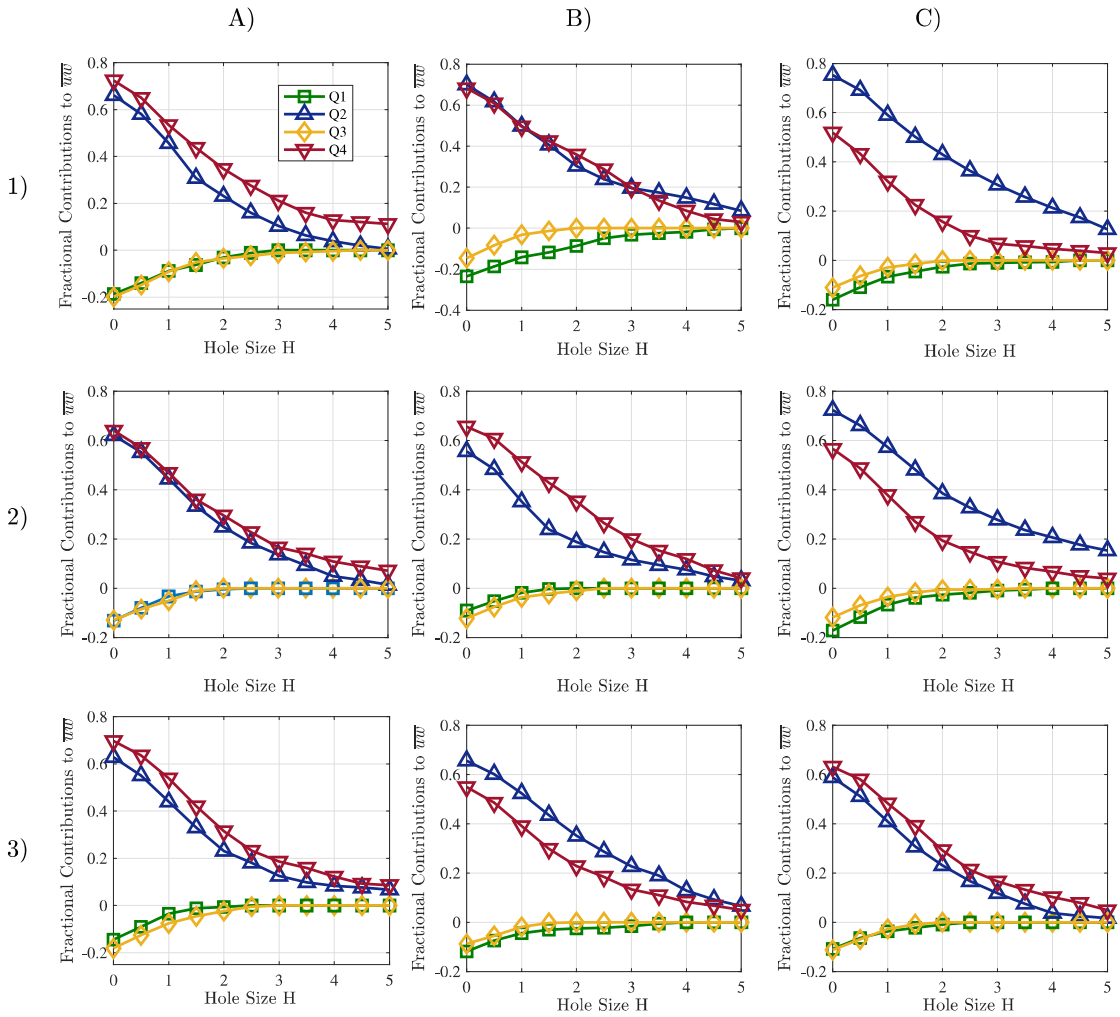

Figure 6.8: Fractional contribution for each quadrant to the Reynolds stress component $\overline{uw}$ per Hole Size H. Q1 is shown in square green markers, blue triangles represent Q2, yellow circles mark Q3 and Q4 is shown by red inverted triangles. From left to right (A,B,C) are plots showing points at line probes for 3 regions (R1 left column, R2 middle column, R3 right column), from top to bottom (1,2,3) are plots at vertical positions of 10% of the water column, 20% and the bottom most row is at 50% of the water column.

6.3.2 Temporal Lifespan of Bursting events

It is important to understand not only the probability of these events but the average duration as well. This holds especially true for high magnitude events, in order to best understand their energy density and fatigue effect on energy extracting devices and other subsea structures. In order to find the average value of the events $T_{i,H}$, the $u'w'$ discrete sampled values were filtered and sorted into their respective quadrants i and hole magnitude H. This method of time filtering by hole sizes was first introduced by Lu and Willmarth (1973) and in explained in the following equations.

$$\overline{T_{i,H}} = \frac{1}{T}\int_0^T S_{i,H,t}dt \tag{6.8}$$

This gives us an average time in seconds for each time burst by summing up every event that occurs outside the limits of a particular hole magnitude and a previously filtered quadrant. Figure 6.9 shows the average duration for the bursting events Q2 and Q4 against their hole size magnitudes H=1-5 for the previously mentioned points in figures 6.7 and 6.8.

It is to be noted that high magnitude events with hole sizes H=4 and H=5 may have high average duration yet occurred with a much lower frequency than other hole sizes. Thus, in some cases they only occurred once during the entire sampling period and their average duration time requires a higher sampling time for stronger statistical power. Every region line probe showed a tendency of decreasing time duration for both quadrant events, as the hole size increased due to extreme events being difficult to sustain for larger period of time. Event duration was highly dependent on vertical position location. Higher averaged periods occurred at the 50% mark and decreased in life spans in conjunction with the vertical position.

Region 1's bursting events showed slightly higher life time cycles than its sweeping event counterpart. Values of sweeping events for H=5 show high values up to 4s life cycle, however as previously mentioned this is due to low frequency events. Region 3 had a noticeable lower lifetime cycle than the other regions at the 20 and 10% bottom water column mark yet maintaining a life cycle of 3-2 seconds until the highest hole size. Highest lifetime cycles were seen in region 3 as well yet decrease

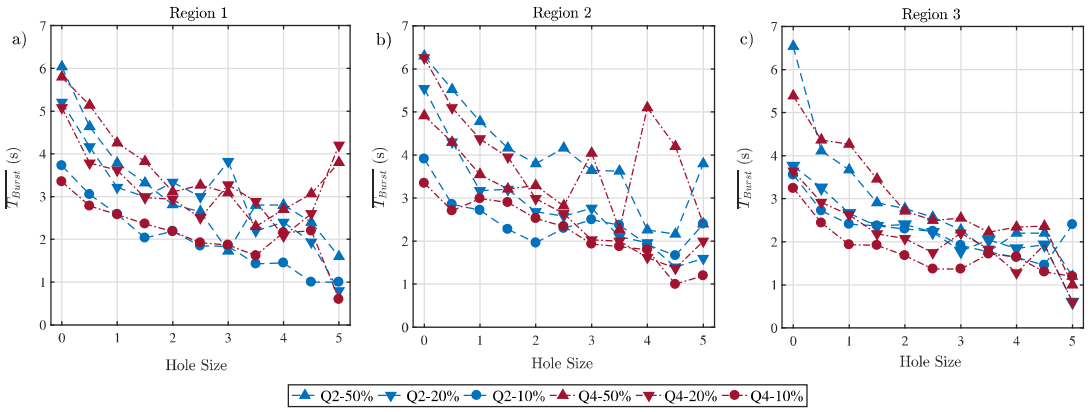

Figure 6.9: Average duration of each bursting event Q2 and Q4 in seconds plotted against the magnitude of the bursting event as delimited by a Hole Size. Point locations are given in figure 6.7. Sweeping events (Q2) are colored in blue while bursting events (Q4) are colored in red. From left to right subplots show Regions 1-3. Upper triangle marks shown bursts at the 50% mark of the water column while lower triangle are at the 20% location, circles represent the bottom 10% of the water column.

more sharply than in region 1 and 2. All life cycles for every quadrant and vertical position remained within a range of 2 to 4 seconds except hole sizes below H=1. This allows us to give a characteristic time scale to bursting events while providing time scales for the more extreme events.

Figure 6.10 aids in visualizing the temporal duration of these events by plotting the vertical axis of the domain against a 10 minute sub-sampling period of red and blue colored Reynolds stress contours for sweep and bursting events respectively. This visual aid was done to representative line probes for each region at $x_{R1} = 30(m)$, $x_{R2} = 185(m)$, $x_{R3} = 850(m)$ (sub-indices indicate the region). While our previous temporal analysis allowed us to contextualize life time cycles in an averaged form with hole sizes, it would be convenient to also present the filtered data in terms of absolute Reynolds stress.

Both higher Reynolds stresses as well as larger structures are present in all three regions near the mid water column yet it is seems apparent that they surge from the seabed at smaller magnitudes. Ejections were shown to be more frequent than

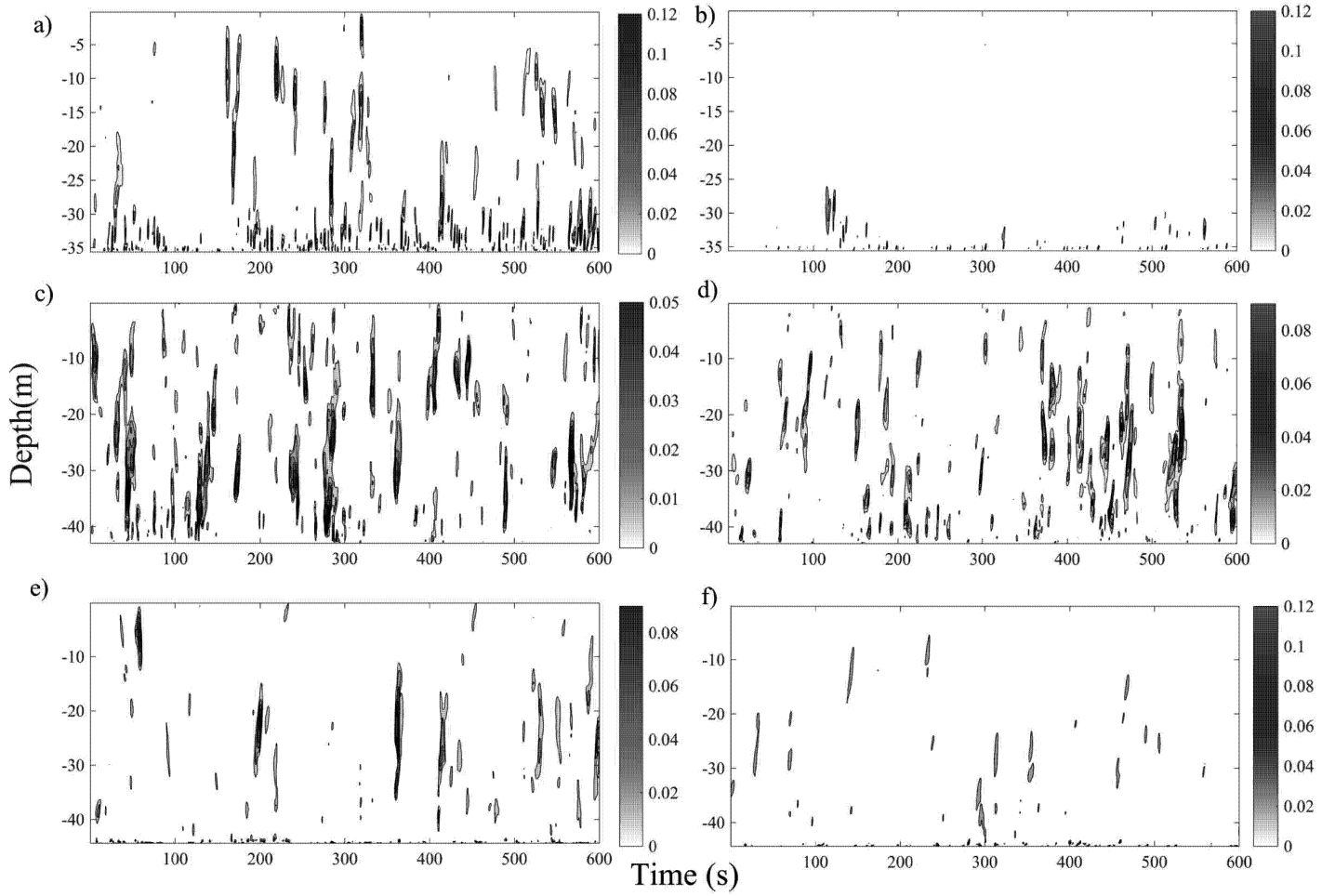

Figure 6.10: Ejection(Q2) are shown on the left column with a red color map while sweeps are shown on the right column with a blue color map (Q4).All plots are filtered colored by instantaneous $|uw|(m^2/s^2)$.(a,b) show a line probe in R3 for a period of 10 minutes plotted against the water column. (c,d) refers to R2 and (e,f) to R1. All line probes are located mid-span at $x_{R1} = 30(m)$, $x_{R2} = 185(m)$, $x_{R3} = 850(m)$. Colormap corresponds to Reynold stress magnitudes.

ejections for all regions yet this unbalance was only skewed more prominently in region 1. Average absolute value for the $\overline{u'w'}$ Reynolds stress across the domain was equal to 0.004 (m^2/s^2). Contours in figure 6.10 show events with Reynolds stress magnitudes 5-30 times the average $\overline{u'w'}$ stress component simultaneously throughout large portions of the water column. Region 2, although the region with more frequent and longer sweeps and ejections showed a smaller magnitude than the other regions. Region 3 noticeably held several ejections with a sustained high magnitude of Reynolds stress. It is thought that the higher frequency of ejecting events is due to the sea bed floor converging as the domain develops in the streamwise direction, creating a ramp like effect pushing the flow upwards.

6.3.3 Higher Moment Statistical Analysis of bursting events

Further statistical understanding of the uw events was complimented by the third and fourth order moments to understand the dominant sign of the discrete uw events as well as a measure of the extreme nature that would otherwise be lost in averaged Reynolds stress values. The third order moment, also referred to as skewness is defined in the following equation:

$$S_{uw} = \frac{\overline{(u'w')^3}}{\overline{(u'w')^2}^{3/2}} \tag{6.9}$$

Figure 6.11 reinforces the aforementioned behaviour of lines 1 and 2 as part of the start-up region of the domain. Higher statistical moments take a longer period of time and start-up length to show converging behavior within the domain. However, lines 3 and 4 as well as regions 2 and 3 show a negative skewness for the $u'w'$ component up to the bottom 20% mark. After this region skewness remains flat independently of the region. Each line probe showed a peak of positive skewness at the wall which quickly switched to negative values near the wall before decaying to 0. Lines 3 and 4 of region 1 and region 2 showed similar levels of negative skewness at the near wall peak. Region 3 exhibited parallel negative skewness yet at higher peak values reaching a maximum of -3 for line 12.

The fourth order moment, also called Kurtosis or flatness factor is calculated by:

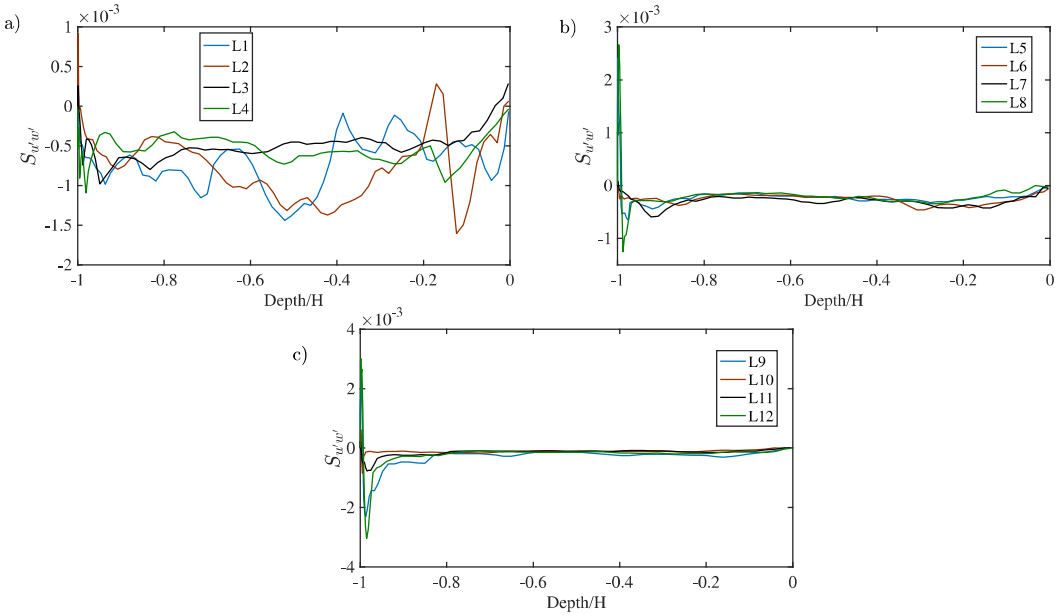

Figure 6.11: Skewness S_{uw} depth profiles of uw Reynolds stress. Line probes shown belong to : a) Region 1, b) Region 2, c) Region 3

$$K_{uw} = \frac{\overline{(u'w')^4}}{\overline{(u'w')^2}^2} \tag{6.10}$$

The Kurtosis value is used to contextualize the importance of extreme events in the tails of the distribution as they deviate from the averaged behaviour. Milne et al. (2017) reported values between 9 and 12 at the Sound of Islay for a point measurement 5 meters above the seabed. Values of kurtosis above 5 are considered strong deviations from normal behaviour. All regions exhibited peaks of high kurtosis and thus a higher frequency of extreme $u'w'$ events close to the wall. Region 3 continued being a region of strong statistical behaviour exhibiting strong leptokurtic behaviour for its line probes up to half the water column. Although average values of the $\overline{u'w}'$ stress show low values if the depth profile shows highly kurtocized behaviors extreme events could be of higher importance for fatigue loading.

The statistical nature of the analyzed points throughout the domain suggest a more in depth analysis of Reynolds stress discrete events may be required. This is apparent when realizing the role $u'w'$ stresses play in turbulent production, events and their interaction with structures near the seabed. Rare yet, turbulent kinetic rich

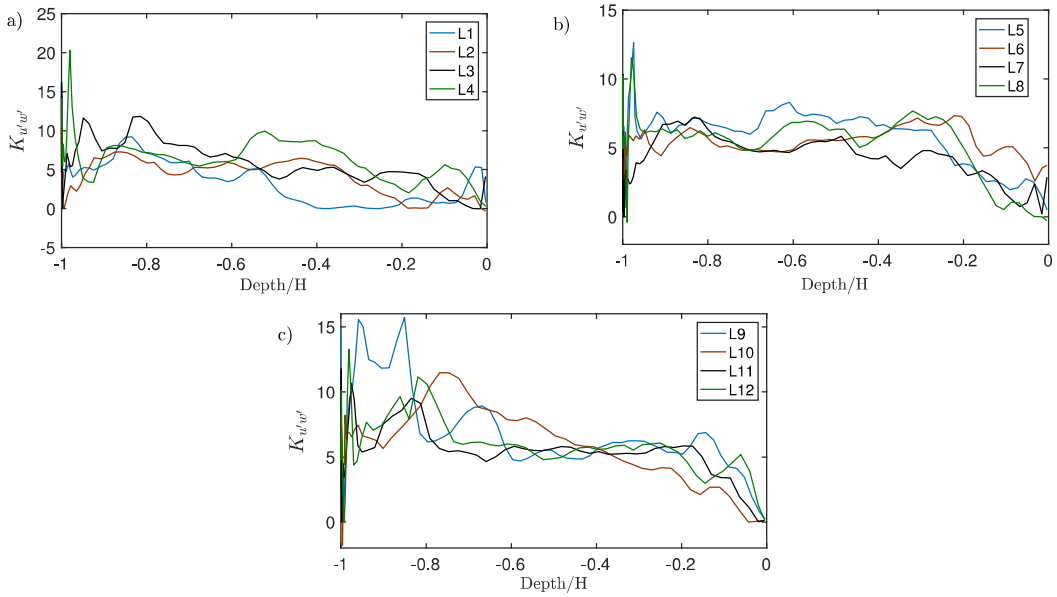

Figure 6.12: Kurtosis K_{uw} depth profiles of uw Reynolds stress. Line probes shown belong to : a) Region 1, b) Region 2, c) Region 3

bursts play a more prominent role in the turbulent flow that would have otherwise been ignored in averaged quantities or if a normal distribution assumptions. Both the magnitude, probability and life time of these events make them a topic of further analysis for offshore hydrodynamic force analysis.

6.4 Coherent Structure visualization

The use of quadrant analysis and anisotropy invariant maps has allowed us to conclude the existence of bursting and sweeping events in the form of long rod like structures also called hairpin vortices, originating near the wall reaching half the water column. Visualization techniques were utilized to find and identify these vortical structures within the CFD domain in a three-dimensional manner.

Figure 6.13 shows a sub-domain sampled at an instant moment in time at $x = (100 - 250)m$ and $y = (160 - 200)m$, the figure shows an iso-surface of a Q criterion which has been conditionally filtered to show quadrant events. Red colored portions of the domain are shown to be Q4 events(sweeps), blue co-responds to Q2 events

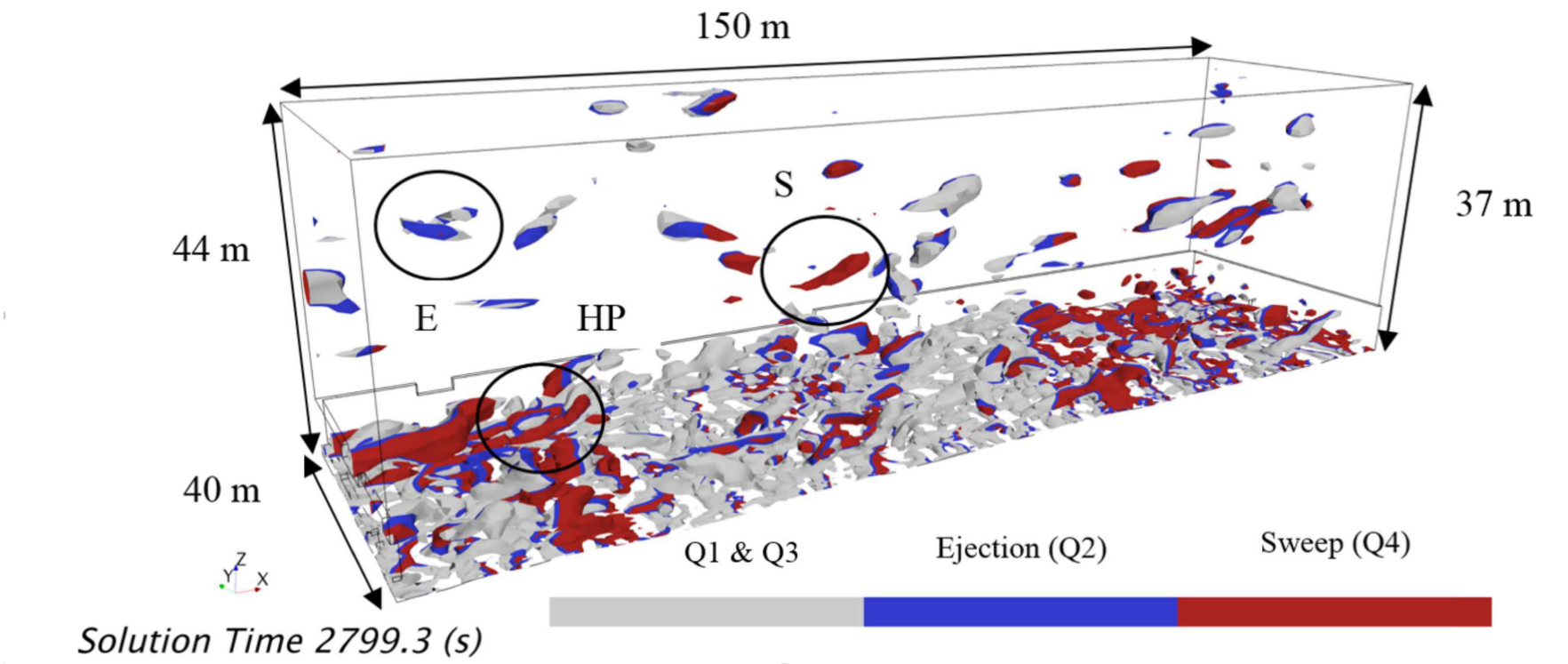

Figure 6.13: Instantaneous Isosurface by Q criterion of a subdomain covering x x y = 150x40 m. Colored by conditional filtering to show Q2 events in blue and Q4 in red, all other events colored in grey. S refers to sweep events, E to ejection and HP to hairpin vortex.

(ejections) and the rest of the inward interaction quadrants are shown in gray. The Q criterion first established by Jeong and Hussain (1995), shows vortical structures and is developed in the following equations.

$$Q = \frac{\Omega^2 - S^2}{2} \tag{6.11}$$

Here the Q-criterion is defined as the vorticity Ω independent from the shear strain S. Where the $S = \frac{J+J^T}{2}$ and $\Omega = \frac{J-J^T}{2}$ vectors are defined by Jeong and Hussain (1995) as the symmetric and anti symmetric components of the Jacobian tensor of the velocity $J = \nabla u$.

Figure 6.13 highlights three clear structures, structures E and S show an ejection and a sweep that are high above the bed yet have a large enough size (length=16m) reinforcing the idea of how high up the water column some bursts can go. The hairpin structure HP is seen near the seabed as a connection between an ejection and a sweep. The sub-domain shown also reinforces the notion set by Adrian (2007) that these hairpin vortices emerge as packets of multiple vortices occurring simultaneously near the seabed.

The coherent structure tagged as HP refers to hairpin vortices, Adrian (2007) comments on the origin of these hairpin vortices as a product of the turbulent Q2 and Q4 events with a dominance on sweeping events, in conjunction with the ejection for boundary layer-like flows. This can be best seen in the highlighted hairpin vortex in figure 6.13. Adrian (2007) also mentions the existence of these coherent structures at a higher strength and density near the wall as a mechanism of turbulent production, this is supported by other authors Roussinova et al. (2008, 2009) which found the creation of hairpin vortices and turbulent events to be more evenly distributed at shallow flow compared to deeper flow in a channel.

6.5 Chapter discussion

Analysis shown in the present chapter is based on data from a Large Eddy Simulation of a 2.1 m/s flood tide at the Fall of Warness EMEC site in Orkney, Scot-

land. Boundary conditions were set based on site measurements and the sea bottom bathymetry. Realistic site bathymetry was used to differentiate from past tidal energy modelling efforts which used smooth wall boundary conditions as well as to compare to other irregular surface turbulence structure studies.

Data from the simulation was used to study the turbulent structure and higher moment statistical quadrant analysis of the temporal and spatial lifetimes of bursting events throughout the domain. Data points covering the water column were taken for several locations throughout the changing maximum water depth in the streamwise direction giving a fuller three-dimensional analysis of the flow. Turbulent structure. as measured by the anisotropy invariant map and the anisotropy tensor B_{ij} showed a rapid increase in isotropy in comparison to smooth channels and in line with 3D roughened surface studies (De Marchis and Napoli, 2012), in particular with accelerating boundary layer studies (Piomelli et al., 2002). Piomellis accelerating boundary layer supported this studys findings of decreasing anisotropy, and coherent structures in accelerating regions. Isotropy was mapped to vertical positions near the mid water column, with showings of axisymetrical "rod like" elongated turbulence in the bottom 5-10 m from the seabed growing from a two-dimensional state at the bottom boundary. Higher velocity areas of the domain had maximum anisotropy levels but quickly returned to isotropy.

A changing turbulence structure in the domain is linked to a spatial varying $-u'w'$ Reynolds Stress quadrant distribution. Ejection and sweeping events showed an asymmetry in their distribution that was strongly seen in the bottom 20% of the water column, this is supported by Milnes analysis at the Sound of Islay (Milne et al., 2017) in which he calls this a strong intermittent area for extreme events at the same portion of the water column. This is supported by third and fourth order moments of the $-u'w'$ component. Second order moments (Reynolds Stresses) may show some similarity to smooth channels, yet for the suggested intermittent area extreme events occur with a sufficient frequency, energy and lifetime to be of interest for fatigue design, scouring and other engineering purposes previously not covered by smooth wall tidal converter simulations. Extreme events shown at the

midway point of the water column were still present showing how turbulent mixing may reach above the intermittent area, this was well supported by the high kurtosis values above the vertical mid-point.

Ejections were more energetic than bursting events in accelerating regions if less frequent due to a ramping effect pushing flow up. Lifespans of events show their fleeting nature which may not be present in surveys after flow time averaging processing yet, are within the operating frequencies of energy extracting devices and thus relevant to their performance and structural design. These high energy turbulent events are strongly connected to coherent structures which can be visually associated to hairpin vortex packages which have been previously related to surface roughness by Castro et al. (2013) and supported by the AIM for points near the wall. Their lengths are of sufficient size in comparison to the water column to be of engineering significance. Results from this analysis show the effect bathymetrical irregularity can affect Reynolds stress distribution and dissipation. These results imply unique local turbulence characteristic dependency near the sea bed floor, particularly for rich turbulent kinetic energy coherent structure production. The use of high resolution spatial and temporal models allow for a deeper statistical analysis of transient energy rich events. Deeper understanding of these events and their characteristics will be of use to tidal energy development as well as a variety of offshore marine engineering applications when designing for fatigue, vibrations, sediment transport etc.

CHAPTER 7

BATHYMETRY EFFECT ON TURBULENCE OF AN EBB TIDE

7.1 Introduction

The chapter aims at bringing together the concepts and data from past chapters in an aim to describe the semi-diurnal tidal components and the relation between them. Chapter 1 introduced the idea that ocean currents change in magnitude and direction depending on the phase of the tidal component. Chapters 4 and 5 have presented results and analysis of a flood tide. Tidal currents are composed out of not only flood tides but also of complimentary ebb tides in a major tidal period 12.42 hours. In the case of the Fall of Warness, the ebb tide reverses the direction of the flow, changing its heading from southeast to northwest headings. The bathymetry during the ebb tide expands the cross-sectional areas as the streamwise direction advances decelerating the flow.

A full turbulent parameter and structure analysis must be taken into account for this behavior for a more complete characterization of the turbulent nature of the Fall of Warness. The chapter will aim to answer one of the questions initially

proposed in this thesis: "What role do the ebb and flood tides, and thus direction of the flow, play on the turbulent nature of the flow? "

This is done by presenting the results of the large eddy simulation that reverses the flow direction compared to the work done in the previous two chapters. The chapter will begin with a proper validation and comparison to the corresponding site measurements for an ebb tide at a 2.1 m/s reference velocity at hub location. The velocity was chosen to compare ebb and flood simulations under the same turbulent conditions only changing the direction of the flow.Flow direction was considered to be 180 degrees opposite between flood and ebb. Seller and Sutherland (2015) found a +/- 5 °mean flow variation from the mean flow direction. This deviation is valid for both flood and ebb at velocities 2 m/s or above. Velocities below 0.8 m/s showed 30 and 15 degree deviations for flood and ebb tide respectively. However, these velocities are not relevant for the speeds analyzed.

Turbulence parameter and structural results are also presented to obtain further understanding of the turbulent character of the ebb flow, including quadrant analysis, (previously introduced in chapter 5) and an exploration of the turbulent kinetic energy behaviour linked to the seabed stress of a decelerating flow.

Ebb site measurements showed a level of asymmetry in relation to its flood counterpart for mean velocity and turbulence parameters along the water column. It is of great interest to see to which effect, if any, the bathymetry plays in explaining the asymmetry between tides. Comparisons will be made between turbulent parameters of the ebb and flood tides, in addition to a base case of a flat channel with no expanding/contracting bathymetry condition, in an attempt to answer the research question.

7.2 Ebb Simulation

Results presented in this chapter were extracted from a simulation run under the same conditions as the flood simulation from the previous chapters. The only, yet significant change, was the change in direction of the flow by the switching of the

velocity inlet and pressure outlet boundary conditions at locations $x_{outlet} = -320m$ and $x_{inlet} = 935m$, seen in figure 4.6.

Inflow data was input into the domain to establish a mirror view of the tidal flow by setting the velocity at hub height at the center of the domain to a $u_{ref} = 2.1m/s$; this was done to compare flood and ebb tides at the same reference velocity. The ebb simulation used the same mesh and time discretization ($\Delta_t = 0.2s,\ T = 30min,\ Ns = 9000$) conditions as in the verification process discussed in chapter 3 and thus will not be elaborated upon in matters of numerical quality. Data presented was taken at the same locations presented in table 5.3. It is however, paramount to continue the necessary validation of the simulation results to site measurements of a $2.1m/s$ ebb tide.

7.2.1 Validation

Figure 7.1 shows a comparison of a) the mean streamwise velocity depth profile, b) turbulence intensity and c) turbulent kinetic density for ebb simulation and site measurement data, for the purpose of model validation. Mean streamwise velocity depth profile from the ebb simulation was compared to a 1/7 power law of a theoretical boundary layer as well as the site measurements taken from an ADCP from the ReDAPT data. Sellar et al. (2018) mentions the disagreement between the theoretical power law model and site data for ebb tides, due to a flow retardation from the mid-depth to the surface. Overall fit of the simulated mean velocity depth profile with the site data was calculated to be within an error of 5.9% when comparing euclidean vector norms $||x||_2 = \sqrt{\sum_{i=1}^{n} |x|^2}$ Creech et al. (2017) , where $||x||_2$ is calculated for all the points at vertical locations above the first measurement taken in the site measurements.

Divergence from the power law velocity model impacts the turbulence intensity and TKE density depth profiles as well. Simulation and site turbulence intensity profiles held similar depth profiles, however, the bulge located in the first 10 m from the seabed was overestimated by the model by 31.8%. The simulation gave the maximum value (note: at a location approximately 5m from the seabed) of $TI = 19.9\%$,

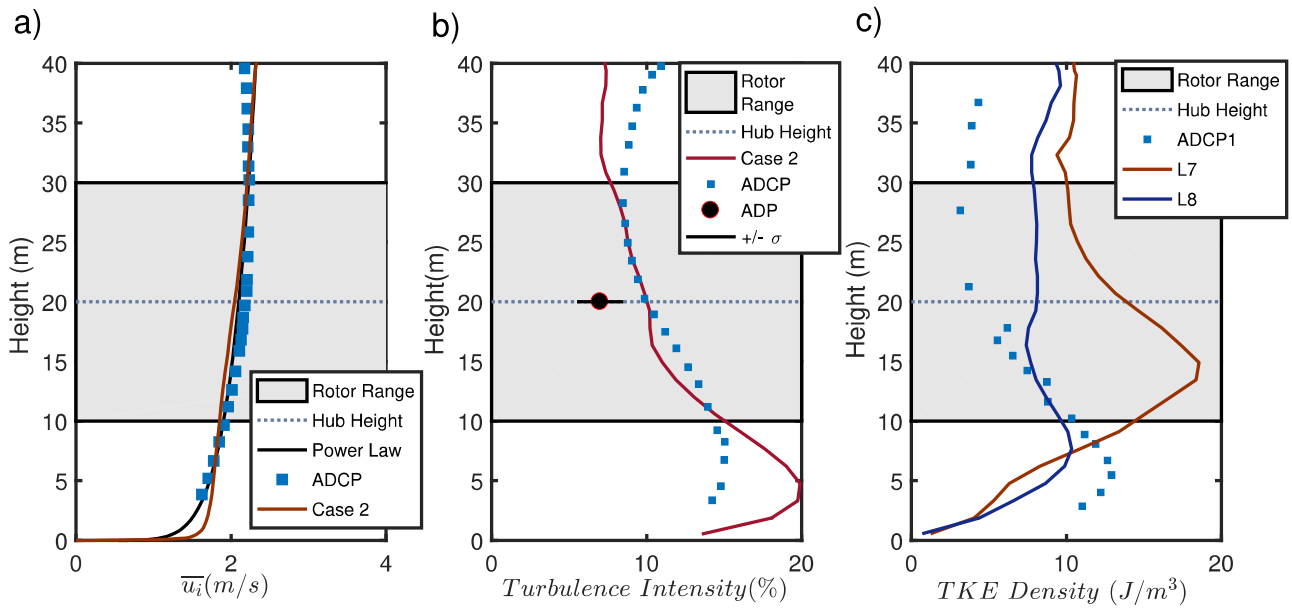

Figure 7.1: a) Velocity (m/s) b), Turbulence Intensity (%) c) and TKE density (J/m^3) Depth Profile Comparisons between simulation data and site measurements. Grey area corresponds to the rotor range for all sub-figures as well as a dotted blue line for the hub height. Solid red line indicates simulation data taken at the midpoint of the domain for case 2. ADCP markers are shown in blue squares and are the result of ensemble averaged profiles from both ADCPs. a) shows a theoretical power law boundary layer with simulation and test data b) includes ADP single point measurement with a $\pm\sigma$ standard deviation range in a solid black line with median value in a black circle c) Shows TKE density lines at L7 and L8 compared to ADCP at the approximate same location.

in contrast with the data measurement of $TI = 15.1\%$. TI measurements at hub height, between the ADCP and simulation data matched at 9.9%. TKE density profiles held a higher disagreement than in flood tide. Site measurements were cleared of very strong outlier points due to their extremely high magnitude ($\approx 160\ J/m^3$) in the upper half of the water column as per suggested by the provider of test data due to unrealistic value as a probable result of device noise and data processing. . Site measurements held a higher TKE density at the previously mentioned bulge seen in the TI profile, equal to 12 J/m^3, which was 16.67% higher than simulation data. Simulation data maintained higher TKE density at points above the bulge while the site measurements showed a higher dissipation not matched by the simulation.

Validation of velocity and turbulent parameters calculated different error measurements for the main turbulence parameters than flood simulations. While velocity and turbulence intensity profiles held a closer fit to the site measurements, the TKE density held less agreement than flood tides to site measurements. The highest error was in locations close to the maximum turbulent depth profile bulge, this would suggest disagreements were more in line with underestimation of the simulation when capturing the turbulent energy content and dissipation of the flow. The modelling component of the LES spectrum may be a source of underestimation. Yet, it is important to stress the role, already mentioned during flood tide, that other features play in turbulence generation. Sellar and Sutherland (2016) and Sellar et al. (2018) mentioned the role that eddies created from nearby islands during ebb tide play in turbulence parameters. Both simulation and site measurements showed an asymmetry in velocity and turbulence parameters from the flood tide that will be analysed further. This is carried out aiming to characterize turbulence parameters both from the ebb flow within a context of the entire tidal cycle and idealized flat bottom flows.

7.2.2 Mean velocity profiles

Analysis of the turbulence parameters should begin with an understanding of the mean velocity profiles of the present simulation as context for the turbulent fluctu-

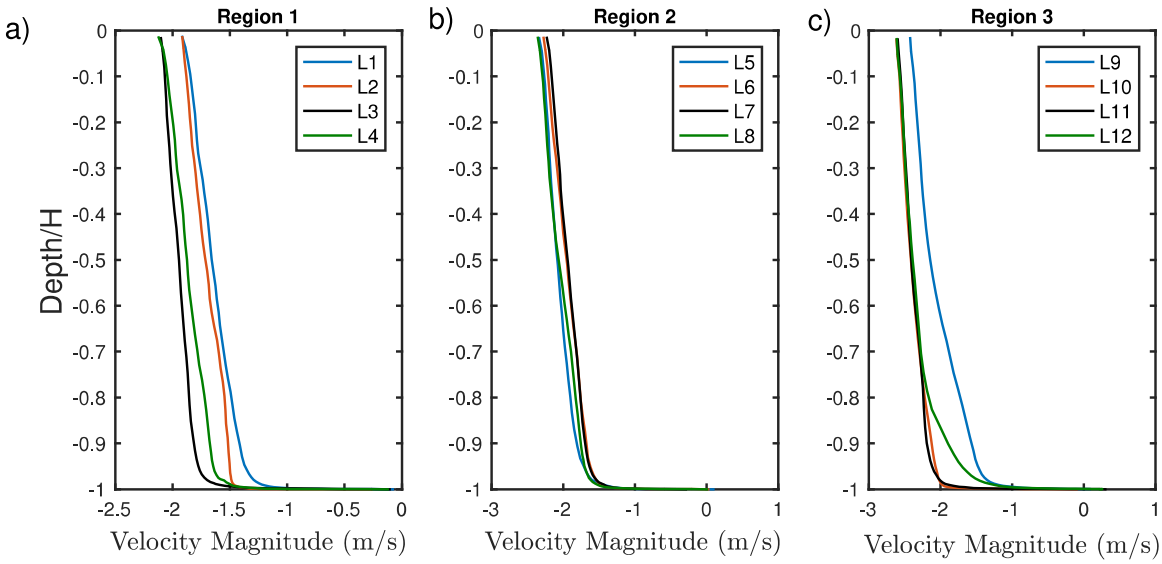

Figure 7.2: Averaged velocity magnitudes plotted along the water column: From left to right, a) Line probes in region 1 b) Line Probes in region 2 c) Line probes in region 3. The vertical axis in all subplots have height normalized by local depth. For location of each line probe refer to tables 1-3. Profile magnitude sign has been changed to emphasize the change in direction compared to flood flow.

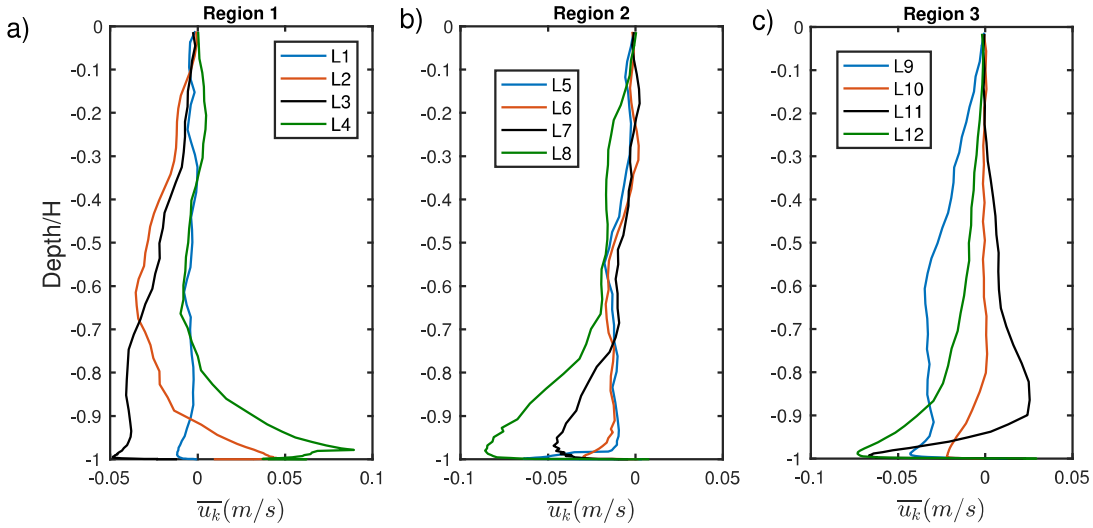

Figure 7.3: Ebb Velocity depth profiles for the mean vertical velocity $\overline{u_k}$: Regions 1-3 from are left to right(A,B,C).

ations. Mean velocity profiles also support comparisons to their flood counterpoints presented in chapter 4. Mean streamwise velocity depth profiles are presented in figure 7.2 for all lines probes divided by the three regions of the domain.The velocity profiles along the three regions decelerated as they travelled in the streamwise direction as a result of an expansion of the cross-sectional area, as opposed to the constrictions in the flow tide. The startup area of the domain is evident in lines L9 and L12 for region 3 as they are the closest line probes to the inlet. Region 1 hub height velocities were at a minimum for the domain for $\overline{u_i} = 1.6\ m/s$ at L1, while the highest hub height velocities were in region 3 lines near the inlet at $\overline{u_i} = 2.5\ m/s$. These values show equal magnitude reference velocities to the opposite flood velocities from chapter 4, albeit in an opposite direction as per ebb tide. Region 2 line probes shared a strong level of similarity in both magnitude and profile shape. Depth profile shape was uniform across all the regions, deviations from the norm are only present near the seabed.

Figure 7.3 shows how the expansion of the cross sectional area impacts mean velocity depth profiles for the vertical direction and not simply the dominant streamwise component. Only lines L2 and L4 did not exhibit a negative vertical velocity

near the seabed. While the contraction of the seabed in flood tide acted as a ramp for up bursts of the mean flow, the ebb tide adds a downward motion in the first 20% of the water column before returning to near zero velocity for the rest of the water column. Highest absolute vertical velocity can be found in region 2, particularly L8 with velocities up to $|\overline{u_k}| = 0.09\ (m/s)$. Mean negative vertical values near the seabed for most of the domain suggest predominantly sweeping motions, particularly in the bottom 20%, which was also found to be the main area of intermittency in chapter 5. Turbulence values should be analyzed further with a mean Reynolds stress calculation and quadrant event analysis to verify the influence of the downward motions.

7.3 Ebb Turbulence Parameters and Structure

Characterization of the turbulence flow begins with an overview of the diagonal components of the Reynolds stress tensor. This is done to understand the local variations along the water column, as well as the magnitudes for each line probe of the principal turbulent fluctuations. The turbulent kinetic budget will be presented by way of the main turbulence production shear term $\overline{-u_i' u_k'}$ of the Reynolds stress tensor. This will lead to a quadrant analysis of the aforementioned term, in an effort to view where turbulence production occurs through bursting events , and a comparison to the flood and baseline flat channel simulations.

The diagonal components of the Reynolds stress tensor are shown in figure 7.4. The effect of the wall bounded flow places the maxima of the $\overline{u_i' u_i'}$ component near the seabed. However, unlike flood flows results, a number of line probes (L6, L2 and L5) exhibit a secondary bulge emerging near the $Depth/H \approx -0.65$ mark. Similar results were seen in the turbulence intensity site measurements, explained by a retardation of the mean flow near the mid-column. The majority of the water column has a near constant value proportional to the mean streamwise flow. Thus both the maxima and average values of the $\overline{u_i' u_i'}$ component increase from region 1 to region 2, and are highest in region 3.

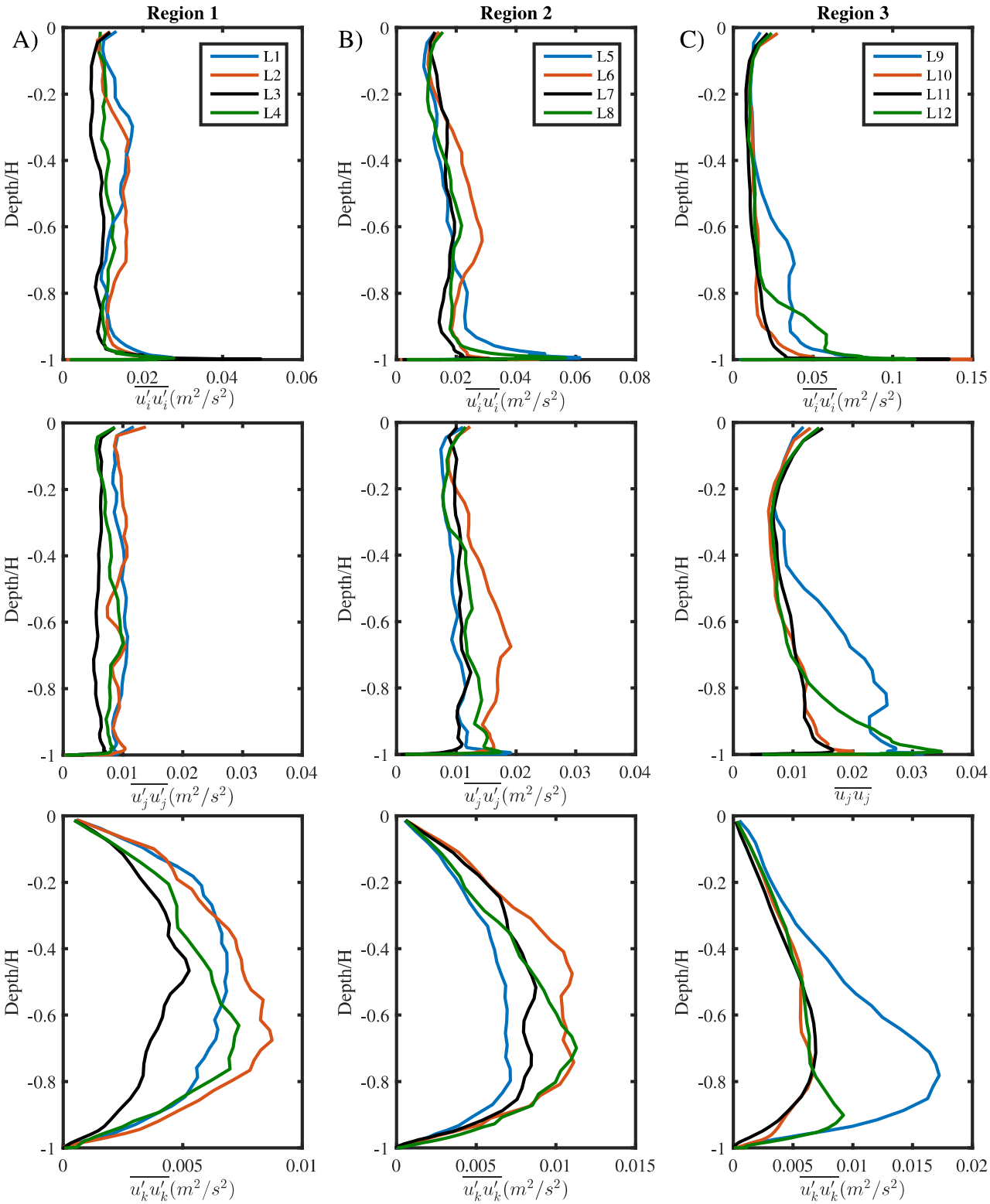

Figure 7.4: Diagonal component depth profiles of the Reynolds stress tensor $\overline{u_i'u_i'}$. Regions 1-3 from left to right.

The spanwise component $\overline{u'_j u'_j}$ is near constant across all three regions with a value of $\overline{u'_j u'_j} \approx (0.010 - 0.012)$. Local maximas were seen close to the seabed, yet not at the much higher values exhibited by the streamwise $\overline{u'_i u'_i}$ component. Neither the steady decrease in mean flow magnitude, nor the bathymetry appeared to have a strong local effect on the spanwise diagonal component. Although values for the vast majority of the water column remained in the same order of magnitude as the dominant streamwise component.

The last row, from top to bottom in figure 7.4 shows the diagonal vertical $\overline{u'_k u'_k}$component of of the Reynolds stress. Depth profiles increased in magnitude proportional to the mean flow and were characterized by a linear increase from the seabed to a maximum sustained bulge for a large portion of the water column. The location of the maximum magnitude bulge varied across line probes, yet all were within a location range of $Depth/H \approx -(-0.80\ to\ -0.65)$. It is worth noting that the maxima of the vertical Reynolds stress component was higher by 50% than for the flood tide value for the same velocity. This maxima was found to have its location shifted to higher values of the water column when comparing ebb to flood values. Both flood and ebb cases had the highest average value for its probes in region 2 and showed highest values in the depth range where the turbine rotor is located.

The main shear stress $-\overline{u'_i u'_k}$ Reynolds stress component for TKE production was found to have a higher maximum and average value in regions 1 and 2 for the ebb tide simulation, than for its flood tide counterpart. Values continued being highest in region 2. Depth profiles exhibited a parabolic shape with the maximum value near the $Depth/H \approx (-0.80\ to\ -0.60)$ location, similar to the vertical diagonal component. Regions 1 and 2 showed near parallel behavior for all line probes with discrepancies only in the maximum value. Region 3 line probes L12 and L9 can be taken out of the analysis as once more it is a sign of the development area of the domain. Although the mean of the shear term for all profiles was negative and indicative of its contribution to the TKE budget it does not provide a full picture of the transient bursting events from the seabed that are part of the energy generation

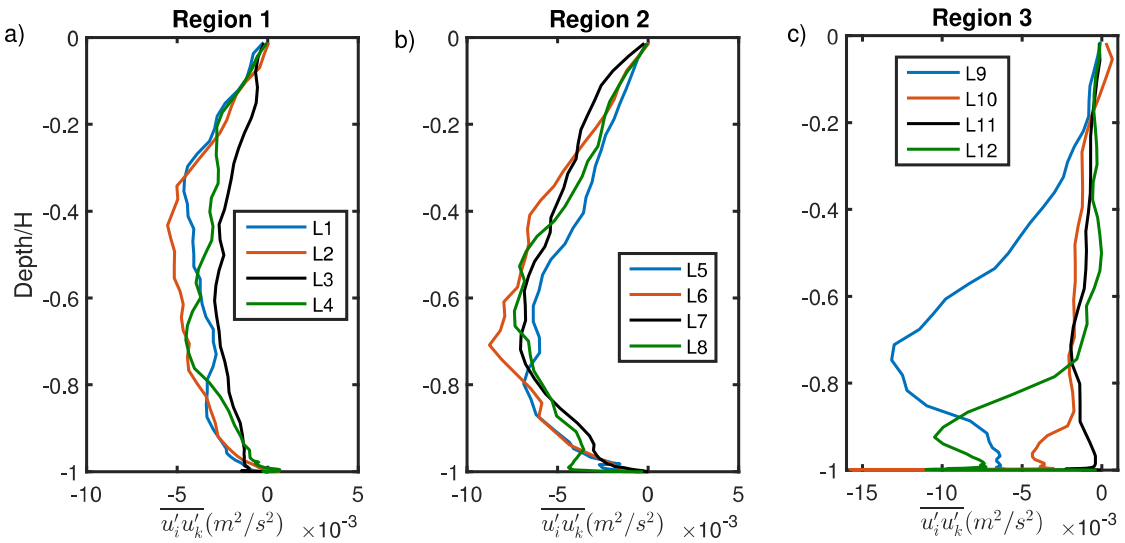

Figure 7.5: Main sheer Reynolds Stress component $\overline{u_i'u_k'}$ depth profile: Regions 1-3 from left to right.Legend for each line probe is shown in the first row.

process.

7.3.1 Quadrant Analysis of bursting events

Analysis of the turbulence shown during the ebb tide will not simply be directed towards the study of Reynolds stresses, but as has been seen in the previous chapters it is imperative to do a deeper statistical analysis for an understanding of the extreme turbulent events and values. Quadrant analysis of the $\overline{u_i u_k}$ Reynolds stress component was calculated for the same representative line probes and locations as in chapter 5 (for reference of locations see legend in figure 7.6). Probability density contours for all quadrants are shown in the same figure comparing the streamwise instantaneous component against the vertical instantaneous component each normalized by its standard deviation. Each quadrant analysis contour is bounded by hole sizes equal to 1 in dashed lines and equal to 4 for solid lines to contextualize the magnitude of the instantaneous stress burst.

Region 2 in particular is found to have an imbalance biased for Q4 sweeping events over Q2 bursts, confirming the initial assumption of the bathymetrical effect increasing sweeping motions. Sub-figures B1,B2 and B3 found a higher dominance

Table 7.1: Ebb-Flood Quadrant Analysis Comparison.

	Probability (-)			Energy Contribution (m^2/s^2)			Lifetime (s)	
	Q2	Q4	Q2/Q4	TKE_{Q2}	TKE_{Q4}	Q2/Q4	T_{Q2}	T_{Q4}
F10	0.323	0.316	1.020	0.70	0.70	1.000	2.44	2.23
F20	0.356	0.305	1.167	0.58	0.62	0.935	2.84	3.12
F50	0.320	0.350	0.914	0.65	0.58	1.120	4.02	3.64
Ebb10	0.329	0.382	0.861	0.74	0.65	1.138	4.47	2.86
Ebb20	0.307	0.309	0.993	0.70	0.65	1.077	3.90	3.55
Ebb50	0.317	0.334	0.949	0.65	0.53	1.226	3.60	3.32
FC10	0.287	0.314	0.914	0.85	0.63	1.335	2.54	1.88
FC20	0.347	0.304	1.141	0.63	0.71	0.909	2.18	2.01
FC50	0.321	0.318	1.009	0.76	0.74	1.023	1.95	1.86

of Q4 events and/or higher magnitude events than other regions. However Q4 dominance is evident as well in region 3 C1 and C2 subfigures, albeit at a lesser dominance. Probabilities densities at the midcolumn (bottom most row) are balanced across all four quadrants in regions 1 and 3, and are constrained between hole sizes equal to 1 leading to an assumption of isotropy and fewer high magnitude events as distance from the wall is highest. Regions 1 and 3 exhibited a high percentage of low magnitude events at the 20% mark of the water column. Areas with high probability (PDF=0.2-0.25) agglomerated near $\overline{u'w'} \approx 0$, where C2 had a spread out distribution amongst the quadrants; while A2 still showed probability contours of high magnitude. Higher mean streamwise velocities in region 3 did not have an impact on the extreme value events. All events were captured within the hole size $H = 4$ contours in region 3, while region 2 in B1 and B2 exhibit small probability contours outside of the larger hole. This would signify higher magnitude probabilities as extreme events in region 2 over region 1 even if not present in averaged turbulence values.

In order to review these quadrant statistics within a larger range of conditions, they must be compared to the flood and flat channel calculates values. Table 7.1 summarizes the results calculated of the quadrant analysis from the three main simulations run (flood, ebb and flat channel), specifically for bursting quadrant behavior.

Results are divided into the probability, energy contribution and mean lifetime of the bursting moments. Data shown in the table shows the filtered quadrant analysis parameters calculated from velocity taken at points at 10%, 20% and 50% of the water column at the center of the domain. This location was chosen for comparison as mean reference velocity ($u_{ref} = 2.1m/s$) was the same for all three simulations and its position near the turbine location. The notation used in the table uses 'F' to refer to flood simulation, 'E' for Ebb and 'FC' for the flat channel (see appendix A for a validation overview of the flat channel case); the following number denotes the vertical position of the point by the percentage of the water column starting from the seabed.

The imbalance between sweeping and bursting moments is analyzed to view the initial hypothesis of the effect of bathymetry ramping/down-turning of flow on bursting events. Ebb clearly shows an increase in probability of Q4 events over Q2, this increase in probability is seen to be highest at the bottom 10% of the water column closest to the seabed where its influence is at its highest. Q2/Q4 events at locations 10 and 20% of the column ocurred 18% more for ebb than for flood tides. The increase in probability does not transfer to higher Q4 energy contribution. Higher lifetime of Q2 events during would lead to a higher energy contribution, as the Q4 lifetimes were approximately the same as during the flood simulation. Energy contribution for Q2 bursting moments decreases as the distance to the seabed increased for all three simulations, in addition to the imbalance of Q2/Q4 probabilities as the influence of the wall decreases with the distance to the measured point. The base case of the flat channel shows lifetime of bursting events decreasing with the distance to the wall, however, this behavior does not follow for Q2 events during flood and Q4 during ebb simulations. Bathymetry ramping or down-turning is thought to bundle flow packets reaching higher portions of the water column increasing the average lifetime of the events, albeit at lower energy contents for its respective dominant quadrant.

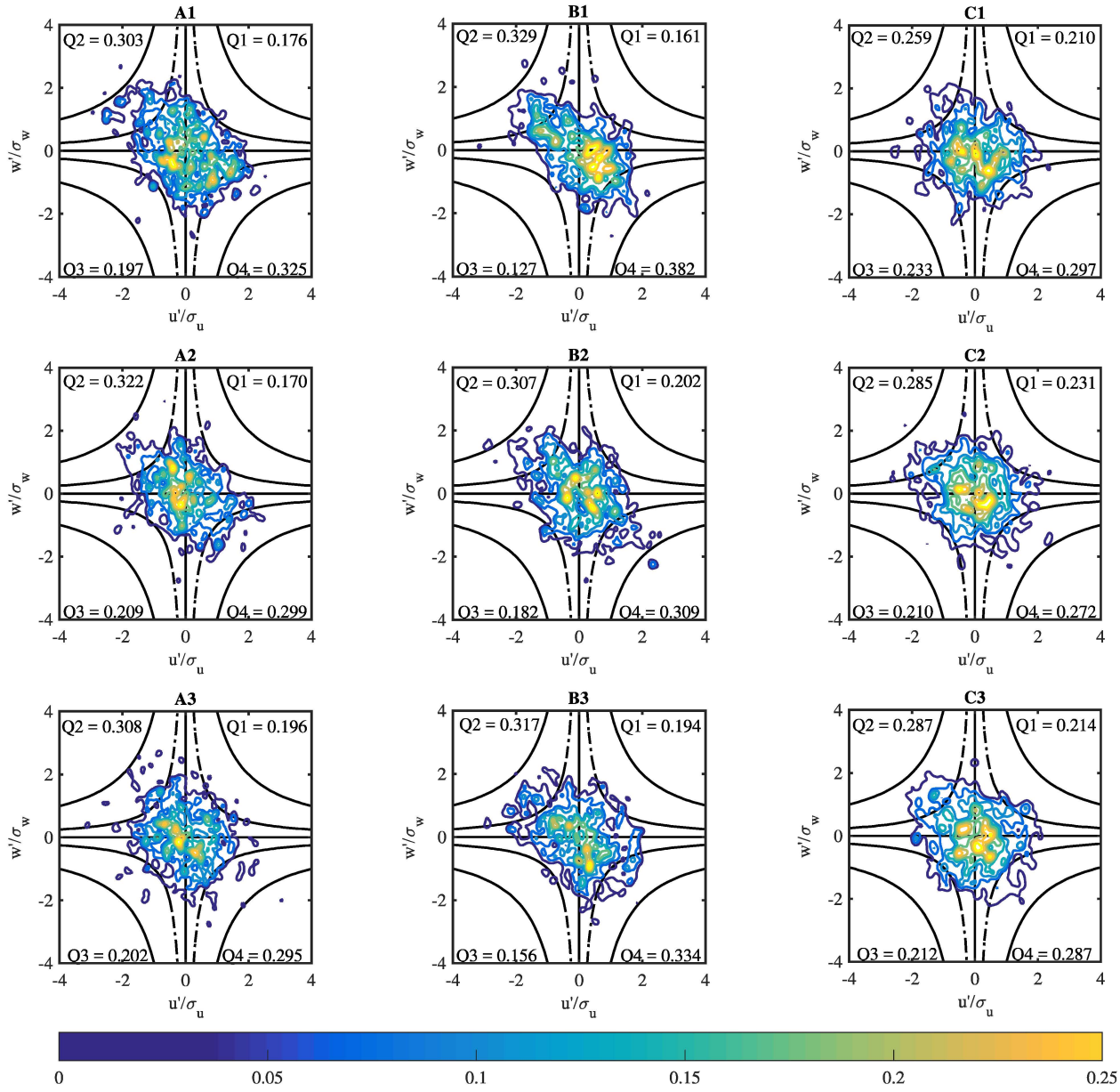

Figure 7.6: Quadrant Analysis contours coloured by their probability density function within 2 Hole (H) size=1 for the dashed and dotted line and H=4 for solid line. Legend in each quadrant refers to the contribution of each event to the total Reynolds stress component $\overline{u'w'}$. Both the streamwise component u' & vertical component w' have been normalized by their respective standard deviation σ. From left to right (A,B,C) are plots showing points at line probes for 3 regions (R1 left column, R2 middle column, R3 right column), from top to bottom are plots at vertical positions of 10% of the water column, 20% and the bottom most row is at 50% of the water column.

7.4 Ebb and Flow Turbulence Asymmetry

Both mean velocity, Reynolds stress and statistical bursting events have shown the effect of the bathymetry. The direction of the flow when paired with the bathymetry changes the mean flow as well as the turbulent fluctuations that emanate from the wall. The asymmetry between these two flows (ebb and flood) has been discussed mostly in terms of the entire period of the tidal component. Asymmetry at tidal sites between ebb and tide components has been mentioned by Hay et al. (2013) as a consequence of local topography and mentioned by Togneri et al. (2017). For the single-velocity cases that have been presented in this work it is convenient to compare the asymmetry to continue with the objectives set out by this chapter in seeing how strong of an impact bathymetry has on the difference between tides. The comparison continues by looking at the turbulent energy contained in the flow, production of the turbulence, and an important parameter for tidal turbines coherent turbulent kinetic energy.

Coherent turbulent kinetic energy (CTKE) proposed by Kelley et al. (2005) for wind energy environments, and since used by McCaffrey et al. (2015), Thomson et al. (2010) for tidal energy converter purposes. CTKE is a measure of the structural fatigue damage that impacts turbines as a result of coherent turbulent fluctuations. CTKE is mentioned as a root damage equivalent and peak load reference by Kelley (2011) and as a measure of the coherent structures by Thomson et al. (2010). Cross shear terms are taken into account due to their connection to energy producting coherent structures established in chapter 5. The measure is calculated by the non-diagonal components of the Reynolds stress and presented in equation 7.1.

$$CTKE = \frac{1}{2}\sqrt{\overline{u_i'u_j'}^2 + \overline{u_i'u_k'}^2 + \overline{u_j'u_k'}^2} \tag{7.1}$$

Figure 7.7 shows the time-averaged CTKE depth profiles for all of the line probes obtained in the domain (see table 4.1) for both flood (solid line) and ebb (dotted line) cases. Ebb depth profiles have been multiplied by -1 to visualize side by side. Depth was kept in terms of absolute value and not non-dimensionlized to view the effect of the maximum depth as well. CTKE scaled inversely with maxmimum depth

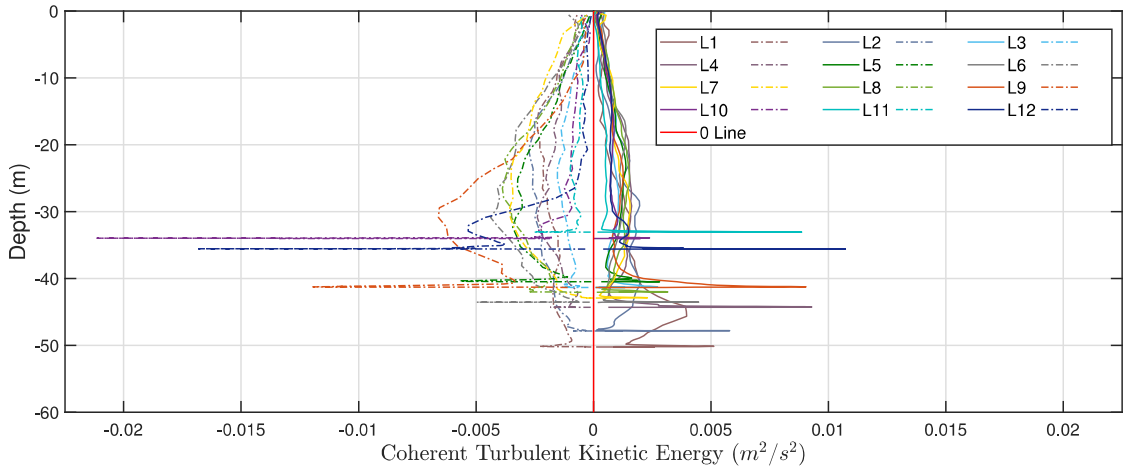

Figure 7.7: Averaged Coherent Turbulent Kinetic Energy (CTKE) plotted vs water depth for all line probes for flood and ebb simulations. Dashed line corresponds to $-CTKE$ Ebb depth profiles to better contrast with the corresponding Flood depth profiles in solid lines.

of the line probe as it related to higher mean flows for both ebb and flood cases (see line probes L10 and L12). Flood profiles hold a maxima near the seabed in the same way as ebb. However, the majority of the water column held secondary bulges 10 m from the seabed during ebb in contrast to the near constant flow during flood.

CTKE values were generally higher for ebb than for their flood counterparts. The ratio between CTKE depth profiles averaged a value $CTKE_{ebb}/CTKE_{flood} = 1.63$, the asymmetry was particularly strong for line probes in region where the ratio reached is 2.15. The higher ratio for ebb is related to the secondary bulges at near the mid-column for ebb flows. This secondary bulge would be of increased importance not only both for structural design of tidal turbines during ebb flow operation but also as a consideration for tidal asymmetry ramifications.

Turbulent kinetic energy depth profiles are shown for all line probes in figure 7.8 comparing ebb and flood tide together. Ebb TKE profiles are shown in dashed lines and multiplied by -1 for a better visualization. Ebb profiles showed a higher level of TKE than its corresponding flood profile, both in terms of the maximum value near the seabed as well as a sustained higher value for most of the water column.

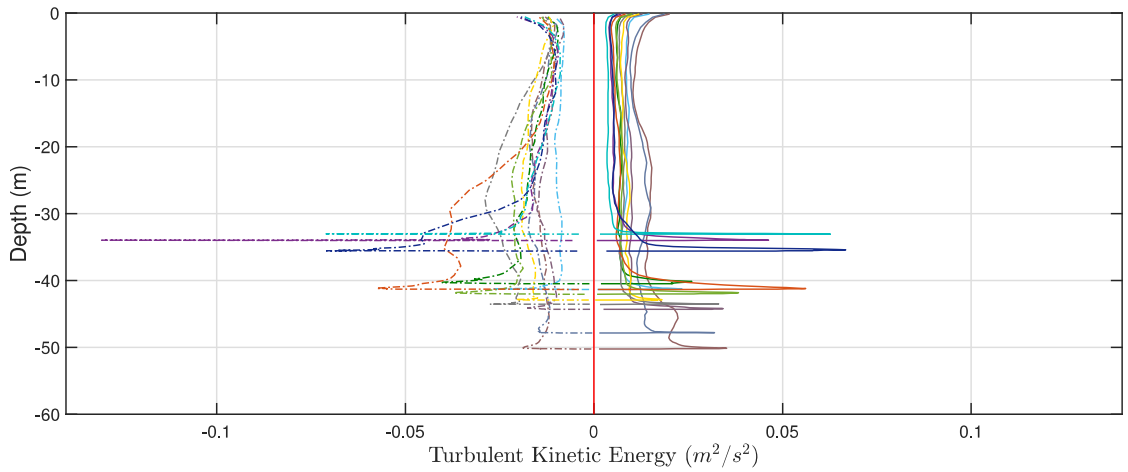

Figure 7.8: Averaged Turbulent Kinetic Energy (TKE) plotted vs water depth for all line probes for flood and ebb simulations. Dashed line corresponds to $-CTKE$ Ebb depth profiles to better contrast with the corresponding Flood depth profiles.Legend as in figure 7.7.

Maximum values of both CTKE and TKE were both shown at L9 for ebb tide, TKE was near constant during flood tide. Higher values of turbulent energy during ebb tide calculated in the simulation follows the acoustic ADV data measurements for the Fall of Warness by Fraser (2017), particularly near the seabed.

Production ratios between the flood and ebb tides, shown in figure 7.9 were calculated with special attention to the central region of the domain due to it's the location of the turbine. The average ratio between the tide production $\mathcal{P}_{Ebb}/\mathcal{P}_{Flood} = 1.25$ for all line probes. TKE production was symmetrical for the turbine rotor range in locations ranging between -30 and -10 m along the water column. Points near the seabed were the ones with higher discrepancy between the tides, this becomes more important for TKE production purposes as highest values ($\approx 10^{-1}$) are found near the seabed. Figure 7.9 shows a comparison of the turbulence production $\mathcal{P}$ for the 2.1 m/s flood and ebb simulations of region 2 as it was the region most distant from the inlet and outlet boundary conditions in both ebb and flood simulations. Ratio between production values was highest near the seabed up to 10 m distance from it. Values for the majority of the water column remained at equal ratios between tides,

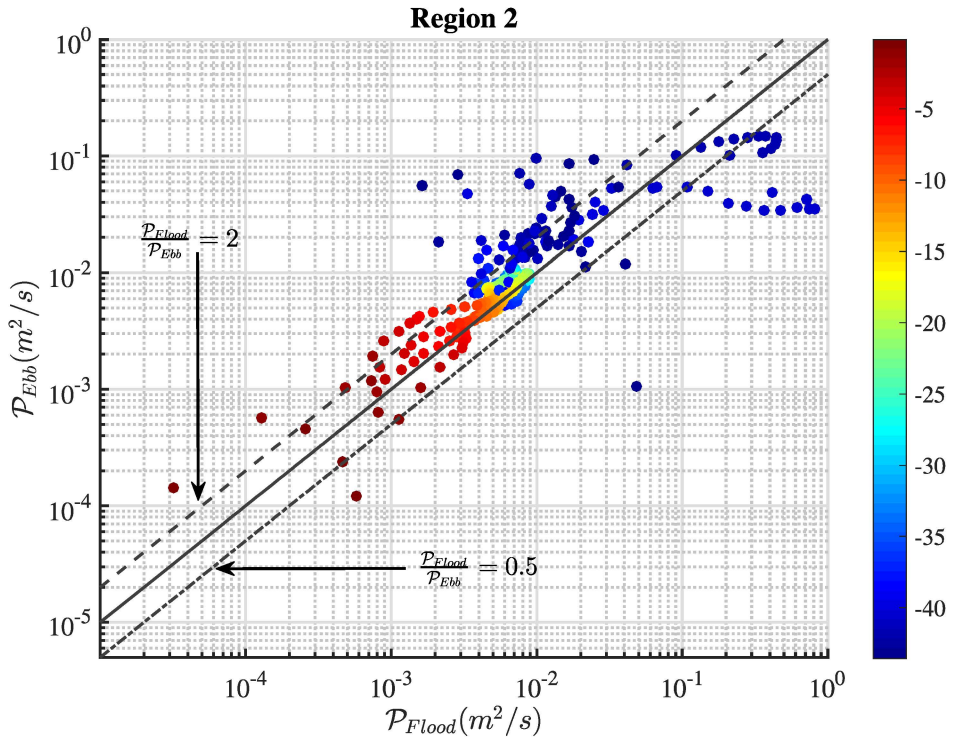

Figure 7.9: Turbulence Production rate $\mathcal{P}$ comparison for Flood versus Ebb Tides at positions in region 2. Vertical Position in the water column in indicated by colorbar.

however the influence of the seabed on the inequality must be stressed.

The spatial character of turbulence between the two tidal conditions was analyzed by comparing the integral length scale depth profiles in figure 7.10. Length scales depth profiles are plotted for all 12 line probes, the vertical axis is non-dimensionalized by $Depth/H$ to better compare the shape of the profile. Ebb profiles are shown in dashed lines and have been multiplied by -1 for a better visualization in opposition to their flood counterparts. The figure shows a clear difference between the ebb and flood profiles, for both shape and magnitude, flood exhibits lengths scales larger by an average factor of 1.2.

The difference between the depth profiles was not simply a matter of magnitude but of the profile shape as well. Flood length scales, as discussed in Chapter 4, closely matched the theoretical profile by Nezu and Nakagawa (1993) of a linearly increasing area in the lower middle water column followed by a constant value equal to half of the maximum depth. Flood tide length scales diverge only in the position

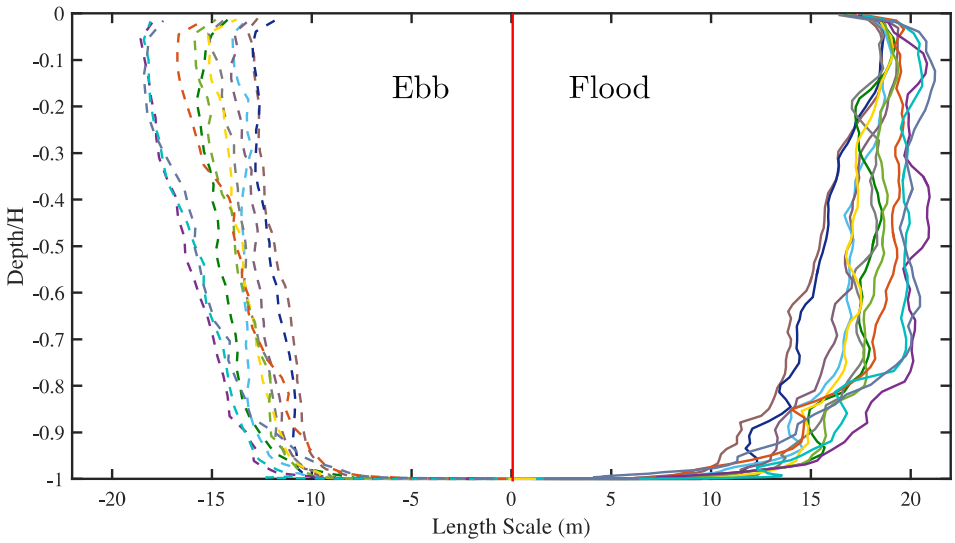

Figure 7.10: Integral Length Scale (m) depth profiles, non-dimensionalized by Depth/H for ebb and flood simulations. Ebb simulation profiles are multiplied -1 for best comparison to Flood. Legend as in figure 7.7.

of the separation of the two theoretical behaviors, finding it not at the mid-column but at values of $Depth/H = (-0.8\ to\ -0.6)$. Ebb tide does not have the constant value behaviour of the upper half of the water column. Ebb depth length scale keeps increasing linearly with its distance from the seabed after a short parabolic rise near the seabed $Depth/H \approx -0.9$. Largest length scale values belong to the lineprobes at highest mean flow velocity for both flood and ebb simulations, as higher velocities contain a larger integral length scale frequency range.

7.4.1 Turbulent structure asymmetry

The structural nature and shape of the turbulence is seen to change with depth in chapter 5 for flood tide across regions. The direction of the flow, and its interaction with the seabed was found to change the probability and energy content distribution of the bursting events. Thus, it is a natural next step to visualize the turbulence as it moves from the seabed to the surface. Due to the existence of the startup area for region 1 in flood tide and region 3 for ebb tide comparison was kept for all line probes in region 2. A baseline was added to the comparison in the way of an

anisotropy invariant mapping of a flat channel simulation. The uniform depth of the flat channel was kept at the maximum depth of the realistic bathymetry $H = -55m$.

Figure 7.11 shows the anisotropy invariant map, as was explained in chapter 5, for a) reference flat channel b) ebb simulation and c) flood simulation watercolumns at the the center of the domain colored by depth. The reference flat channel begins the water column at a higher and more sustained degree of anisotropy straddling the 2D dimensional condition line for the first meter along the seabed before returning to full isotropy at the mid column by way of the axisymmetric condition line for points (2-5) m from the seabed. Finally the water column returns to a 2D condition due to the top lid boundary condition and its condition of impermeability. Both ebb and flood change their points in comparison to the flat channel, albeit by different pathways.

All three simulations showed full isotropy by mid-column and 2D isotropy as driven by their wall boundary conditions. The main difference between the AIM plots lie in the first $5m$ of the water column. While ebb tide maintains a similar level of high anisotropy (described in the second invariant -II) than the flat channel it does not remain two-dimensional for all points near the seabed. The path to the isotropical condition at the mid column does not approach the rod-like axisymmetrical line, with the exception of few points nearest to the seabed at a high level of anisotropy. The points nearest to the surface $H = (-7\ to\ 0)\ m$ follow the "disk-like" axisymmetrical line (shown in red in figure 7.11) before coming near to the two-dimensional condition at the surface.

The Anisotropy invariant map for flood in figure 7.11 c) has a lower magnitude of anisotropy than both ebb and flat channel. The near seabed points follow the black two-dimensional line before turning to an isotropical condition, touching the red "disk-like" axisymmetric condition. It must be mentioned that some points were found outside of the boundaries as mentioned in chapter 5 due to discretization errors, these points will be considered at positions located at the nearest boundary.

Both ebb and flood simulations show how, on average, bathymetry roughness features decrease the level of anisotropy for all points and make the transition to

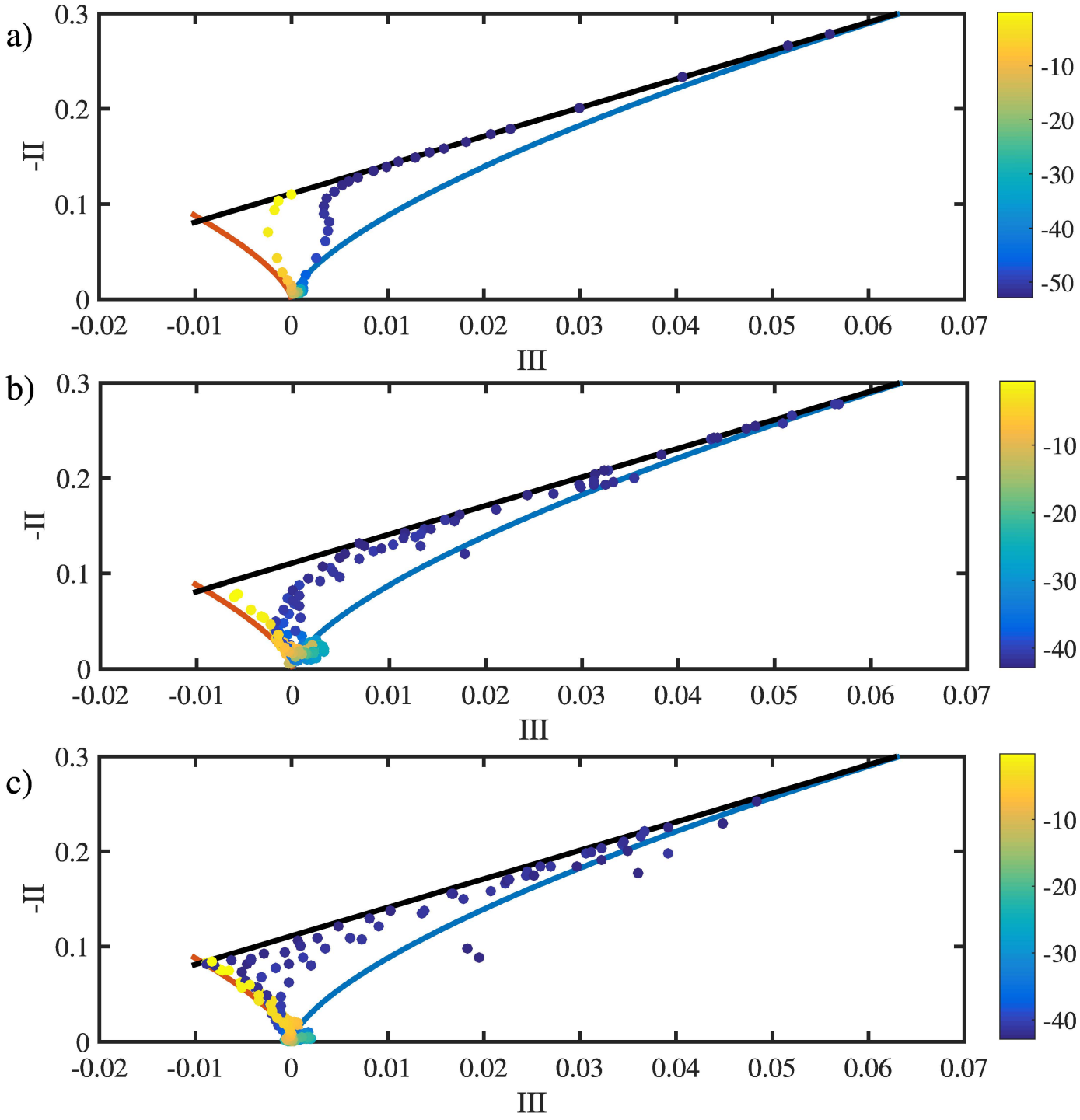

Figure 7.11: Anisotropy Invariant map for lines probes in region 2 colored by depth of the following simulations: a) Flat channel simulation b) Ebb simulation c) Flood simulation

isotropy occur at lower depths. Both flood and ebb show points near the seabed that indicate "rod-like" turbulence but only at the lowest points of the water column. Flood shows a stronger two-dimensional character for points below the mid-column and "disk-like" near the surface than ebb. This is consistent with the quadrant analysis seen in table 7.1 where only large bursting moments occurred at the deepest sampled points and the literature by Ashrafian and Andersson (2006); De Marchis and Napoli (2012); Krogstad and Efros (2012) concerning wall effect on anisotropy throughout the water column depth.

7.5 Discussion and final comments

The results shown in this chapter were the output of an LES simulation created with the objective of characterizing the turbulent flow of a 2.1 m/s ebb flow. These results are of importance not only to understand the ebb tide flow but also as part of broader range of flows when coupled and compared to previous results of flood tide. The simulation was validated against the site measurements of an equal mean reference flow from Sellar et al. (2018). Simulation results were capable of capturing the retardation of the mean flow in the upper portions of the water column that effect the mean flow and turbulence intensity profiles albeit with an overestimation of TI near the seabed.

Mean turbulence parameters, as well as statistical analysis of shear stresses were presented to understand the turbulent nature of ebb flow and its variability throughout the domain. Bathymetry variation affected the mean Reynolds stress depth profiles, particularly for $\overline{u_i u_i}$ and $\overline{u_k u_k}$diagonal components. The effect manifested itself through increases in flow speed and higher shear stress. Depth changes on the seabed impacted not only the maximum magnitudes of the depth profiles but also the shape of the depth profile creating a secondary bulge along the watercoumn of the streamwise Reynolds stress diagonal component. Additionally, bathymetry was found to push the area of maximum $\overline{u_i u_k}$ to the same range of the water column as the turbine rotor.

Turbulent producing bursting events showed a preponderance of sweeping motions at all near seabed locations for ebb simulation, especially in comparison to flat channel and flood simulation results. Dominance of sweeping over bursting events is in line with the experimental findings of Mazumder and Sarkar (2014); Lefebvre and Winter (2016) for declined surface geometries (for geometries at an inclination of 6°, although Lefebvre and Winter (2016) mentions the necessary inclination for this dominance to occur is as low as 0.4 °) and the opposite occurring for inclined surfaces up to a difference of $Q2/Q4 = 1.13 - 1.25$ disappearing by mid watercolumn. This disparity impacted the turbulence structure of the flow, creating a higher amount of anisotropy near the seabed than the flood case, which is later lost as the water column returns to isotropy at a lower portion of the water column in all three regions of the domain as seen in the quadrant analysis and the anisotropy invariant map.

The comparison between flood and ebb parameters showed a clear asymmetry in turbulence spatial and averaged conditions. The asymmetry between tidal components was expected as seen in measurements by Seller and Sutherland (2015); Fraser (2017) and seen in many tidal environments Korotenko and Senchev (2011); McCaffrey et al. (2015); Thomson et al. (2010); L.Brennan et al. (2002); Stacey and Ralston (2005); Garcia Novo and Kyozuka (2018). Both CTKE and TKE levels were calculated to be higher by 63% and 50% respectively, this difference as driven by higher maxima near the seabed and a secondary bulge in the 10 meters from the seabed. Higher energy levels were corroborated by turbulence production rates in region 2 of the domain. Production rates were higher for ebb tide by 25% on average throughout the water column with a strong emphasis on asymmetry in the first 5 m from the seabed. Similar measurements were found by Stacey and Ralston (2005) in a tidal estuary in San Francisco Bay, calculating ebb TKE values to be up to 2 times the flood energy as a result of bathymetry irregularities.

Tidal asymmetry was not constrained exclusively to turbulent energy levels but manifest itself to the size of turbulent eddies as measured by integral length scales. Ebb length scales were found to be 33% smaller on average than their flood coun-

terparts. Profile shape was consistent for line probes in their respective simulation. Ebb length scale profiles were shown to be of an increasing linear nature along the water column while flood held a constant value range for the majority of the water column. Milne et al. (2017) found similar values at the Sound of Islay where one tidal component behaved as a linear increase versus a two behaviour profile for the remaining tidal component.

The influence of the direction of the flow combined with the bathymetry of the domain were shown through the presented results to be a main driver for turbulence behaviour and energy levels. The effects of each site bathymetry are highly local, however there seems to be a level of similarity between asymmetry measurements of tidal cycles (L.Brennan et al., 2002; Milne et al., 2013). Diverging and converging bathymetry drives flow to accelerate or decelerate depending on the direction of the flow at site dependent angles of seabed inclination.

The full effect of the tidal asymmetry would still require an amount of time varying flow to capture the transition between ebb and flow as well as slack flow when utilizing a realistic bathymetry as a boundary condition. High resolution LES turbulence modelling becomes an expensive technique for time variating cases. Wall modelled LES simulations and DES may prove to be an acceptable compromise in the future to model a full tidal cycle while preserving the ability to capture extreme values even if not at full resolution of the energy spectrum.

CHAPTER 8

CONCLUSIONS

8.1 Summary and conclusions

The work just presented was created to contribute to the body of knowledge related to turbulence at tidal energy sites. The work demonstrated the applicability of high resolution numerical computational fluid dynamics to model, process and analyze unsteady turbulent flows; aiming to characterize the spatial and temporal turbulent nature and energetic events of a tidal environment. This was done for a specific location in the Fall of Warness,Scotland and was supported by site data for comparison and model development.The combination of bathymetry and flow direction was studied and simulated for a characteristic velocity for ebb and flood tides. The specific environmental site characteristics such as bathymetry and flow velocities were found to greatly influence the generation cycle of turbulent energy beyond what previous idealized models have suggested.

Idealization of complex sea state bathymetry and flow time scales may not always present a complete picture of the flow, decreasing the robustness and losing unique site characteristic influence. A deeper understanding of the different energy rich turbulent events helps further a practical understanding of offshore flows. The knowledge gained from this work will be applicable to tidal energy, and hopefully

be transferable to a host of related offshore engineering applications. The methods used in this body of work, while resource intensive, are within the realm of possibility for engineering analysis to obtain high resolution time histories for sites. The output capabilities of the model go beyond averaged turbulence parameters, aiding engineering design of tidal turbines for short yet energetic turbulent phenomena previously washed away by time averaged models. The initial aim of this work to produce a faithful and representative model of the EMEC tidal energy site at The Fall of Warness was completed in terms of explaining the role the bathymetry had on averaged tides. While the model can be improved to include extended areas and a time domain simulation the initial aim and research questions are considered sufficiently answered.

Research objectives of this thesis were stated at the beginning of the body of work. They are repeated here and answered from the results of the research as a way to summarize the main findings.

1. Is it possible and how does one develop affordable and available numerical models capable of capturing the unique turbulent character of a tidal energy site?

   The use of LES turbulent models was shown to be effective at capturing a great proportion of the turbulent motions of the flow end their energy. The model was not constructed to capture the smallest of viscous scales more than for engineering design purposes. Model resolutions of 0.5-2 m were aimed at reproducing device component scale relevant turbulence. The model, aided by site inflow data, was able to recreate the spatial anisotropy and turbulent magnitudes found at the Fall of Warness showing the fidelity and quality of the method and model. The model being constructed on commercial software Star-CCM+ shows the viability of the method as a viable and affordable method to characterize specific site flows beyond academic research tools.

2. What is the effect of seabed irregularities on turbulence statistics and can it explain the discrepancies between site measurements and ideal flows?

The ramping bathymetry of the Fall of Warness was found to be a main factor in the generation of turbulent discrete events and averaged turbulent values. The local bathymetry controlled flow acceleration and drove the main and secondary flow directions near the seabed. Reynolds stress maxima for water columns were determined by the specific bathymetry gradients, high Reynolds stress dependence on bathymetry decreased sharply as flows furthered from the seabed, however secondary maxima were seen at specific locations. These bathymetry gradients are ignored in idealized flat channel simulations and thus underestimate turbulent magnitudes in both averaged and localized measurements.

3. What are the turbulent structures present in tidal channel flow and how do they contribute to the kinetic energy budget of the flow?

   Analysis of the high-resolution velocity time histories was focused on the spatial and structural nature of turbulent fluctuations. Turbulent structure was calculated to be of a decreased anisotropy for portions of the water column far from the seabed. The irregularities of the seabed force the flow to an isotropic state at higher depths. At depths near the seabed rod like structures were found with a highly energetic sustained lifetime. The lifetime of these structures was of a sufficient time scale to impact the performance of tidal turbine blades and structure. Extreme value turbulent events, while relatively rare, were found to be up to 20 times as energetic as averaged turbulence parameters would suggest. The nature of turbulent coherent structures influences hydrodynamic forces on subsea structures enough to be an important factor in design outside of normal assumptions of isotropy and non-statistical turbulence, particularly at regions near the seabed. The turbulent generation-dissipation life cycle is born from the connection between seabed wall forcing, to disregard it in any simulation will lose contributions of the kinetic energy budget.

4. What role do the ebb and flood tides, and thus direction of the flow, play on

the turbulent nature of the flow?

Ebb and flood flow for 2.1 m/s showed a high level of asymmetry in measurements of averaged turbulence parameters and discrete turbulent event statistics. This asymmetry was not only an increase of magnitude but also a change of depth profile shapes. Asymmetry played a larger role near the seabed, most of its effects dissipating by mid column. Ebb flows produced higher levels of turbulent energy at larger integral scales. It is thought that the increase in energy levels is due to a higher level of anisotropy for lower portions of the water column, creating a larger probability of sweeping events. This is not a general rule for ebb flows , but a result of the interaction between flow direction and the local bathymetry. However, it shows the importance of taking into their interaction for each site. Comparison of ebb and flow tides to ideal flat channel simulations show the deficiency of flat channel bathymetries for recreating the turbulence generation cycle and sustained turbulent local maxima.

8.2 Recommendations for future work

The combination of bathymetry and flow direction was simulated for a characteristic velocity for ebb and flood tides. However, an understanding of the main semi-diurnal tidal cycle requires analysis of not only steady single velocity flows, but a time-variating signal with corresponding slack periods. A more complete picture of the turbulence statistics at a site should take into account the temporal changes of turbulent phenomena as flows accelerate and decelerate as a function of the tidal period as well as in combination with the flow alterations of the bathymetry. The numerical resources required for a coupling of these effects make it an ambitious goal for future research.

In addition, the work presented here was independent of wave conditions on the surface of the water column. While the bathymetry played an important role in the turbulence life cycle in the bottom portion of the water column, surface unsteadiness is mainly driven by wave behavior. The influence of surface waves convects

downwards into the water column towards the seabed eventually meeting turbulence created at the seabed. Further experimental and numerical work coupling the effect of the surface waves and seabed on turbulence would join some of the largest influences of the turbulence life-cycle for a majority of the water depth. Previous work has been done with wave-current coupling, however the methodology shown here with high resolution models would further explore the fundamental hydrodynamics of the interaction between wave-current for specific sites.

The potential of high resolution CFD for the aforementioned phenomena was shown in this body of work. Further simplification and modification in the methodology is necessary to attempt wave and tidal cycle eddy modeling. However, the capabilities of large eddy simulation and similar high resolution turbulence models have shown to be an attractive future next step in understanding ocean turbulence in addition to being available for engineering design.

BIBLIOGRAPHY

Adcock, T. A., Draper, S., and Nishino, T. (2015). Tidal power generation - A review of hydrodynamic modelling. In *Proceedings of the Institution of Mechanical Engineers, Part A: Journal of Power and Energy*, volume 229, pages 755–771.

Adrian, R. J. (2007). Hairpin vortex organization in wall turbulencea. *Physics of Fluids*, 19(4).

Adrian, R. J., Balachandar, S., and Liu, Z. C. (2001). Spanwise growth of vortex structure in wall turbulence. *KSME International Journal*, 15(12):1741–1749.

Afgan, I., McNaughton, J., Rolfo, S., Apsley, D. D., Stallard, T., and Stansby, P. (2013). Turbulent flow and loading on a tidal stream turbine by LES and RANS. *International Journal of Heat and Fluid Flow*, 43:96–108.

Ahmed, U., Afgan, I., Apsley, D. D., Stallard, T., and Stansby, P. K. (2015). CFD Simulations of a Full-Scale Tidal Turbine: Comparison of LES and RANS with Field Data. *Proceedings of the 11th European Wave and Tidal Energy Conference*, pages 1–8.

Alfredsson, P. H., Örlü, R., and Segalini, A. (2012). A new formulation for the streamwise turbulence intensity distribution in wall-bounded turbulent flows. *European Journal of Mechanics, B/Fluids*.

Antonia, R. A. and Krogstad, P. (2001). Turbulence structure in boundary layers over different types of surface roughness. *Fluid Dynamics Research*, 28(2):139–157.

Ashrafian, A. and Andersson, H. I. (2006). The structure of turbulence in a rod-roughened channel. *International Journal of Heat and Fluid Flow*, 27(1):65–79.

Balakumar, B. and Adrian, R. (2007). Large- and very-large-scale motions in channel and boundary-layer flows. *Philosophical Transactions of the Royal Society A: Mathematical, Physical and Engineering Sciences*, 365(1852):665–681.

Batten, W. M., Harrison, M. E., and Bahaj, A. S. (2013). Accuracy of the actuator disc-RANS approach for predicting the performance and wake of tidal turbines. *Philosophical Transactions of the Royal Society A: Mathematical, Physical and Engineering Sciences*.

Bechmann, A., Sørensen, N. N., Sørensen, A. B., and N., N. (2010). Hybrid RANS/LES method for wind flow over complex terrain. *Wind Energy*, 13(2010):36–50.

Blackmore, T., Myers, L. E., and Bahaj, A. S. (2016). Effects of turbulence on tidal turbines: Implications to performance, blade loads, and condition monitoring. *International Journal of Marine Energy*, 14:1–26.

Bose, S. T. and Park, G. I. (2018). Wall-Modeled Large-Eddy Simulation for Complex Turbulent Flows. *Annual Review of Fluid Mechanics*.

Breton, S.-P., Sumner, J., Sørensen, J., Hansen, K., Sarmast, S., and Ivanell, S. (2017). A survey of modelling methods for high-fidelity wind farm simulations using large eddy simulation. *Philosophical Transactions of the Royal Society A: Mathematical, Physical and Engineering Sciences*.

Castro, I. P., Segalini, A., and Alfredsson, P. H. (2013). Outer-layer turbulence intensities in smooth- and rough-wall boundary layers. *Journal of Fluid Mechanics*.

Celik, I., Klein, M., Freitag, M., and Janicka, J. (2006). Assessment measures for URANS/DES/LES: An overview with applications.

Celik, I., Klein, M., and Janicka, J. (2009). Assessment Measures for Engineering LES Applications. *Journal of Fluids Engineering*.

Celik, I. B. (1999). Introductory Turbulence Modeling Lectures Notes by. *West Virginia University*, (December).

Celik, I. B., Cehreli, Z. N., and Yavuz, I. (2005). Index of Resolution Quality for Large Eddy Simulations. *Journal of Fluids Engineering*.

Chang, K. and Constantinescu, G. (2013). Coherent structures in flow over two-dimensional dunes. *Water Resources Research*, 49(5):2446–2460.

Choi, H. and Moin, P. (2012). Grid-point requirements for large eddy simulation: Chapman's estimates revisited. *Physics of Fluids*.

Choi, K. S. and Lumley, J. L. (2001). The return to isotropy of homogeneous turbulence. *Journal of Fluid Mechanics*.

Choi, K. S., Lumley, J. L., Krogstad, P. ., Antonia, R., Simonsen, A. J., and Krogstad, P. . (2001). The return to isotropy of homogeneous turbulence. *Experiments in fluids*.

Christensen, K. T. and Adrian, R. J. (2001). Statistical evidence of hairpin vortex packets in wall turbulence. *Journal of Fluid Mechanics*, 431:433–443.

Creech, A. C., Borthwick, A. G., and Ingram, D. (2017). Effects of support structures in an LES actuator line model of a tidal turbine with contra-rotating rotors. *Energies*.

Cui, J., Patel, V. C., and Lin, C. L. (2003). Large-eddy simulation of turbulent flow in a channel with rib roughness. *International Journal of Heat and Fluid Flow*.

Davidson, L. (2009). Large Eddy Simulations: How to evaluate resolution. *International Journal of Heat and Fluid Flow*.

Davidson, L. (2012). Fluid mechanics, turbulent flow and turbulence modeling. *CFD course*, pages 1–270.

Davidson, L. and Dahlström, S. (2005). Hybrid LES-RANS: An approach to make les applicable at high Reynolds number. In *International Journal of Computational Fluid Dynamics*.

Davies, G. (2017). WAVE & TIDAL ENERGY : Report to Climate Change. (December).

De Marchis, M. and Napoli, E. (2012). Effects of irregular two-dimensional and three-dimensional surface roughness in turbulent channel flows. *International Journal of Heat and Fluid Flow*, 36:7–17.

de Marchis, M., Napoli, E., and Armenio, V. (2010). Turbulence structures over irregular rough surfaces. *Journal of Turbulence*, 11(3):1–32.

Driest, E. (1956). On Turbulent Flow Near a Wall. *Journal of the Aeronautical Sciences (Institute of the Aeronautical Sciences)*.

Ferziger, J. and Peric, M. (2002). *Computational Methods for Fluid Dynamics*. Springer, Berlin, 3rd edition.

Flack, K. A. and Schultz, M. P. (2014). Roughness effects on wall-bounded turbulent flows. *Citation: Physics of Fluids*, 26:65103.

Fraser, S. (2017). *Acoustic Investigation of the Hydrodynamics and Ecology of a Tidal Channel and the Impacts of a Marine Renewable Energy Installation*. PhD thesis, University of Aberdeen.

Fröhlich, J., Mellen, C. P., Rodi, W., Temmerman, L., and Leschziner, M. A. (2005a). Highly resolved large-eddy simulation of separated flow in a channel with streamwise periodic constrictions. *Journal of Fluid Mechanics*, 526:19–66.

Fröhlich, J., Mellen, C. P., Rodi, W., Temmerman, L., and Leschziner, M. A. (2005b). Highly resolved large-eddy simulation of separated flow in a channel with streamwise periodic constrictions. *Journal of Fluid Mechanics*, 526:19–66.

Gant, S. and Stallard, T. (2008). Modelling a Tidal Turbine in Unsteady Flow. *Proceedings of the Eighteenth (2008) International Offshore and Polar Engineering Conference*, 8(2007):473–480.

Garcia Novo, P. and Kyozuka, Y. (2018). Analysis of turbulence and extreme current velocity values in a tidal channel. *Journal of Marine Science and Technology (Japan)*.

George, W. K. (2010). Lectures in Turbulence for the 21st Century, Imperial College of London and Chalmers University of Tecnhology. (January).

Germano, M., Piomelli, U., Moin, P., and Cabot, W. H. (1991). A dynamic subgrid-scale eddy viscosity model. *Physics of Fluids A*.

Grabbe, M., Lalander, E., Lundin, S., and Leijon, M. (2009). A review of the tidal current energy resource in Norway.

Grass, A. J. (1971). Structural features of turbulent flow over smooth and rough boundaries. *Journal of Fluid Mechanics*.

Gunawan, B., Neary, V. S., and Colby, J. (2014). Tidal energy site resource assessment in the East River tidal strait, near Roosevelt Island, New York, New York. *Renewable Energy*, 71:509–517.

Han, Y., Stoellinger, M., and Naughton, J. (2016). Large eddy simulation for atmospheric boundary layer flow over flat and complex terrains. In *Journal of Physics: Conference Series*.

Hay, A. E., McMillan, J. M., Cheel, R., and Schillinger, D. J. (2013). Turbulence and Drag in a High Reynolds Number Tidal Passage Targetted for In-Stream Tidal Power. *Oceans 2013 San DIego*, pages 1–10.

Head, M. R. and Bandyopadhyay, P. (1981). New aspects of turbulent boundary-layer structure. *Journal of Fluid Mechanics*.

Issa, R. I. (1985). Solution of the Implicitly Discretised Fluid Flow Equations by Operator-Splitting. Technical report.

Jarrin, N., Benhamadouche, S., Laurence, D., and Prosser, R. (2006). A synthetic-eddy-method for generating inflow conditions for large-eddy simulations. *International Journal of Heat and Fluid Flow*.

Jeanmart, H. and Winckelmans, G. (2002). Comparison of recent dynamic subgrid-scale models in turbulent channel flow. In *Proceedings of the Summer Program*, pages 105–116, Dallas, Texas.

Jeong, J. and Hussain, F. (1995). On the identification of a vortex. *Journal of Fluid Mechanics*, 285:69–94.

Jimenez, J. (2004). TURBULENT FLOWS OVER ROUGH WALLS. *Annual Review of Fluid Mechanics*.

Kelley, N., B.J. Jonkman, Scott, G., Bialasiewicz, J., and Redmond, L. (2005). The Impact of Coherent Turbulence on Wind Turbine Aeroelastic Response and Its Simulation. In *WindPower 2005*, page 22. NREL.

Kelley, N. D. (2011). Turbulence-Turbine Interaction: The Basis for the Development of the TurbSim Stochastic Simulator. Technical report.

Kim, H. T., Kline, S. J., and Reynolds, W. C. (1971). The production of turbulence near a smooth wall in a turbulent boundary layer. *Journal of Fluid Mechanics*.

Kim, K. C. and Adrian, R. J. (1999). Very large-scale motion in the outer layer. *Physics of Fluids*, 11(2):417–422.

Kline, S. J., Reynolds, W. C., Schraub, F. A., and Runstadler, P. W. (1967). The structure of turbulent boundary layers. *Journal of Fluid Mechanics*.

Kolmogorov, A. N. (2006). Dissipation of Energy in the Locally Isotropic Turbulence. *Proceedings of the Royal Society A: Mathematical, Physical and Engineering Sciences*.

Kornhaas, M., Sternel, D. C., and Schäfer, M. (2008). Influence of Time Step Size and Convergence Criteria on Large Eddy Simulations with Implicit Time Discretization. In *Quality and Reliability of Large-Eddy Simulations*.

Korotenko, K. A. and Senchev, A. V. (2011). Turbulence investigation in a tidal coastal region. *Oceanology*, 51(3):394–406.

Krogstad, P. A. and Efros, V. (2012). About turbulence statistics in the outer part of a boundary layer developing over two-dimensional surface roughness. *Physics of Fluids*, 24(7).

Krogstad, P. . and Antonia, R. A. (1999). Surface roughness effects in turbulent boundary layers. *Experiments in Fluids*.

Launder, B. E. and Spalding, D. B. (1974). The numerical computation of turbulent flows. *Computer Methods in Applied Mechanics and Engineering*.

Laval, J. P., Elsner, W., Kuban, L., and Marquillie, M. (2011). LES modeling of converging diverging turbulent channel flow. In *ERCOFTAC Series*, volume 14, pages 355–363.

Lawson, M. J., Li, Y., and Sale, D. C. (2011). Development and Verification of a Computational Fluid Dynamics Model of a Horizontal-Axis Tidal Current Turbine. In *Volume 5: Ocean Space Utilization; Ocean Renewable Energy*, pages 711–720. ASME.

L.Brennan, M., H.Schoellhamer, D., R.Burau, J., and G.Monismith, S. (2002). Tidal asymmetry and variability of bed shear stress and sediment bed flux at a site in San Francisco Bay, USA. In *Proceedings in Marine Science*, volume 5, pages 93–107.

Lefebvre, A. and Winter, C. (2016). Predicting bed form roughness: the influence of lee side angle. *Geo-Marine Letters*.

Leonardi, S., Orlandi, P., Djenidi, L., and Antonia, R. A. (2004). Structure of turbulent channel flow with square bars on one wall. *International Journal of Heat and Fluid Flow*.

Lilly, D. (1967). Representation of small scale turbulence in numerical simulation experiments. *Proceedings of the IBM Scientific Computing Symposium on Environmental Sciences*.

Lilly, D. K. (1992). A proposed modification of the Germano subgrid-scale closure method. *Physics of Fluids A*.

Lu, S. S. and Willmarth, W. W. (1973). Measurements of the structure of the Reynolds stress in a turbulent boundary layer. *Journal of Fluid Mechanics*.

Lu, Y., Lueck, R. G., and Huang, D. (2002). Turbulence Characteristics in a Tidal Channel. *Journal of Physical Oceanography*, 30(5):855–867.

Ma, J., Wang, F., and Tang, X. (2008). Comparison of Several Subgrid-Scale Models for Large-Eddy Simulation of Turbulent Flows in Water Turbine. In *The 4th International Symposium on Fluid Machinery and Fluid Engineering*, pages 328–334, Beijing,China. Tsinghua University Press.

Maries, A., Abedul Haque, M., Yilmaz, S. L., Nik, M. B., and Marai, G. E. (2012). Interactive exploration of stress tensors used in computational turbulent combustion. In *Mathematics and Visualization*, number 202519, pages 137–156.

Marusic, I. and Adrian, R. J. (2010). The eddies and scales of wall turbulence. In *Ten Chapters in Turbulence*, pages 176–220.

Mazumder, B. S. and Sarkar, K. (2014). Turbulent flow characteristics and drag over 2-D forward-facing dune shaped structures with two different stoss-side slopes. *Environmental Fluid Mechanics*, 14(3):617–645.

McCaffrey, K., Fox-Kemper, B., Hamlington, P. E., and Thomson, J. (2015). Characterization of turbulence anisotropy, coherence, and intermittency at a prospective tidal energy site: Observational data analysis. *Renewable Energy*, 76:441–453.

McDonough, J. (2017). INTRODUCTORY LECTURES on TURBULENCE. *Journal of Molecular Liquids*, 246:363–371.

McMillan, J. M., Hay, A. E., Lueck, R. G., and Wolk, F. (2016). Rates of dissipation of turbulent kinetic energy in a high reynolds number tidal channel. *Journal of Atmospheric and Oceanic Technology*, 33(4):817–837.

McNaughton, J., Rolfo, S., Apsley, D., Afgan, I., Stansby, P., and Stallard, T. (2012). CFD Prediction of Turbulent Flow on a Laboratory Scale Tidal Stream Turbine using RANS modelling. In *Asian Wave and Tidal Energy Conference*, Jeju Island, Kore.

Milne, I. A., Sharma, R. N., and Flay, R. G. (2017). The structure of turbulence in a rapid tidal flow. *Proceedings of the Royal Society A: Mathematical, Physical and Engineering Sciences*, 473(2204).

Milne, I. A., Sharma, R. N., Flay, R. G. J., Bickerton, S., and A, P. T. R. S. (2013). Characteristics of the turbulence in the flow at a tidal stream power site Subject Areas :. *Phil. Trans. R. Soc. A.*, 371(1985):20120196.

Moin, P. and Kim, J. (1982). Numerical investigation of turbulent channel flow. *Journal of Fluid Mechanics*.

Moser, R. D., Kim, J., and Mansour, N. N. (1999). Direct numerical simulation of turbulent channel flow up to Reτ=590. *Physics of Fluids*.

Neill, S. P., Angeloudis, A., Robins, P. E., Walkington, I., Ward, S. L., Masters, I., Lewis, M. J., Piano, M., Avdis, A., Piggott, M. D., Aggidis, G., Evans, P., Adcock, T. A., Židonis, A., Ahmadian, R., and Falconer, R. (2018). Tidal range energy resource and optimization Past perspectives and future challenges. *Renewable Energy*, 127:763–778.

Neill, S. P., Hashemi, M. R., and Lewis, M. J. (2014). The role of tidal asymmetry in characterizing the tidal energy resource of Orkney. *Renewable Energy*, 68:337–350.

Neill, S. P., Vögler, A., Goward-Brown, A. J., Baston, S., Lewis, M. J., Gillibrand, P. A., Waldman, S., and Woolf, D. K. (2017). The wave and tidal resource of Scotland. *Renewable Energy*.

Nezu, I. and Nakagawa, H. (1993). *Turbulence in open channel flows*. CRC Press, Longon.

Nicoud, F. and Ducros, F. (1999). Subgrid-scale stress modelling based on the square of the velocity gradient tensor. *Flow, Turbulence and Combustion*, 62(3):183–200.

Omidyeganeh, M. and Piomelli, U. (2013a). Large-eddy simulation of three-dimensional dunes in a steady, unidirectional flow. Part 1. Turbulence statistics. *Journal of Fluid Mechanics*, 721:454–483.

Omidyeganeh, M. and Piomelli, U. (2013b). Large-eddy simulation of three-dimensional dunes in a steady, unidirectional flow. Part 2. Flow structures. *Journal of Fluid Mechanics*, 734:509–534.

Osalusi, E. (2010). *Analysis of wave and current data in a tidal energy test site*. PhD thesis, Heriot-Watt University.

Osalusi, E., Side, J., and Harris, R. (2009a). Reynolds stress and turbulence estimates in bottom boundary layer of Fall of Warness . *International Communications in Heat and Mass Transfer*, 36(5):412–421.

Osalusi, E., Side, J., and Harris, R. (2009b). Structure of turbulent flow in EMEC's tidal energy test site. *International Communications in Heat and Mass Transfer*, 36(5):422–431.

Ouro, P. and Stoesser, T. (2018). Impact of Environmental Turbulence on the Performance and Loadings of a Tidal Stream Turbine. *Flow, Turbulence and Combustion*.

Perry, A., Mesbah Uddin, A. K., and Marusic Ivan (1995). Similarity laws and attached eddy shapes in turbulent boundary layers. pages 203–206, Sydney.

Piomelli , U., Balaras, E., and Pascarelli, A. (2002). Turbulent structures in accelerating boundary layers. *Journal of Turbulence*, 1:N1.

Pope, S. B. (2004). Ten questions concerning the large-eddy simulation of turbulent flows. *New Journal of Physics*.

Raw, M. (1995). A Coupled Algebraic Multigrid Method for the 3D Navier-Stokes Equations. pages 204–215. Vieweg+Teubner Verlag, Wiesbaden.

Roache, P. J. (1998). Verification and Validation in Computational Science and Engineering. In *Computing in Science Engineering*, pages 8–9.

Robins, P. E., Neill, S. P., Lewis, M. J., and Ward, S. L. (2015). Characterising the spatial and temporal variability of the tidal-stream energy resource over the northwest European shelf seas. *Applied Energy*, 147:510–522.

Robinson, S. (2002). Coherent Motions In The Turbulent Boundary Layer. *Annual Review of Fluid Mechanics*, 23(1):601–639.

Roussinova, V. (2009). *Scholarship at UWindsor Turbulent structures in smooth and rough open channel flows : effect of depth.* PhD thesis, University of Windsor.

Roussinova, V., Biswas, N., and Balachandar, R. (2008). Revisiting turbulence in smooth uniform open channel flow. *Journal of Hydraulic Research*, 46:36–48.

Roussinova, V., Shinneeb, A.-M., and Balachandar, R. (2009). Investigation of Fluid Structures in a Smooth Open-Channel Flow Using Proper Orthogonal Decomposition. *Journal of Hydraulic Engineering*, 136(3):143–154.

Schmitt, F. G. (2007). doi:10.1016/j.crme.2007.08.004. *C. R. Mecanique*, 335:617–627.

Sellar, B., Wakelam, G., Sutherland, D. R., Ingram, D. M., and Venugopal, V. (2018). Characterisation of Tidal Flows at the European Marine Energy Centre in the Absence of Ocean Waves. *Energies*, 11(1):176.

Sellar, B. G. and Sutherland, D. R. J. (2016). Tidal Energy Site Characterisation at the Fall of Warness, EMEC, UK. Technical report.

Seller, B. and Sutherland, D. (2015). At the Fall of Warness Redapt MA1001 (MD3.8). Technical report, UK Energy Technologies Institute, EMEC, UK.

Shamsoddin, S. and Porté-Agel, F. (2017). Large-Eddy Simulation of Atmospheric Boundary-Layer Flow Through a Wind Farm Sited on Topography. *Boundary-Layer Meteorology*.

Shima, E., Kitamura, K., and Haga, T. (2013). Green-Gauss/Weighted-Least-Squares Hybrid Gradient Reconstruction for Arbitrary Polyhedra Unstructured Grids. *AIAA Journal*, 51(11).

Siemens (2018). STAR-CCM+ Users Guide.

Simonsen, A. J. and Krogstad, P. . (2005). Turbulent stress invariant analysis: Clarification of existing terminology. *Physics of Fluids*, 17(8):1–4.

Smagorinsky, J. (1963). General Circulation Experiments With the Primitive Equations. I: The basics experiment. *Monthly Weather Review*.

Smalley, R., Leonardi, S., Antonia, R., Djenidi, L., and Orlandi, P. (2002). Reynolds stress anisotropy of turbulent rough wall layers. *Experiments in Fluids*.

Smith, C. (1984). A synthesized model of the near-wall behavior in turbulent boundary layers. *Proceedings of the 8th Symposium of Turbulence,*.

Smith, W. A. M. N., Katz, J., and Osborn, T. R. (2005). On the Structure of Turbulence in the Bottom Boundary Layer of the Coastal Ocean. Technical Report 1.

Smits, A. J., McKeon, B. J., and Marusic, I. (2011). HighReynolds Number Wall Turbulence. *Annual Review of Fluid Mechanics*, 43(1):353–375.

Spalart, P. R. (1988). Direct simulation of a turbulent boundary layer up to Rθ= 1410. *Journal of Fluid Mechanics*.

Stacey, M. T. and Ralston, D. K. (2005). The Scaling and Structure of the Estuarine Bottom Boundary Layer. *Journal of Physical Oceanography*, 35(1):55–71.

Steele, E. C., Nimmo-Smith, W. A. M., and Vlasenko, A. (2016). Direct measurement of hairpin-like vortices in the bottom boundary layer of the coastal ocean. *Geophysical Research Letters*, 43(3):1175–1183.

Stoesser, T. (2013). Calculation and Eduction of Coherent Flow Structures in Open-Channel Flow Using Large-Eddy Simulations. *Coherent Flow Structures at Earth's Surface*, pages 175–197.

Stoesser, T., Braun, C., García-Villalba, M., and Rodi, W. (2007). Turbulence Structures in Flow over Two-Dimensional Dunes. *Journal of Hydraulic Engineering*.

Theodorsen, T. (1952). Mechanism of turbulence. In *Proc. {M}idwest. {C}onf. {F}luid {M}ech. 2nd, {C}olumbus, {O}hio*.

Thomson, J., Polagye, B., Durgesh, V., and Richmond, M. C. (2012). Measurements of turbulence at two tidal energy sites in puget sound, WA. *IEEE Journal of Oceanic Engineering*, 37(3):363–374.

Thomson, J., Polagye, B., Richmond, M., and Durgesh, V. (2010). Quantifying turbulence for tidal power applications. *MTS/IEEE Seattle, OCEANS 2010*, (4):1–8.

Thyng, K. M., Riley, J. J., and Thomson, J. (2013). Inference of turbulence parameters from a ROMS simulation using the k-ϵ closure scheme. *Ocean Modelling*, 72:104–118.

Togneri, M., Lewis, M., Neill, S., and Masters, I. (2017). Comparison of ADCP observations and 3D model simulations of turbulence at a tidal energy site. *Renewable Energy*, 114:273–282.

Townsend, A. A. (1961). Equilibrium layers and wall turbulence. *Journal of Fluid Mechanics*.

Turnock, S. R., Phillips, A. B., Banks, J., and Nicholls-Lee, R. (2011). Modelling tidal current turbine wakes using a coupled RANS-BEMT approach as a tool for analysing power capture of arrays of turbines. *Ocean Engineering*, 38(11-12):1300–1307.

Uchida, T. (2017). High-Resolution LES of Terrain-Induced Turbulence around Wind Turbine Generators by Using Turbulent Inflow Boundary Conditions. *Open Journal of Fluid Dynamics*, 07(04):511–524.

Union, E. (2014). 2030 Climate and Energy policy framework. Technical report, European Council, Brussels, Belgium.

Venugopal, V. and Nemalidinne, R. (2014). Marine energy resource assessment for Orkney and Pentland waters with a coupled wave and tidal flow model. Technical report.

Versteeg, H. and Malalasekera, W. (2007). *An Introduction to Computational Fluid Dynamics*.

Waldman, S., Bastón, S., Nemalidinne, R., Chatzirodou, A., Venugopal, V., and Side, J. (2017). Implementation of tidal turbines in MIKE 3 and Delft3D models of Pentland Firth & Orkney Waters. *Ocean and Coastal Management*.

Wilcox, D. C. (2006). *Turbulence Modeling for CFD*. DCW Industries, San Diego, third edition.

Willmarth, W. W. and Lu, S. S. (1972). Structure of the reynolds stress near the wall. *Journal of Fluid Mechanics*.

Wu, Y. and Christensen, K. T. (2007). Reynolds-Stress Enhancement Associated with a Short Fetch of Roughness in Wall Turbulence. *AIAA Journal*.

Xie, Z., Lin, B., Falconer, R. A., and Maddux, T. B. (2013). Large-eddy simulation of turbulent open-channel flow over three-dimensional dunes. *Journal of Hydraulic Research*.

Xie, Z. T., Coceal, O., and Castro, I. P. (2008). Large-Eddy simulation of flows over random urban-like obstacles. *Boundary-Layer Meteorology*.

Yang, X., Howard, K. B., Guala, M., and Sotiropoulos, F. (2015). Effects of a three-dimensional hill on the wake characteristics of a model wind turbine. *Physics of Fluids*, 27(2):25103.

Yue, W., Lin, C.-L., and Patel, V. C. (2005). Coherent Structures In Open-Channel Flows Over a Fixed Dune. *Journal of Fluids Engineering*, 127(5):858.

Yue, W., Meneveau, C., Parlange, M. B., Zhu, W., Van Hout, R., and Katz, J. (2007). A comparative quadrant analysis of turbulence in a plant canopy. *Water Resources Research*, 43(5):2–15.

Zangiabadi, E., Edmunds, M., Fairley, I. A., Togneri, M., Williams, A. J., Masters, I., and Croft, N. (2015). Computational fluid dynamics and visualisation of coastal flows in tidal channels supporting ocean energy Development. *Energies*.

APPENDIX A VALIDATION RESULTS FOR STANDARD PLANE CHANNEL FLOW CASE.

A Fully Developed Turbulent Channel Flow Experiments and Validation

In order to have appropriate validation of the simulations presented in chapters 4-7 for a tidal channel with bathymetry, simulations of a standard flat channel flow were tested as a validation test of feasibility for the mesh, model and boundary conditions used. This appendix presents the validation data for mean streamwise velocity u profiles (figure 1), cross-component of streamwise and wall normal Reynolds stress $-\overline{u'w'}$ normalized by the friction velocity squared u_τ^2 (figure 2) and diagonal streamwise component $\overline{u'u'}$ again normalized by friction velocity squared u_τ^2 (figure 3) . Turbulence data used to validate the fully developed turbulent channel flow was taken from Wei and Willmarth (1989) and Schultz and Flack (2013) who in turn cite Hoyas and Jiménez (2006) a reference in their data.

Case was chosen also based on the recommendation of LES simulations. by the AGARD Advisory report "A selection of test cases used for the validation of

Large-Eddy Simulations of Turbulent Flows" Advisory et al. (1998) using the data sheets for pipes and channels PCH12 Fully Developed Turbulent Channel Flow Experiments, Data was chosen due to the same boundary conditions as the smooth wall simulation presented in chapter 7 and discussed in chapters 4,5 and 6.

The boundary conditions of the validation experiments cited are as follows: rigid top and side walls 173δ from the channel inlet, sufficiently long for the channel to be developed. The only variable parameter in the flow is the Reynolds number, data from Wei & Willmarth includes bulk Reynolds numbers $Re_b = 113145, 20197$ and 35353. Reynolds number for channel flow is based on a channel height and bulk mean velocity. Turbulent data is however normalized by the scaling factor of friction velocity u_τ to apply for all sufficiently high Reynolds numbers. Results are further compared to similar Reynolds number by experimental results from Schultz and Flack (2013) in the range of bulk $Re = 10,000$ *to* 300000 which the authors convert into a frictional Reynolds number of $Re_\tau = 1000 - 6000$. This second experimental result comparison was done due to the authors comparison to a DNS numerical simulation and having the streamwise diagonal Reynolds stress component available for validation.

Data from channel flow flat case (FC) shown in chapter 7. Data was time and ensemble averaged at several locations of the domain due to the symmetrical nature of the domain for a total of 90000 data points per vertical profile. Domain was composed of a mesh equal to 1200 x 305 x 50 for a domain size of 34.2H x 7.5H x H, where H is the domain height. Simulation was run at a t*=0.0106 time step for a total run time t*=95.77 giving 9000 time steps as explained in simulation design chapter 4 of the main body of the thesis. Mesh parameters were equal to the ones described in chapter 4, however due to the different wall friction this decreased the non-dimensionalized wall location $z^+ = 10$.

Reynolds number based on the channel height and bulk velocity was equal to 50 million or $Re_\tau = 2.34x10^6$. All lines compared to validation data will be marked at one of these two Reynolds numbers in accordance with the nomenclature originally used by the respective authors.

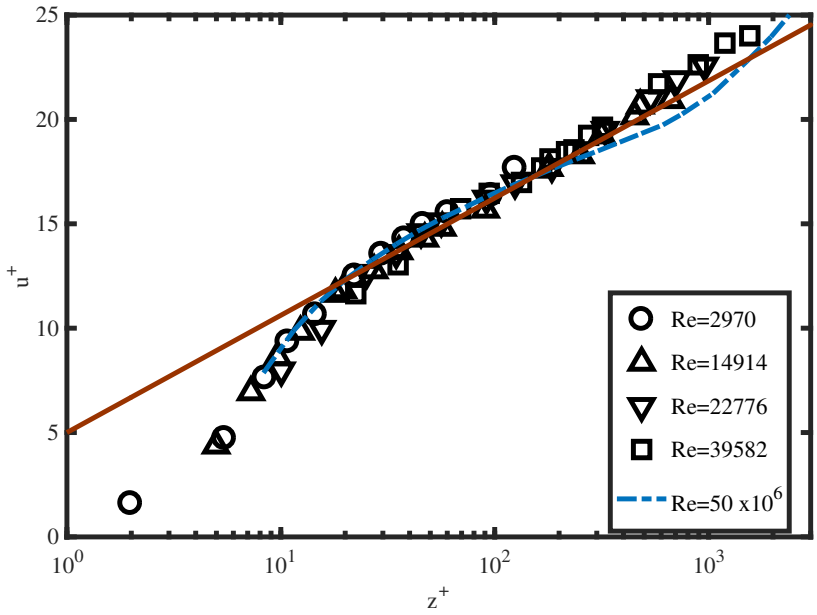

Figure 1: Mean streamwise velocity Profile non-dimensionalized by friction variables. Solid red line is the log-law of the wall for a turbulent boundary layer. Solid blue line is the $u^+ = z^+$ profile.

Figure 1 shows the ensemble averaged streamwise velocity profile compared to both experimental results for all of the Reynolds numbers mentioned by Wei and Willmarth (1989) as well as the log-law in a solid red line and the $u^+ = z^+$ equation for lower values near the wall. Maximum disagreement between log law and the simulation was 4.7% in the outer layer. This is in the same order as the experimental values for any Reynolds number shown. Only the first value followed the lower value of the wall behaviour, however this gave no issues for the rest of the velocity profile.

Figure 2 shows strong agreement with all of the Reynolds numbers shear stress components. Although the values are of Reynolds numbers magnitudes lower than the simulation presented, Wei & Willmarth argue that above a certain Reynolds number (approx 10,000 for this case) Reynolds stress values will not be Reynolds number dependent as is seen with the difference between Re=2970 and the other experimental results. Simulation results only had a drop from experimental values in the last quarter of the channel height, however near wall values were all within experimental range, showing the models's capabilities for generating turbulence.

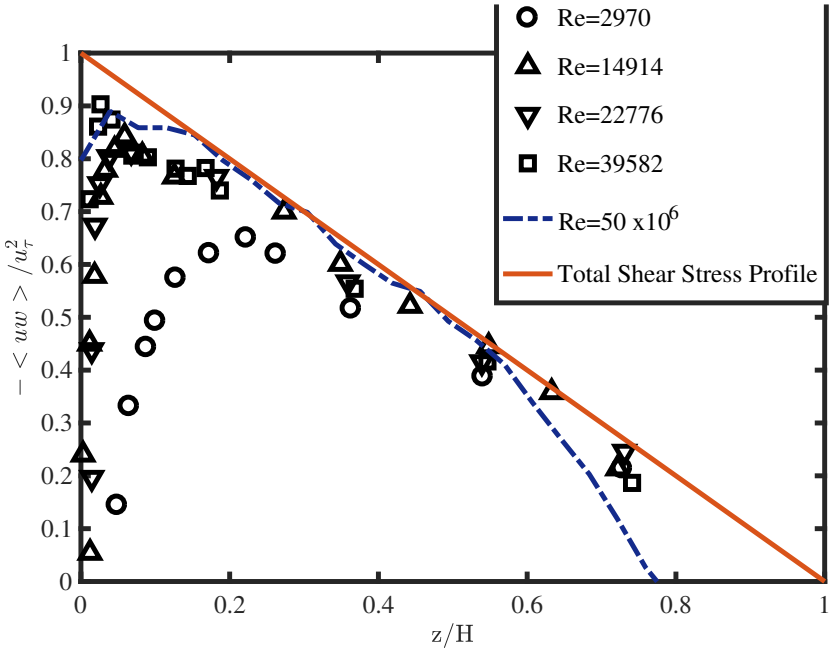

Figure 2: Reynolds stress component $-\overline{u'w'}/u_\tau^2$ normalized by friction velocity u_τ^2 validation of simulation data.

Fig 3 shows a comparison of the diagonal value of the Reynolds Stress normalized by the friction velocity compared to the non-dimensionalized channel height. Once more, all sufficiently high Reynolds numbers should hold similar behaviour as long as normalized by the friction velocity. All values were within experimental and DNS ranges for Re_τ in the range of 1000 to 6000. Only peak values were overestimated near the wall for a single data point of 6.6% and near the end of the half channel height.

By comparing mean velocity data, cross component wall shear stress and diagonal component Reynolds stress it is considered that the mesh, boundary conditions and model are of sufficient fidelity as to be considered validated to classical case results for the main variables that were sought in the main body of work.

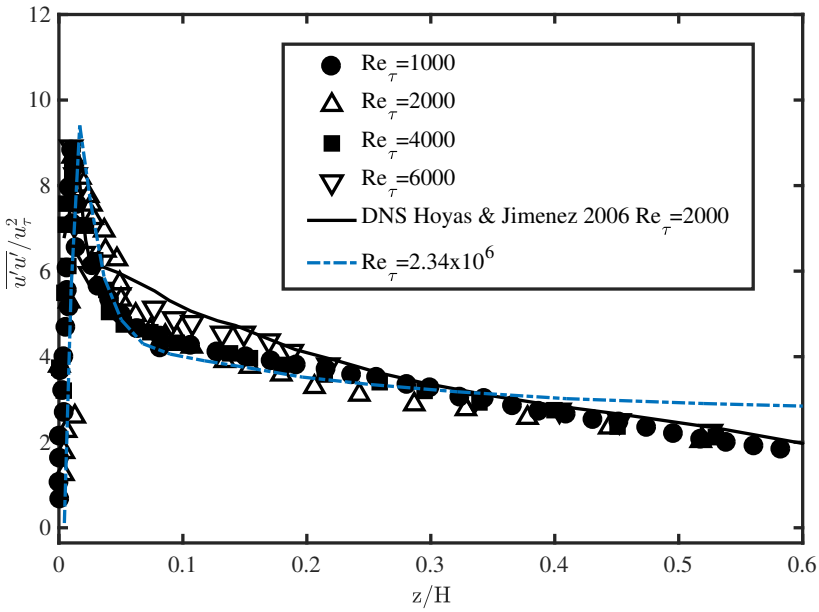

Figure 3: Streamwise $\overline{u'u'}/u_\tau^2$ normalized by friction velocity u_τ^2 validation of simulation data.

BIBLIOGRAPHY

Advisory, A., No, R., and Wray, A. A. (1998). A Selection of Test Cases for the Validation of Large-Eddy Simulations of Turbulent Flows. *AGARD Advisory Report*.

Hoyas, S. and Jiménez, J. (2006). Scaling of the velocity fluctuations in turbulent channels up to Reτ=2003. *Physics of Fluids*.

Schultz, M. P. and Flack, K. A. (2013). Reynolds-number scaling of turbulent channel flow. *Physics of Fluids*.

Wei, T. and Willmarth, W. W. (1989). Reynolds-number effects on the structure of a turbulent channel flow. *Journal of Fluid Mechanics*.